



AFRL-RB-WP-TR-2010-3111

**STRUCTURAL TECHNOLOGY EVALUATION ANALYSIS
PROGRAM (STEAP)**

Delivery Order 0025: Laser Peening for Reliable Fatigue Life

Hemanth Amarchinta and Ramana V. Grandhi

Wright State University

DECEMBER 2010

Final Report

Approved for public release; distribution unlimited.

See additional restrictions described on inside pages

STINFO COPY

**AIR FORCE RESEARCH LABORATORY
AIR VEHICLES DIRECTORATE
WRIGHT-PATTERSON AIR FORCE BASE, OH 45433-7542
AIR FORCE MATERIEL COMMAND
UNITED STATES AIR FORCE**

NOTICE AND SIGNATURE PAGE

Using Government drawings, specifications, or other data included in this document for any purpose other than Government procurement does not in any way obligate the U.S. Government. The fact that the Government formulated or supplied the drawings, specifications, or other data does not license the holder or any other person or corporation; or convey any rights or permission to manufacture, use, or sell any patented invention that may relate to them.

This report was cleared for public release by the USAF 88th Air Base Wing (88 ABW) Public Affairs Office (PAO) and is available to the general public, including foreign nationals. Copies may be obtained from the Defense Technical Information Center (DTIC) (<http://www.dtic.mil>).

AFRL-RB-WP-TR-2010-3111 HAS BEEN REVIEWED AND IS APPROVED FOR PUBLICATION IN ACCORDANCE WITH THE ASSIGNED DISTRIBUTION STATEMENT.

*//Signature//

KRISTINA LANGER
Program Manager
Analytical Mechanics Branch
Structures Division

//Signature//

MICHAEL J. SHEPARD, Chief
Analytical Mechanics Branch
Structures Division

//Signature//

DAVID M. PRATT, Technical Advisor
Structures Division
Air Vehicles Directorate

This report is published in the interest of scientific and technical information exchange, and its publication does not constitute the Government's approval or disapproval of its ideas or findings.

*Disseminated copies will show “//Signature//” stamped or typed above the signature blocks.

| REPORT DOCUMENTATION PAGE | | | | | <i>Form Approved</i> OMB No. 0704-0188 | | | |
|---|--|-------------------------------------|---|--|--|---|--|--|
| The public reporting burden for this collection of information is estimated to average 1 hour per response, including the time for reviewing instructions, searching existing data sources, gathering and maintaining the data needed, and completing and reviewing the collection of information. Send comments regarding this burden estimate or any other aspect of this collection of information, including suggestions for reducing this burden, to Department of Defense, Washington Headquarters Services, Directorate for Information Operations and Reports (0704-0188), 1215 Jefferson Davis Highway, Suite 1204, Arlington, VA 22202-4302. Respondents should be aware that notwithstanding any other provision of law, no person shall be subject to any penalty for failing to comply with a collection of information if it does not display a currently valid OMB control number. PLEASE DO NOT RETURN YOUR FORM TO THE ABOVE ADDRESS. | | | | | | | | |
| 1. REPORT DATE (DD-MM-YY) December 2010 | | 2. REPORT TYPE Final | | 3. DATES COVERED (From - To) 01 January 2008 – 31 December 2010 | | | | |
| 4. TITLE AND SUBTITLE STRUCTURAL TECHNOLOGY EVALUATION ANALYSIS PROGRAM (STEAP) Delivery Order 0025: Laser Peening for Reliable Fatigue Life | | | | 5a. CONTRACT NUMBER FA8650-04-D-3446-0025 | | | | |
| | | | | 5b. GRANT NUMBER | | | | |
| | | | | 5c. PROGRAM ELEMENT NUMBER 62201F | | | | |
| 6. AUTHOR(S) Hemanth Amarchinta and Ramana V. Grandhi | | | | 5d. PROJECT NUMBER 2401 | | | | |
| | | | | 5e. TASK NUMBER | | | | |
| | | | | 5f. WORK UNIT NUMBER A0F10A | | | | |
| 7. PERFORMING ORGANIZATION NAME(S) AND ADDRESS(ES) <table style="width: 100%; border: none;"> <tr> <td style="width: 50%; vertical-align: top;"> By: Wright State University Ohio Center of Excellence in Product Reliability and Optimization 3640 Colonel Glenn Highway Dayton, OH 45435 </td> <td style="width: 50%; vertical-align: top;"> For: General Dynamics Information Technology 5100 Springfield Pike, Suite 509 Dayton, OH 45431 </td> </tr> </table> | | | | By: Wright State University Ohio Center of Excellence in Product Reliability and Optimization 3640 Colonel Glenn Highway Dayton, OH 45435 | For: General Dynamics Information Technology 5100 Springfield Pike, Suite 509 Dayton, OH 45431 | 8. PERFORMING ORGANIZATION REPORT NUMBER | | |
| By: Wright State University Ohio Center of Excellence in Product Reliability and Optimization 3640 Colonel Glenn Highway Dayton, OH 45435 | For: General Dynamics Information Technology 5100 Springfield Pike, Suite 509 Dayton, OH 45431 | | | | | | | |
| 9. SPONSORING/MONITORING AGENCY NAME(S) AND ADDRESS(ES) Air Force Research Laboratory Air Vehicles Directorate Wright-Patterson Air Force Base, OH 45433-7542 Air Force Materiel Command United States Air Force | | | | | | | | |
| 10. SPONSORING/MONITORING AGENCY ACRONYM(S) AFRL/RBSM | | | | 11. SPONSORING/MONITORING AGENCY REPORT NUMBER(S) AFRL-RB-WP-TR-2010-3111 | | | | |
| | | | | | | | | |
| 12. DISTRIBUTION/AVAILABILITY STATEMENT Approved for public release; distribution unlimited. | | | | | | | | |
| 13. SUPPLEMENTARY NOTES PAO Case Number: 88ABW-2011-0071; Clearance Date: 10 January 2011. Report contains color. | | | | | | | | |
| 14. ABSTRACT Laser peening (LP) is an advanced mechanical surface enhancement technique used to increase the fatigue life of metallic components. To reduce costs and make the technique available on a large-scale basis for industrial applications, simulation of the LP process is required. One of the objectives of this research is to make advancements in the simulation of LP-induced residual stresses by validating various material models for use in simulation and design. An inverse optimization-based methodology is developed, which involves optimizing the model constants for one load case and using the same constants for other load cases. The second aspect of this research is to develop a framework for uncertainty quantification of the residual stress field induced by the LP process by propagation of regression uncertainty. Development methodology includes identification of regression uncertainty as a source of input uncertainty and using the bootstrap method to verify the multivariate normality assumption of the model constant estimates. The propagation of the input uncertainty is performed using Taylor series expansion and sensitivity analysis. A confidence band for the entire residual stress field is obtained and validated using the Monte Carlo analysis. | | | | | | | | |
| 15. SUBJECT TERMS laser peening, laser shock processing, residual stress, aircraft fatigue, optimization, uncertainty analysis | | | | | | | | |
| 16. SECURITY CLASSIFICATION OF: | | | 17. LIMITATION OF ABSTRACT: SAR | 18. NUMBER OF PAGES 150 | 19a. NAME OF RESPONSIBLE PERSON (Monitor) Kristina Langer 19b. TELEPHONE NUMBER (Include Area Code) N/A | | | |
| a. REPORT Unclassified | b. ABSTRACT Unclassified | c. THIS PAGE Unclassified | | | | | | |

ABSTRACT

Advanced mechanical surface enhancement techniques (SET) have been used successfully to increase the fatigue life of metallic components. These techniques impart deep compressive residual stresses into the component to counter potentially damage-inducing tensile stresses generated under service loading. Laser peening (LP) is an advanced mechanical SET used predominantly in the aircraft industry. To reduce costs and make the technique available on a large-scale basis for industrial applications, simulation of the LP process is required. Accurate simulation of the LP process is a challenging task, because the process has many parameters such as laser spot size, pressure profile, and material model that must be precisely determined. In the LP process material is subjected to strain rates up to $10^6 s^{-1}$, which is very high compared to conventional strain rates. The importance of an accurate material model increases because the material behaves significantly different at such high strain rates. One of the objectives of this research is to make advancements in the simulation of residual stresses induced by LP. Validation of various material models under investigation that could be used in simulation and design is performed. Inverse optimization-based methodology is developed for simulation of residual stresses for materials such as Inconel®718. The procedure involves optimizing the model constants for one load case and using the same constants for other load cases. The second aspect of this research is to develop a framework for uncertainty quantification of the residual stress field induced by the LP process by propagation of regression uncertainty. Development methodology includes identification of regression uncertainty as a source of input uncertainty and using the bootstrap method to verify the multivariate normality assumption of the model constant estimates. The propagation of the input uncertainty is performed using Taylor series expansion and sensitivity analysis. A confidence band for the entire residual stress field is obtained and validated using the Monte Carlo analysis.

TABLE OF CONTENTS

| <u>Section</u> | <u>Page</u> |
|---|--------------------|
| List of Figures | iv |
| List of Tables | vii |
| 1. Summary | 1 |
| 2. Introduction | 2 |
| 2.1 Motivation..... | 2 |
| 2.2 SET..... | 3 |
| 2.2.1 Shot Peening..... | 4 |
| 2.2.2 LPB..... | 5 |
| 2.2.3 Waterjet Peening | 6 |
| 2.2.4 LP | 7 |
| 2.3 Section Summary | 8 |
| 3. Background..... | 9 |
| 3.1 Historical Perspective | 9 |
| 3.2 Experimental Attribute of LP | 9 |
| 3.2.1 Laser Systems..... | 9 |
| 3.2.2 Opaque Overlay..... | 10 |
| 3.2.3 Transparent Overlay | 10 |
| 3.3 Review of Simulation of the LP Process | 10 |
| 3.4 Review of Relevant Uncertainty Quantification Research | 12 |
| 3.4.1 Sources of Uncertainty in LP Simulation..... | 13 |
| 3.5 Definition of Research Need..... | 15 |
| 3.6 Project Scope and Organization..... | 15 |
| 4. Material Model Validation of Laser Peened Residual Stresses..... | 18 |
| 4.1 LP Description with Reference to Simulation | 18 |
| 4.1.1 Thick and Thin Geometries..... | 18 |
| 4.2 Material Model Details | 19 |
| 4.2.1 The EPP Model | 20 |
| 4.2.2 The JC Model | 20 |
| 4.2.3 The ZA Model..... | 21 |
| 4.2.4 Parameter Estimation | 21 |
| 4.3 Simulation Procedure..... | 25 |
| 4.3.1 Pressure Loads..... | 26 |
| 4.3.2 Material Models | 27 |
| 4.3.3 Analysis Procedure..... | 28 |

| | | |
|---------|---|-----|
| 4.3.3.1 | Dynamic Loading Analysis..... | 29 |
| 4.3.3.2 | Static Equilibrium Analysis..... | 30 |
| 4.3.3.3 | Comparison between Explicit and Implicit Algorithms..... | 30 |
| 4.4 | Results and Discussion..... | 31 |
| 4.4.1 | The EPP Model..... | 34 |
| 4.4.2 | The JC Model..... | 40 |
| 4.4.3 | The ZA Model..... | 43 |
| 4.4.4 | Additional Performance Metrics..... | 44 |
| 4.5 | Section Summary..... | 46 |
| 5. | Inverse Optimization of Material Models for Simulation of Laser Peened Residual Stresses..... | 47 |
| 5.1 | Limitation of Existing Simulation Methodology..... | 47 |
| 5.2 | Optimization-based Approach..... | 48 |
| 5.3 | Material Model Details..... | 49 |
| 5.3.1 | KHL Model..... | 49 |
| 5.4 | Simulation Procedure..... | 50 |
| 5.5 | Results and Discussion..... | 50 |
| 5.5.1 | Validation of Optimization-Based Approach for Inconel®718..... | 50 |
| 5.5.1.1 | LP Experimental Procedure..... | 50 |
| 5.5.1.2 | Residual Stress Comparison Between Simulations and Experiments..... | 51 |
| 5.5.2 | Validation of Optimization-Based Approach and Comparison with Traditional Approach for Ti-6Al-4V..... | 57 |
| 5.6 | Section Summary and Conclusions..... | 70 |
| 6. | Probabilistic Framework for Laser peened Residual Stress Field by Propagation of Regression Uncertainty..... | 71 |
| 6.1 | Deterministic LP Simulation Procedure..... | 71 |
| 6.2 | Cause and Effect of Uncertainty in LP Simulation..... | 72 |
| 6.3 | Probabilistic Framework for LP Simulation..... | 72 |
| 6.3.1 | Regression (Input) Uncertainty..... | 73 |
| 6.3.2 | What is Bootstrapping?..... | 75 |
| 6.3.2.1 | Bootstrapping for Regression..... | 76 |
| 6.3.3 | Uncertainty Propagation..... | 89 |
| 6.3.4 | Residual Stress Field Confidence Band..... | 93 |
| 6.4 | Regression (Input) Uncertainty Quantification Results..... | 94 |
| 6.5 | Demonstration Examples and LP Application..... | 97 |
| 6.5.1 | Demonstration Example 1..... | 97 |
| 6.5.2 | Demonstration Example 2..... | 104 |
| 6.5.3 | LP Application..... | 112 |
| 6.6 | Section Summary..... | 118 |

| | | |
|-------|---|-----|
| 7. | Summary and Future Directions | 119 |
| 7.1 | Future Directions | 120 |
| 7.1.1 | Modeling of Thin Specimens | 120 |
| 7.1.2 | Two Sided LP Simulation | 120 |
| 7.1.3 | Geometric Effects of the LP Process | 120 |
| 7.1.4 | Bootstrapping Method for Parametric Uncertainty | 120 |
| 7.1.5 | Integration Framework for LP Design | 121 |
| 8. | References | 123 |
| | LIST OF ACRONYMS, ABBREVIATIONS, AND SYMBOLS | 130 |

List of Figures

| Figure | Page |
|---|------|
| 1. Two F-22 Raptors in Column Flight Formation [2] | 2 |
| 2. Location of Crack on an Aircraft Lug [4] | 3 |
| 3. Attributes Considered During Conceptual Stage of a Component | 3 |
| 4. Basic Mechanism to Generate Residual Stresses..... | 4 |
| 5. Schematic of the Shot Peening Process | 5 |
| 6. Schematic of the LPB Process | 6 |
| 7. Schematic of the Waterjet Peening Process..... | 7 |
| 8. Schematic of the LP..... | 8 |
| 9. Sources of Uncertainty During LP Simulation | 14 |
| 10. Project Scope | 16 |
| 11. Simulation Overview | 17 |
| 12. Overview of Simulation Models | 19 |
| 13. The JC Model Fit to Experimental Data [75] of Multiple Strain Rates..... | 22 |
| 14. The ZA Model Fit to Experimental Data [75] of Multiple Strain Rates..... | 23 |
| 15. Strain Rate Dependence Curve for the JC Model..... | 24 |
| 16. Strain Rate Dependence Curve for the ZA Model..... | 25 |
| 17. Representative Axi-symmetric FE Mesh | 26 |
| 18. Temporal Pressure Profile of Shock Wave | 27 |
| 19. Spatial Pressure Profile of Shock Wave | 27 |
| 20. Schematic Representation of Analysis Procedure | 29 |
| 21. History of Kinetic Energy | 30 |
| 22. Residual Stress Comparison Between Simulation and Experiment for the EPP model | 32 |
| 23. Residual Stress Comparison Between Simulation and Experiment for the JC model..... | 33 |
| 24. Residual Stress Comparison Between Simulation and Experiment for the ZA model..... | 34 |
| 25. Equivalent Plastic Strain Variation with Depth for the EPP Model | 35 |
| 26. Propagation of Stress Waves for the EPP model at 5.5 GPa Peak Pressure..... | 36 |
| 27. Propagation of Stress Waves for the EPP model at 8.3 GPa Peak Pressure..... | 37 |
| 28. Propagation of Stress Waves for the JC Model at 5.5 GPa Peak Pressure | 38 |
| 29. Propagation of Stress Waves for the JC Model at 8.3 GPa Peak Pressure | 39 |
| 30. Residual Stress Comparison Between Simulation and Experiment for the EPP Model..... | 40 |
| 31. Equivalent Plastic Strain Variation with Depth for the JC Model..... | 41 |
| 32. Residual Stress Comparison Between Simulation and Experiment for the JC Model | 42 |
| 33. Equivalent Plastic Strain Variation with Depth for the ZA Model..... | 43 |
| 34. Residual Stress Comparison Between Simulation and Experiment for the ZA Model | 44 |
| 35. Traditional Approach for Simulation of Laser Peened Residual Stresses | 47 |
| 36. Optimization-Based Approach for Simulation of Laser Peened Residual Stresses..... | 48 |
| 37. Residual Stress Comparison for Inconel®718 with 5.3 GPa Peak Pressure | 53 |
| 38. Residual Stress Comparison for Inconel®718 with 6.6 GPa Peak Pressure | 54 |
| 39. Residual Stress Comparison for Inconel®718 with 7.1 GPa Peak Pressure | 55 |
| 40. Residual Stress Comparison for Inconel®718 with 7.6 GPa Peak Pressure | 56 |
| 41. Residual Stress Comparison for Ti-6Al-4V for the JC Model with 5.5 Peak Pressures | 60 |
| 42. Residual Stress Comparison for Ti-6Al-4V for the JC Model with 6.1 Peak Pressures | 61 |

| | |
|--|-----|
| 43. Residual Stress Comparison for Ti-6Al-4V for the JC Model with 8.3 Peak Pressures | 62 |
| 44. Residual Stress Comparison for Ti-6Al-4V for the ZA Model with 5.5 Peak Pressures | 63 |
| 45. Residual Stress Comparison for Ti-6Al-4V for the ZA Model with 6.1 Peak Pressures | 64 |
| 46. Residual Stress Comparison for Ti-6Al-4V for the ZA Model with 8.3 Peak Pressures | 65 |
| 47. Residual Stress Comparison for Ti-6Al-4V for the KHL Model with 5.5 Peak Pressures | 66 |
| 48. Residual Stress Comparison for Ti-6Al-4V for the KHL Model with 6.1 Peak Pressures | 67 |
| 49. Residual Stress Comparison for Ti-6Al-4V for the KHL Model with 8.3 Peak Pressures | 68 |
| 50. Deterministic Simulation Procedure of the LP Process | 71 |
| 51. Probabilistic Framework for LP Simulation | 73 |
| 52. Schematic Representation of Bootstrap Method | 76 |
| 53. Histogram of Mean of the Sample Data | 77 |
| 54. Parametric Bootstrap Histogram of $\hat{\beta}_0^*$ for the Demonstration Example | 81 |
| 55. Parametric Bootstrap Histogram of $\hat{\beta}_1^*$ for the Demonstration Example | 81 |
| 56. Parametric Bootstrap Histogram of $\hat{\beta}_2^*$ for the Demonstration Example | 82 |
| 57. Random-x Bootstrap Histogram of $\hat{\beta}_0^*$ for the Demonstration Example | 85 |
| 58. Random-x Bootstrap Histogram of $\hat{\beta}_1^*$ for the Demonstration Example | 85 |
| 59. Random-x Bootstrap Histogram of $\hat{\beta}_2^*$ for the Demonstration Example | 86 |
| 60. Fixed-x Bootstrap Procedure Flowchart | 86 |
| 61. Fixed-x Bootstrap Histogram of $\hat{\beta}_0^*$ for the Demonstration Example | 88 |
| 62. Fixed-x Bootstrap Histogram of $\hat{\beta}_1^*$ for the Demonstration Example | 88 |
| 63. Fixed-x Bootstrap Histogram of $\hat{\beta}_2^*$ for the Demonstration Example | 89 |
| 64. Confidence Band Validation Procedure | 93 |
| 65. JC Model Fit to the Experimental Data | 94 |
| 66. JC Model Fit vs Actual Experimental Data | 95 |
| 67. JC Model Fit vs Residuals | 96 |
| 68. Bootstrap Histogram of \hat{A} | 97 |
| 69. Bootstrap Histogram of \hat{B} | 98 |
| 70. Bootstrap Histogram of \hat{n} | 98 |
| 71. Bootstrap Histogram of \hat{C} | 99 |
| 72. Deterministic Residual Stress Field for Demonstration Problem 1 | 100 |
| 73. Gradient of Residual Stress Field with respect to Model Constant Estimate \hat{A} for Demonstration Problem 1 | 100 |
| 74. Gradient of Residual Stress Field with respect to Model Constant Estimate \hat{B} for Demonstration Problem 1 | 101 |
| 75. Gradient of Residual Stress Field with respect to Model Constant Estimate \hat{n} for Demonstration Problem 1 | 101 |
| 76. Gradient of Residual Stress Field with respect to Model Constant Estimate \hat{C} for Demonstration Problem 1 | 102 |
| 77. 95% Confidence Band on the Residual Stress Field for Demonstration Problem 1 | 103 |
| 78. Standard Deviation of Residual Stress Field for Demonstration Problem 1 | 103 |
| 79. Confidence Level Comparison to Target Confidence Level for Demonstration Problem1 | 104 |
| 80. Response Surface Fit Comparison with FEA | 106 |
| 81. Deterministic Residual Stress Field for Demonstration Example 2 | 107 |
| 82. Gradient of Residual Stress Field with respect to Model Constant Estimate \hat{A} for Demonstration Problem 2 | 108 |

| | |
|---|-----|
| 83. Gradient of Residual Stress Field with respect to Model Constant Estimate \hat{B} for Demonstration Problem 2 | 108 |
| 84. Gradient of Residual Stress Field with respect to Model Constant Estimate \hat{n} for Demonstration Problem 2 | 109 |
| 85. Gradient of Residual Stress Field with respect to Model Constant Estimate \hat{C} for Demonstration Problem 2 | 110 |
| 86. 95% Confidence Band on the Residual Stress Field for Demonstration Problem 2..... | 111 |
| 87. Standard Deviation Variation along the Depth for Demonstration Problem 2 | 111 |
| 88. Confidence Level Comparison to Target Confidence Level for Demonstration Problem 2 | 112 |
| 89. Deterministic Residual Stress Field for the LP Process Simulation | 113 |
| 90. Gradient of Residual Stress Field with respect to Model Constant Estimate \hat{A} for the LP Simulation | 114 |
| 91. Gradient of Residual Stress Field with respect to Model Constant Estimate \hat{B} for the LP Simulation | 114 |
| 92. Gradient of Residual Stress Field with respect to Model Constant Estimate \hat{n} for the LP Simulation | 115 |
| 93. Gradient of Residual Stress Field with respect to Model Constant Estimate \hat{C} for the LP Simulation | 116 |
| 94. 95% Confidence Band on the Residual Stress Field for the LP Simulation | 117 |
| 95. Standard Deviation of Residual Stress Field for the LP Simulation | 117 |
| 96. Bootstrapping for Parametric Uncertainty | 121 |
| 97. Integration Framework for LP Design | 122 |

List of Tables

| Table | Page |
|---|------|
| 1. Material Properties of Ti-6Al-4V | 21 |
| 2. Model Constants for the JC Model | 23 |
| 3. Model Constants for the ZA Model | 24 |
| 4. Performance Metrics Comparison Between the Models for Peak Pressure of 5.5 GPa | 45 |
| 5. Performance Metrics Comparison Between the Models for Peak Pressure of 6.1 GPa | 45 |
| 6. Performance Metrics Comparison Between the Models for Peak Pressure of 8.3 GPa | 45 |
| 7. Material Properties for Inconel®718 | 50 |
| 8. LP Conditions Used for Inconel®718 | 51 |
| 9. In-Depth Residual Stresses for Inconel®718 [Courtesy: LSP Technologies, Inc.]..... | 52 |
| 10. Model Constants Using Optimization-Based Approach for the JC Model for Inconel®718 .. | 53 |
| 11. Least Square Error Comparison for Inconel®718 | 57 |
| 12. Material Model Constants Using Optimization-Based Approach for the JC Model | 57 |
| 13. Material Model Constants Using Traditional Approach for the JC Model [83]..... | 58 |
| 14. Material Model Constants Using Optimization-Based Approach for the ZA Model | 58 |
| 15. Material Model Constants Using Traditional Approach for the ZA Model [83]..... | 58 |
| 16. Model Constants Using Optimization-Based Approach for the KHL Model | 59 |
| 17. Material Model Constants Using Traditional Approach for the KHL Model | 59 |
| 18. Least Square Error Comparison for Ti-6Al-4V | 69 |
| 19. Viscosity Data of Demonstration Example [86] | 78 |
| 20. Regression Coefficients for Linear Regression Model | 78 |
| 21. Observations, Predicted Values, and Residuals for Demonstration Example [86]..... | 79 |
| 22. Randomly Sampled Error, Predicted Values, and Generated Observations | 80 |
| 23. Bootstrap Error, Predicted Values, and Generated Observations for Fixed-x Bootstrap Method | 87 |
| 24. Material Model Constant Estimates | 95 |
| 25. Latin Hypercube Samples Design Matrix | 105 |
| 26. Response Surface Coefficients | 106 |

FOREWORD

This final report represents the work conducted under Contract No.FA8650-04-D-3446-25 for the Wright-Patterson Air Force Base in Ohio. The report is published to impart technical information and therefore does not necessarily represent the recommendations, conclusions, or approval of the Air Force. The project was managed by Dr. Kristina Langer of Air Force Research Laboratory (AFRL), Wright-Patterson Air Force Base, Ohio. Wright State University was a sub-contractor to GDIT for the project.

The principal investigator, Dr. Ramana V. Grandhi, would like to thank Dr. Kristina Langer, Dr. Pamela Kobryn, and Dr. David Stargel of the Air Force Research Laboratory for their guidance over the course of the project. The principal investigator would also like to thank Dr. Allen Clauer, Mr. David Lahrman, and Mr. Rich Tenaglia of LSP Technologies, Inc., and Mr. Jim Pillers of the Boeing Corporation for their technical advice during all stages of the project. Additional thanks are extended to Dr. Michael Shepard and Mr. Robert Reuter of the Air Force Research Laboratory for their technical assistance throughout the duration of the project.

Dr. Grandhi was assisted by the following team of WSU researchers in both developing and conducting the research work.

Dr. Hemanth Amarchinta
Dr. Jong-Bin Im
Mr. Inseok Park
Dr. Gulshan Singh
Mr. T J Spradlin
Mr. Anoop Vasu
Mr. Dan Gorsky

PREFACE

This is the final volume of technical reports produced for the project *Laser Peening for reliable fatigue life*, Contract No.FA8650-04-D-3446-25. This volume covers the inverse optimization of high strain rate properties from experimental material data, material model validation, and development of a framework for uncertainty quantification of residual stress fields.

The first volume included the 3D simulation of LP, showing the important process parameters, an optimization of the residual stress field from these key parameters, an outline of the optimization strategies applied, and finally finding multiple optima using a modified particle swarm optimization method.

1.0 SUMMARY

Laser Peening (LP) has been advancing as an able substitute for conventional treatments in the process of improving fatigue, corrosion, and wearing resistance of metals. The favorable compressive residual stresses developed by LP can extend further below the surface than the residual stresses from shot peening. Also, it is well suited for precisely controlled treatments of localized fatigue, and critical areas such as holes, notches, and small fillets which might be inaccessible through shot peening. The applicability of LP on complicated geometries provides a unique advantage when compared with other surface enhancement techniques (SET) because laser beams can easily reach intricate locations.

While the processing cost of LP is high compared to its counterparts, advances in simulation accuracy and capabilities will decrease the simulation costs considerably translating to reduction in processing costs through decreased design times. An ideal simulation model will incorporate the laser beam parameters, spatial profiles, overlay conditions, and material properties to increase comparability between simulated and experimental results. The basic effect of process parameters has been extensively investigated and discussed in Volume 1. This report details the effect of material behavior and the uncertainties associated with it when obtaining realistic results from the simulations.

Material models help effectively characterize the material behavior in Finite Element Analysis (FEA). Three material models have been considered to validate the simulation results of experimental results found in literature. The models considered are the Elastic Perfectly Plastic (EPP), Johnson-Cook (JC), and Zerilli-Armstrong (ZA) material models. It was found that for the various conditions the JC model performed best of the three models investigated.

In most cases, there is little experimental data available to compare to simulated results. Using a technique based on inverse optimization, the material behavior was obtained by optimizing the material model constants and reducing the error in predicting residual stresses. Two different materials were tested to validate this approach. The advantage of inverse optimization is that testing for material model constants at strain rates consistent with those experienced in the simulations is that further material model constant testing is not necessary.

This research also develops a framework to determine the uncertainty in the resultant residual stresses from the LP simulation. Material model constants are considered to be uncertain. The uncertainty represents the variability of the material model when characterizing the material behavior. The 'Bootstrapping Method' employed in statistics is used for this process. Two case studies were used to validate this method. Finally, the method was applied to an LP simulation, cementing the suitability of the JC model for LP simulations.

2.0 INTRODUCTION

This chapter introduces the fatigue life issues of the aircraft lug component and the motivation for the development of SET. An introduction to SET is presented. The mechanism of the SET is described, which generates favorable compressive residual stresses in the surface regions. Several techniques such as shot peening, Low Plasticity Burnishing (LPB), waterjet peening, and LP are discussed.

2.1 Motivation

The F-22 Raptor is a fighter aircraft that uses stealth technology. It is primarily an air superiority fighter. The United States Air Force considers the F-22 a critical component of the fleet [1].

Figure 1 shows a picture of two F-22 raptors in column flight formation [2] .



Figure 1: Two F-22 Raptors in Column Flight Formation [2]

To demonstrate the capability of the design, the F-22 aircraft design was subjected to a full-scale fatigue test by Cayton and his co-workers [3]. The main goal of this full-scale testing was to identify any anomalies that remained undiscovered. One such structural problem was found in the form of a crack on one of the lugs of the wing attachments. Figure 2 shows the location of the crack on the aircraft [4]. The lower lugs are important for durability and damage tolerance [3]. The summary of the analysis was that the crack was a result of ForceMateTM expansion levels for the applied load levels. The detailed report is available in the work of Cayton et al. [3]. A configuration change was made in the design of the aircraft and the change was implemented in the manufacturing process for subsequent aircraft. Since there were aircraft already manufactured with the old design, a program has been proposed to increase the fatigue life. This program suggests to use techniques to increase the fatigue life without replacing the component. SET are one possible option that can address the issue.

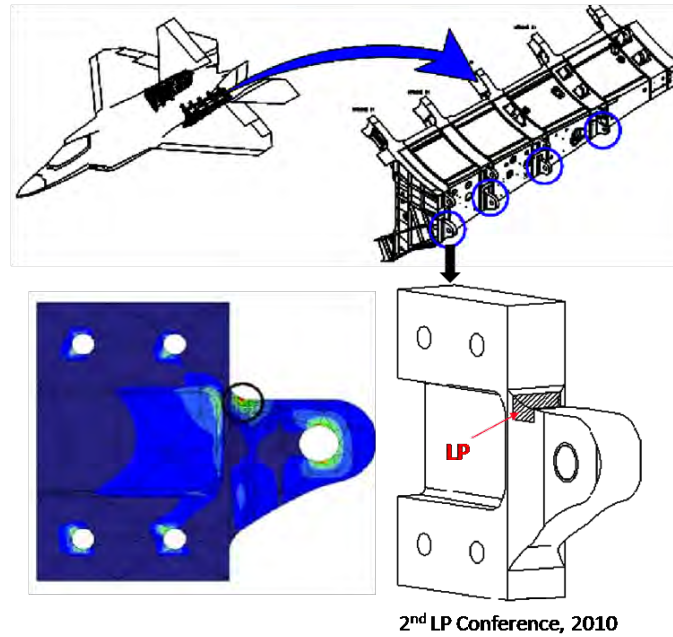


Figure 2: Location of Crack on Lug of an Aircraft Lug [4]

2.2 SET

Highly stressed components such as aircraft lugs, turbine blades from aerospace applications, connecting rods from automobiles, and knee implants from medical applications demand an optimal judgment of material, loading conditions, design, and production processes in the conceptual stages (Figure 3).

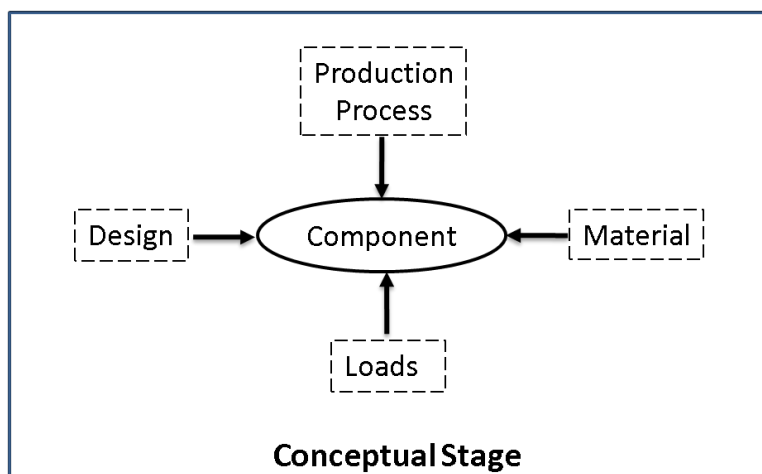


Figure 3: Attributes Considered During Conceptual Stage of a Component

The surface of the component plays an important role under fatigue loading because cracks are initiated from the surface discontinuities such as notches, holes, and voids, ultimately leading to failure. With respect to this, various SET are being used in the industry to mitigate or delay failure. These techniques can be broadly classified [5] as:

1. Mechanical surface treatments
2. Surface diffusion treatments
3. Surface overlay coatings

The basic idea of mechanical treatments is to induce compressive residual stresses on the surface regions. Residual stresses are defined as stresses which exist in the bulk of the material without application of external load. These compressive stresses negate the tensile stresses acting on the surface leading to increased life of the component. Figure 4 shows the basic mechanism for the production of residual stresses in mechanical SET.

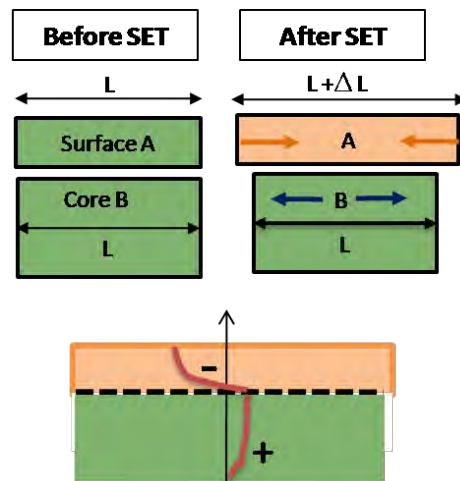


Figure 4: Basic Mechanism to Generate Residual Stresses

Before any pressure is applied to the surface, the length of surface and core are the same. When a high pressure is applied on the surface, shock waves are generated and progress through the depth. This causes plastic deformation in the top region. Since the magnitude of the shock wave decreases as it moves down to the core, it does not produce plastic deformation in the core. To keep cohesion between the stretched surface and the core, the layers in the surface are set to compressive stresses. To maintain equilibrium, compensatory tensile stresses are induced in the core. In this section several of the techniques used in the industry, such as shot peening, LP, LPB, and waterjet peening are discussed.

2.2.1 Shot Peening

Shot peening is one of the traditional techniques used to induce compressive residual stresses. The discovery of improvement in fatigue properties is seen from efforts in 1928 and 1929 by Buick Motor Division [6]. Shot peening is a cold working process in which the surface of the

component is bombarded with small spherical media called shot [7]. Each piece of shot striking the surface acts as a tiny peening hammer, imparting to the surface a small indentation or dimple. A schematic of the process is shown in figure 5.

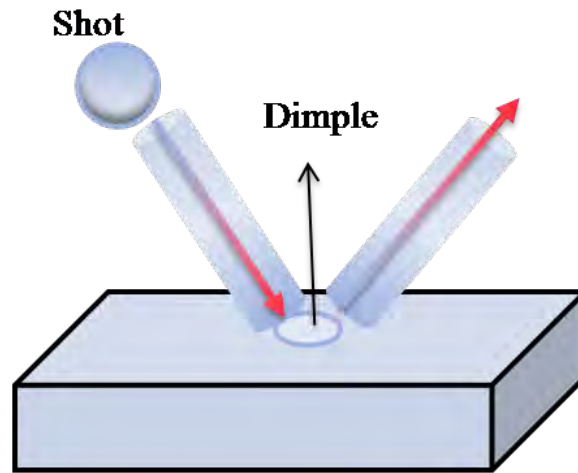


Figure 5: Schematic of the Shot Peening Process

Steel balls are the popular material used for the shot. The most commonly used ball size is 0.05 to 1 mm in diameter. Shot peening has the advantage of low cost and has a successful track record of application to compressor blades [8]. A three dimensional finite element simulation was performed by Meguid et al. using ANSYS [9]. Three main issues addressed in this work were: (i) effect of shot velocity, size, and shape upon the plastic zone development, (ii) effect of the separation distance between two shots on the unloading residual stresses, and (iii) effect of strain-hardening rate of the target upon the spread of the plastic zone. Shot peening has been used in the industry during the past decade. The other advantage of using shot peening is that the cost involved is less compared to other techniques. The process also has disadvantages. The surface finish is damaged due to roughening by the balls. The depth of compressive residual stresses generated by shot peening is relatively low compared to other techniques. This is considered to be one of the major disadvantages of the method [10].

2.2.2 LPB

LPB is a SET developed to induce compressive stresses with higher depth compared to shot peening and minimal cold work [11]. In this process, a smooth, free rolling ball makes a single pass over the material under a normal force just sufficient to plastically deform it. This creates compressive residual stresses on the surface region. The process is shown schematically in Figure 6.

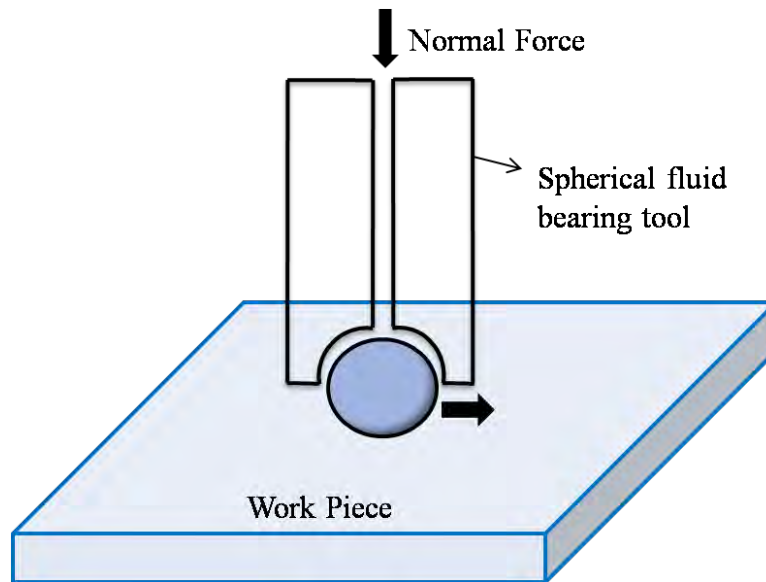


Figure 6: Schematic of the LPB Process

The ball is supported in a fluid bearing with sufficient pressure to lift the ball off of the surface of the retaining spherical socket. The ball is in solid contact only when the surface needs to be burnished. It is free to roll otherwise. The force is applied from top and the tool position is generally computer controlled [12]. LPB has been used in medical field for hip stems [13]. The LPB process was developed and applied to the modular neck taper junction of total hip prosthesis. The advantages of LPB are its low cost and minimal cold work. The disadvantage of this technique is that it cannot be applied to complicated geometries such as a mechanical gear.

2.2.3 Waterjet Peening

Waterjet peening is very similar to shot peening, but instead of using balls, water with high velocity is impinged upon the target [14]. A schematic of the process is shown in Figure 7.

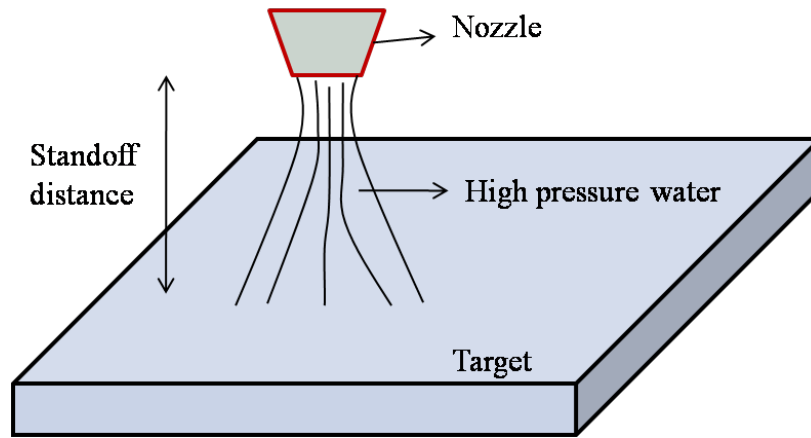


Figure 7: Schematic of the Waterjet Peening Process

The waterjet generates a pressure distribution, creating localized plastic deformation. This deformation is restrained by surrounding material, leading to compressive residual stress in the surface regions. The advantages of waterjet peening compared to shot peening are a better surface finish and increased coverage capabilities. The disadvantage is that the magnitude of residual stress is lower than other treatments and low controllability. There are various parameters such as water pressure, nozzle feed speed, peening duration, nozzle and peening angle that control the magnitude of residual stresses [15]. Various approaches [16, 17] are available for mathematical modeling of the process that vary from closed form differential equations to finite element method.

2.2.4 LP

LP is a very high powered process with a short interactive time. It requires a laser power density on the order of 10^9Wcm^{-2} with pulse duration in nano seconds. Figure 8 shows a schematic of the process.

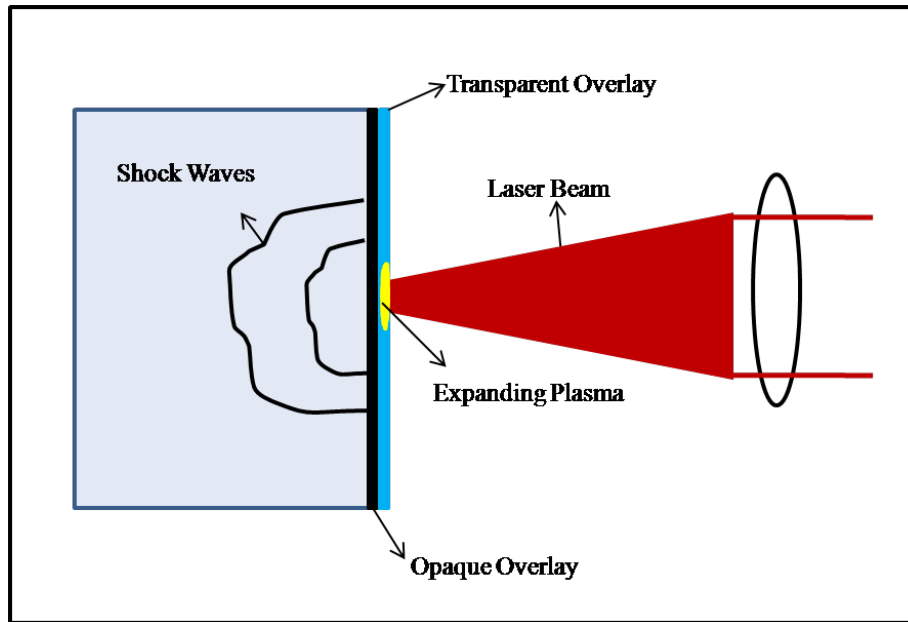


Figure 8: Schematic of the LP Process

In the LP , a laser beam is fired at an opaque overlay (example: black paint) applied to the surface of the component to be laser peened. The opaque overlay is covered in turn with a transparent overlay such as water. This water overlay can either be running or still water. The vaporization of the opaque overlay produces a plasma confined between the two overlays. The pressure exerted on the material surface by the expanding, confined plasma generates shock waves that propagate into the target. Depending on the laser parameters, if the magnitude of shock waves is high enough, the material plastically yields, resulting in compressive residual stresses in the surface regions. The formation of plastic strain by shock waves continues until the peak stress wave decreases below the dynamic yield strength. Compensatory tensile stresses are also created inside the target. Details about the process can be found in the review papers of Peyre and Fabbro [18] and Mantross et al. [19]. The advantage of the LP process is that it can be performed on complex geometries and involves no contact with the component. Compared to the shot peening process, LP achieves higher depth of compressive residual stress.

2.3 Section Summary

Fatigue life issues in engineering structures are introduced with focus on aircraft component. A basic mechanism of SET is introduced. Various SET are briefly described including advantages and disadvantages.

3.0 BACKGROUND

This chapter provides the background details on the LP process. Evolution of the LP process in a historical perspective is described. A review of LP experiments performed on different materials is provided. The parameters involved in the LP process for a successful implementation are discussed. A review of the simulation of the LP process is discussed and the advantages and limitations of the work are provided. Also, a review of uncertainty quantification methodologies relevant to spatial structural response such as residual stresses is detailed. The limitations of the review leads to the definition of research need.

3.1 Historical Perspective

The history and evolution of the LP process has been described in detail by Clauer [20]. Clauer divided the time between the discovery of the phenomenon in 1960, to the phase into production in the 1990 into stages. The first experimental generation of shock waves in a laboratory was performed by White [21] in 1962. The shock waves were generated by electron bombardment and electromagnetic wave absorption. The experiments were conducted in a vacuum chamber and peak power densities of $44W/cm^2$ were achieved. Gregg and Thomas [22] and Skeen and York [23] were a few of the researchers who extended the investigations on characterizing the momentum transfer phenomena for the laser induced plasma. The enhanced pressure was achieved by the use of the transparent overlay was discovered by Anderholm in the 1970 [24]. Stress measurements were made using quartz gauze. Aluminum foil and quartz disk were used as overlays. Although the experiment was performed in a vacuum chamber, the pressure enhancement can also be achieved in air. The benefits of laser-induced shock waves in material properties were identified by Malozzi and Fairand, who were awarded the patent in 1974 [25]. There were additional patents awarded until the present date in various applications of LP.

During the 1970 and early 1980 efforts were made to model laser material interaction using LILA and TOODY codes. Many of the efforts were made towards understanding the effects of laser processing parameters on fretting fatigue, hardening, galling, and wear of metals. Clauer and Fairand demonstrated that compressive residual stresses were a contributing factor to the increase in fatigue life of metallic components [26]. The first step into production was made in early 1990's, when LP was used on several F101 fan blades to reduce the foreign object damage. The goal at the current stage is to lower the processing cost and to engineer the process parameters for new applications.

3.2 Experimental Attribute of LP

The LP process has three major ingredients for a successful application. They are (i) laser system, (ii) opaque overlay, and (iii) transparent overlay. This section gives a brief description about each of the three.

3.2.1 Laser Systems

The laser system for the LP process is not one of the standard laser systems available in the industry. These system have to be custom built because the minimum energy required is 20

Joules/pulse, whereas the standard in the industry is 3 Joules/pulse. The wavelength of the system is very important because it controls the interaction with the target to generate the shock waves. The wavelength should be about $1\mu m$. These constraints reduce the large variety of laser systems available to two or three viable possibilities. Pulsed CO₂ laser systems are proven to be efficient and durable, but they have a characteristic wavelength of $10.6\mu m$ that makes them infeasible for the LP process. Currently, neodymium-glass laser is the most suitable candidate. Detailed description of the selection of laser systems is provided by Shepard [27] and Fairand and Clauer [28]. The experiments performed by Fairand and Clauer [29] used a Q-switched neodymium-glass laser that consisted of an oscillator followed by six amplifier stages. The system was capable of emitting up to 500 J of laser energy in a pulse with a full width at half maximum (FWHM) of 20-40 ns. Peyre et al. [30] used a Nd-glass prototype laser operating at a wavelength of $1.06\mu m$ followed by four amplifier stages. This system is capable of emitting up to 80 J in a pulse that is semi-gaussian and short rise time (SRT) in shape with a FWHM of 15-30 ns.

3.2.2 Opaque Overlay

The opaque overlay in the LP process serves two purposes. First, vaporization of the opaque overlay forms plasma that generates the shock waves inside the target, creating favorable compressive residual stresses. Second, it acts as a protective layer for the target. Various materials such as Al, Zn, Pb, and black paint have been used as opaque overlays. It has been shown by Fairand and Clauer [29] that all opaque overlays produce nearly the same shock wave pressures after crossing certain laser power density. The thickness of the black paint is typically $8 - 10\mu m$. Self-adhesive foils were proven to be better in certain conditions compared to protective coatings [31]. The practical advantage of black paint compared to others has made it attractive in the commercial LP process.

3.2.3 Transparent Overlay

The presence of transparent overlay is known as confined regime, compared to direct regime, which does not have any confining overlay. The earlier experiments that induced shock waves by laser systems did not include transparent overlays. Transparent overlay was first used by Anderholm [32, 24]. The intensity of shock waves due to confinement by transparent overlays is up to two orders of magnitude higher than plasmas generated in vacuum [33, 34, 35]. According to Peyre et al. [36], the pressure of shock waves is five to ten times higher in magnitude and two to three times longer in duration than direct regime. Fused quartz, glass, polymeric material and distilled water have been used successfully as a transparent overlay. Water is the most widely used in the commercial LP process. This water can be either running water or stagnant water.

3.3 Review of Simulation of the LP Process

One of the major disadvantage of the LP process is the cost involved. The fixed cost to set up the laser system is high, and the variable operating costs for particular applications are also high. One reason for higher operating costs can be attributed to the current industry practice of performing LP experiments and then obtaining the optimum process parameters for each application. Simulation of the LP process not only reduces the requirements for expensive trial-and-error

experiments, it also helps in engineering the process parameters. The review of the simulation of the LP process is described here in chronological order.

The first finite element simulation to predict residual stresses from the LP process was reported in 1999 by Braisted and Brockman [37]. The methodology of sequential switch from explicit to implicit algorithms for efficient computation was developed. They also introduced finer and infinite elements to take advantage of the localized effect of the LP process. Constitutive behavior of elastic perfectly plastic material behavior was assumed. Nam and co-workers from The Ohio State University developed their own finite element code called SHOCKWAVE to model the residual stresses induced by the LP process [38]. The JC material model was used for the constitutive behavior. Single-side and double-side LP were modeled. The shock wave profile was measured by using streak cameras and quartz gages by LSP Technologies, LLC. The shock wave has temporal and spatial profile. Experimental results were provided by LSP Technologies. Research efforts to model the LP phenomenon were carried out independently in Saudi Arabia, France, and Australia in 2003. Researchers in Saudi Arabia worked on two aspects of modeling the LP process. The first one included developing analytical equations for temperature during plasma generation, recoil pressure calculations, and wave analysis for plastic deformation [39]. The second work focused on numerical prediction of the depth of plastic deformation and compressive residual stresses [40]. Finite difference scheme was used to simulate the propagation of stress waves coupled with finite element models. Peyre et. al from France used ABAQUS for the prediction of residual stresses. The JC model with Equation of State (EOS) was used as the procedure for material behavior. Axisymmetric mesh with infinite elements was used to represent the structure. Velocity Interferometer System for Any Reflector technique was used to predict the loading conditions. Ding and Ye developed the first 3D simulations for prediction of residual stresses [41]. They also developed the two-sided LP process [42]. EPP constitutive model was assumed for the material behavior. History of energies was used as a stopping criteria for ABAQUS/Explicit. The 3D simulations were also modeled by Ocana and his co-workers [43]. Multiple overlapping shots, which were neglected in the previous work were modeled using ABAQUS. Wu and Shin from Purdue University developed a complete model for simulating the residual stresses induced by the LP process. Their first work was published in 2004 [44], and their work continued until recently in 2007 [45]. Most of the work involved developing analytical equations for converting the laser pulse to pressure pulse. According to them the plasma generated from the LP process is divided into breakdown and confined plasma. Only the confined plasma is able to produce the shock waves. There is no need for any measurement of shock wave pressure magnitudes. Inputs are needed for the laser equipment such as power density, laser wavelength. The modeling procedure predicts the residual stresses. The JC model was used as constitutive model. The recent work in modeling the residual stresses include Peyre et al. and Warren et al. in 2007 [46] and 2008 [47] respectively. The main goal of Peyre and his co-workers was to investigate the influence of protective coatings, and precise simulation of thermo-mechanical uncoated LP process. Shock propagation and attenuation was modeled in ABAQUS/Explicit, and thermal modeling of plasma heating was modeled in ABAQUS/Standard. Thermo-mechanical residual stresses were predicted by combining the results of ABAQUS/Explicit and ABAQUS/Standard. Warren et al. performed 3D simulations of single and multiple shots. A user subroutine, VDLOAD, was developed in ABAQUS to include spatial and temporal variation. Spot size effect, spacing effect, and intensity effect on residual stresses were

investigated. Srinivasan [48] developed simulation work for the spallation response, caused by the LP process through strain rate and temperature dependent material models. The JC and modified ZA models were used as material models. The constants were obtained from other references. The most recent work [49] involves 3D simulations on curved surfaces for geometric effects on residual stress predictions. This is the first effort to simulate a three dimensional curved geometry. There were no experimental comparisons in their work.

3.4 Review of Relevant Uncertainty Quantification Research

Uncertainty quantification provides an alternative to conventional deterministic analysis. The uncertainty is taken into consideration in deterministic analysis by employing the safety factor approach. This safety factor accounts for the uncertainties in the design, manufacturing, and other factors in making the final product. While deterministic approach with safety factor have been used with success in the past, they tend to be over conservative. Today's increased demand for higher efficiency, better performance and lower cost makes it necessary to consider developing techniques to quantify these uncertainties. Probability theory has been widely used to quantify the response caused by uncertainties in inputs. Non-probability based methods exist, such as fuzzy set theory [50, 51], evidence theory [52], and information-gap theory [53]. Uncertainties can be broadly categorized as model uncertainty and parametric uncertainty. Model uncertainty is caused when there are different models to represent the same physical situation. Choosing one model over other is referred as model uncertainty. Parametric uncertainty is caused within a model. It is caused due to variations in the input parameters for a simulation model. The uncertainties can also be classified into two categories: aleatory and epistemic. Aleatory uncertainty is irreducible or inherent uncertainty. Epistemic uncertainty is a result of lack of knowledge or data, and therefore is a reducible uncertainty. There are many ways to characterize the uncertainty in the inputs and propagation of the input uncertainty through a physics-based simulation or analytical equation. The final goal is to predict the uncertainties in the response of the systems caused by the uncertainties in the inputs.

Sampling methods are the most common method to quantify uncertainty in system response. New methods that are developed are often compared with a sampling method for verification. The computational cost of sampling methods makes it impractical for implementation. Monte Carlo Simulation (MCS) technique with Latin Hypercube Sampling (LHS) is a popular sampling method [54]. The drawback of the LHS is its inefficiency to sample for correlated input random variables. This limitation has been recently addressed and an extension to the existing LHS technique is developed to incorporate correlation between the variables [55].

Techniques based on limit state function were developed. These include First Order Reliability Method (FORM) and Second Order Reliability Method (SORM). In FORM, the limit state is approximated by linear approximation at the Most Probable Point (MPP). The accuracy of the FORM depends on failure surface. FORM is most accurate when the limit state is nearly linear in the vicinity of MPP. FORM predicts inaccurate results when the failure surface is nonlinear. If the failure surface is approached by second order approximation at the MPP it is SORM. The addition of second order term increases the efficiency, but also increases the computational cost. The MPP-based methods can be based on high quality function approximations [56]. This is

based on standard normalized system. Performance measure approach [57] is developed that is shown to be more stable and efficient than reliability index.

Approximate integration methods have been developed to estimate the statistical moments of the response. Univariate dimension reduction method was developed by Rahman and Xu [58] for numerical integration of multi-dimensional integration. It converts a multidimensional integration into multiple one dimension integration. Recently this method has been extended by Youn et al. by including eigenvector sampling technique among other developments [59]. Penmetsa and Grandhi have adapted the fast fourier transformation (FFT) technique to estimate the structural failure probability [60]. Convolution integral is converted into multiplication by use of FFT. Two point adaptive nonlinear approximation is used at the MPP.

Spatial variability is another form of uncertainty that quantifies variability in the structural response. Choi et al developed framework by considering random field variations [61]. The effect of spatial variation in Young's modulus on the responses such as displacement is shown in the work. The framework developed involved use of Karhunen-Loeve transformation for reducing the number of input random variables. Polynomial chaos expansion is used to construct approximation. Analysis of variance is performed for significance test. Probabilistic analysis of residual stress (spatial structural response) is performed by Millwater and his co-workers [62, 63]. In the first work, the residual stress is modeled as probabilistic in nature by a random scaling factor. The main objective was to identify the effect of residual stress on probability of fracture for a compressor disk. Other random variables that were considered in the design process were initial crack size distribution, crack propagation scatter, and stress scatter. An extension to the work is performed by assuming random residual stress field. Two analytical models were fit to the experimental data using nonlinear regression analysis. The randomness in the estimates obtained were utilized further to obtain confidence bounds on the residual stress field. Khaled and Noor [64] examined the effect of uncertainty in the material properties of steel associated with martensitic transformations on the residual stress field induced by the welding process. They used a fuzzy-set approach to quantify the uncertainty in material properties. The main conclusion was that the variation in material properties has a significant effect on welding residual stress field. Grujicic et. al. [65] quantified the effect of material and processing parameters on the magnitude and distribution of the axial residual stress on gun barrels. Advanced mean value method, which is based on limit state concept. was adapted to determine the cumulative distribution of residual stress. Sobczyk and Trebicki [66] proposed one to three parameters to model the random residual stress on fatigue crack growth. The probabilistic model of residual stress was included in their evaluation of stress intensity factor and calculations of crack growth life. The Forman fatigue crack growth equation was used to obtain the cycles to failure. Park and his co-workers [67] have developed an approach based on bayesian statistics to quantify the model uncertainty by using the measured differences between the experimental data and simulation predictions. Model probability, that is defined as the degree of belief that a model is the best approximating model among a model set is estimated using the experimental data. The methodology is applied to obtain a confidence band on the residual stress field induced by the simulation of the LP process.

3.4.1 Sources of Uncertainty in LP Simulation

Different sources of uncertainty exist during the simulation of the LP residual stresses. Figure 9

shows an overview of these different sources. The uncertainties can be categorized as:

1. Model Uncertainty
2. Parametric Uncertainty
3. Shape Uncertainty
4. Regression Uncertainty

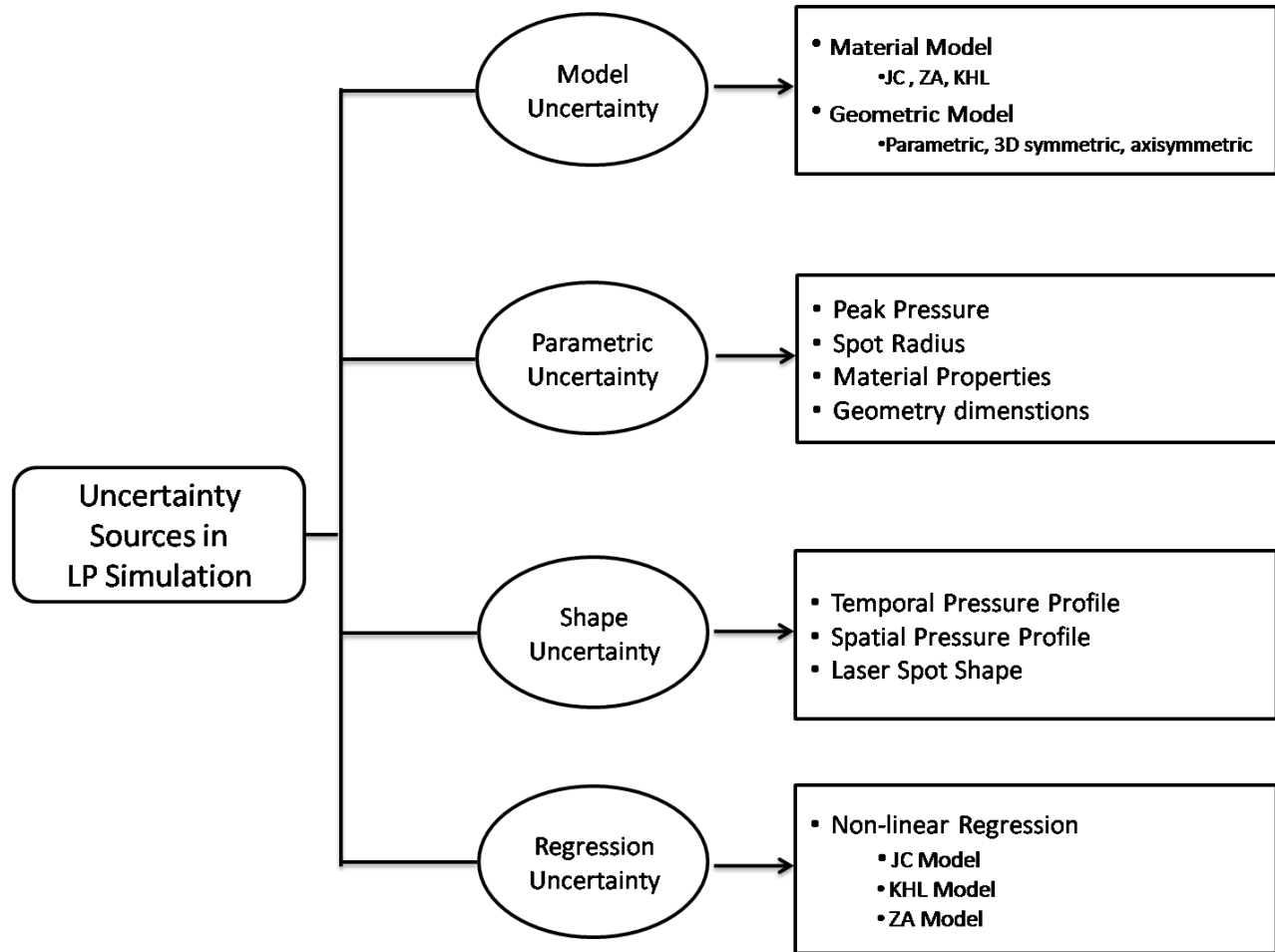


Figure 9: Sources of Uncertainty During LP Simulation

Model uncertainty is defined as the uncertainty involved in selecting the best model from the possible models to represent the physical scenario. Details regarding model uncertainty can be found in the work of Park [67]. An example of model uncertainty would be selecting the best material model from among the JC model, ZA model, and EPP model to predict the material behavior based on limited experimental data.

Parametric uncertainty arises due to uncertainty in the input process parameters. Parametric uncertainty can be categorized as aleatory or epistemic, based on the availability of experimental

data. Examples of parametric uncertainty are: i) peak pressure of the shock wave, ii) laser spot radius, iii) geometric dimensions, and iv) material properties.

Shape uncertainty is defined as the uncertainty in shape of the input profiles that are essential for the LP simulation. Examples of shape uncertainty include temporal and spatial profiles of the shock wave. The shape of the laser spot acts as a shape uncertainty for 3D models.

Regression uncertainty is defined as the uncertainty in the model constant estimates obtained from the fit of the constitutive material model to the experimental data. Regression uncertainty represents the uncertainty in the material model used to predict the material behavior.

3.5 Definition of Research Need

The review of the research in simulation of the LP process and uncertainty quantification leads to three major research needs. These three research needs are separated into two groups. The first group is advancements in finite element simulation of residual stresses induced by the LP process, and the second group is development of uncertainty quantification framework for spatial structural response such as residual stress.

Due to the complexity of the process, development of reliable and accurate simulation that can be used in process design is a challenging task. There have been disagreements between experimental and simulated results in previous work. The LP process has many parameters that need to be precisely determined for an accurate finite element simulation. Among them are pressure profile, laser spot, and material model. The first two parameters depend on the laser system being used in experiments. During the LP process the component experiences strain rates of $10^6/s$. This work emphasizes the need for an accurate material model because the material behaves significantly different at such high strain rates. There has been no work reported on validation of material model for the simulation of the LP process.

Secondly, most of the materials used for simulation in the previous work had little experimental data of the material behavior. This insufficient or little experiment data was used to predict the model constants. The material model was extrapolated for higher strain rates, where there was no experimental data available. In this work, LP experiments on Inconel®718 were performed in collaboration with LSP Technologies. For Inconel®718 material, no experimental data of the material behavior for room temperatures at high strain rates were found. The simulation of the LP process for materials which don't have any experimental data is non trivial.

Thirdly, uncertainty quantification of spatial structural response, such as residual stress from the LP process is needed. No framework has been developed in the literature. A methodology needs to be developed to obtain confidence bounds on the residual stress. Robust design is an important aspect that must be addressed, because small difference in estimation of compressive residual stresses leads to an order of magnitude in the fatigue life estimates.

3.6 Project Scope and Organization

This section describes the scope of the project. Figure 10 provides the overview of the project. The main goal of the research is to develop a method to quantify uncertainty in the LP residual stresses due to regression uncertainty.

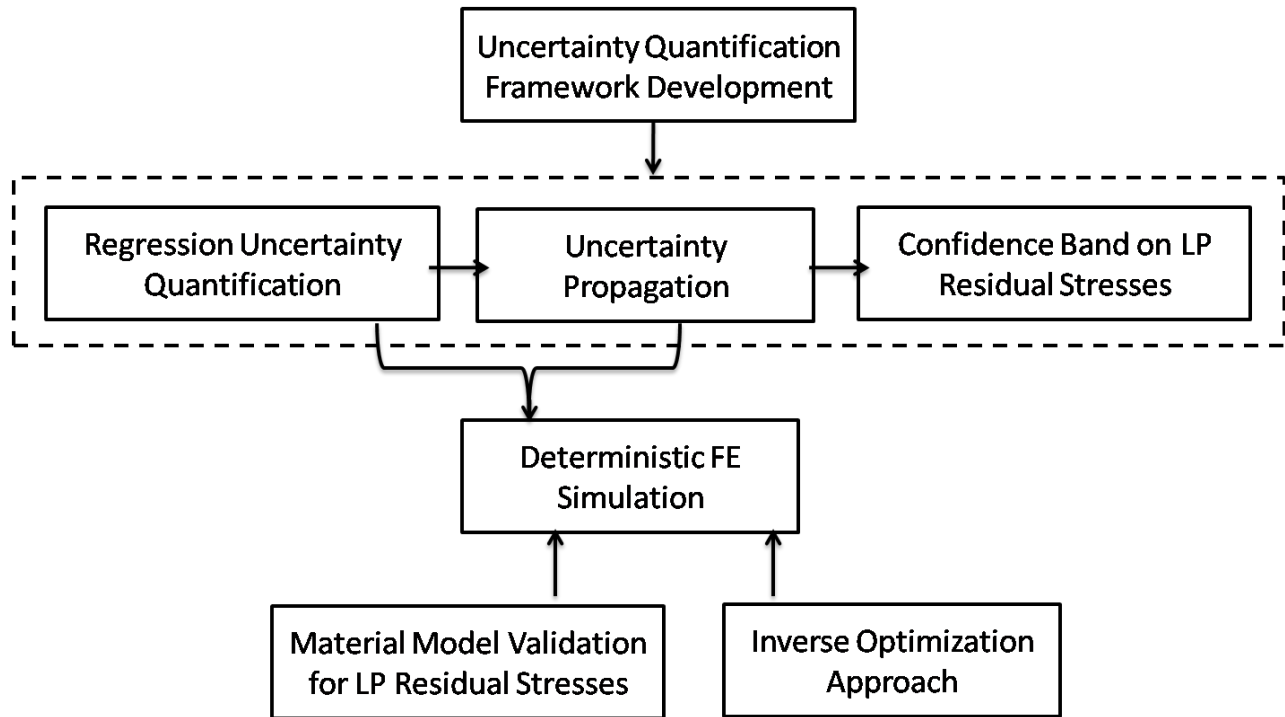


Figure 10: Project Scope

The framework is comprised of three components: (i) regression uncertainty quantification for material model, (ii) uncertainty propagation to LP residual stress, and (iii) confidence band on LP residual stresses. Regression uncertainty represents the variability in the model constant estimates from the non-linear regression analysis. A statistical technique known as bootstrap for regression is adapted to validate the normality assumption of the model constant estimates. For the uncertainty propagation, a Taylor series expansion is used as an approximation to propagate the regression uncertainty through the FEA. The final confidence band of the LP residual stress is obtained for the entire depth.

LP has many process parameters that must be precisely determined for an accurate finite element simulation. Among them are pressure profile, laser spot, and material model. This research investigates different material models and validates them with experimental results. An optimization-based methodology is implemented for identifying material models to simulate the LP residual stresses when very little experimental data of material behavior is available. The project is organized as follows.

Chapter 4 describes the details of the finite element simulation procedure. Figure 11 shows the four major components of an LP simulation. In this work, research is conducted in the material behavior component. Material model validation for the simulation of the LP residual stress is described.

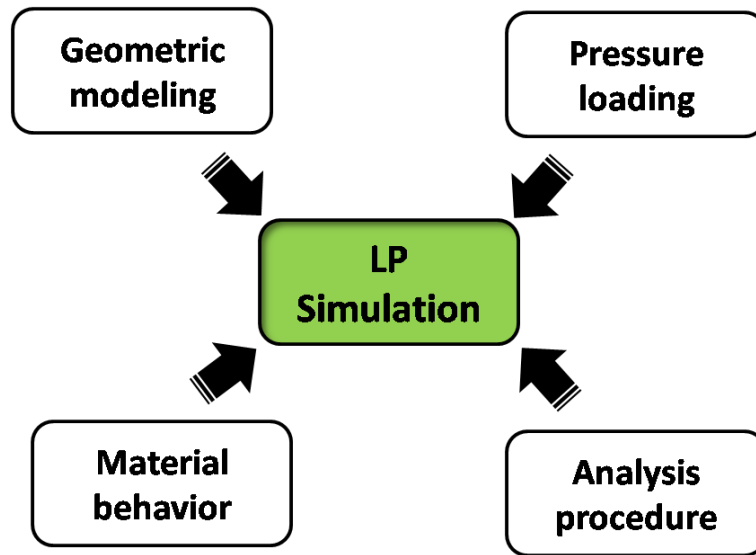


Figure 11: Simulation Overview

Three different constitutive material models are used for validation purposes: the EPP model, the JC model and the ZA model. The analysis procedure and geometric modeling are also described.

In Chapter 5, simulation of the LP process for Inconel®718 material is described. An optimization-based methodology is implemented to predict the LP residual stresses. This inverse optimization approach obtains the model constants from the experimental data at one peak pressure and predicts the residual stress at other peak pressures. The advantage of this approach is that the results obtained from the simulation will be consistent with the experimental results. The power of the approach can be seen when there is very little or no stress-strain data available at different strain rates.

In Chapter 6, the framework to obtain the confidence bounds on the residual stress is described. A generic definition of the bootstrapping technique is described and an example is provided. The technique of bootstrapping for regression is also described. The two categories of bootstrapping for regression are defined, and an example for each method is provided. Two demonstration examples are provided to validate the uncertainty framework. The developed framework is implemented for the JC model and the confidence band for the LP residual stresses is obtained.

4.0 MATERIAL MODEL VALIDATION FOR LASER PEENED RESIDUAL STRESSES

This chapter provides brief details of the Laser Peening (LP) process with reference to the simulation procedure. Constitutive material model advantages and disadvantages. The simulation procedure is described followed by results and discussion.

4.1 Laser Peening Description With Reference to Simulation

The LP process is comprised of two parts. The first part is the quick process of laser firing and the second part is the slow recovery of the component to equilibrium. The laser firing part is a highly intense process. A high powered laser with intensity of the order of $10^9 W/cm^2$ is focused on an opaque overlay. The laser is in contact with the opaque overlay for a few nano seconds. Firing the laser on the component creates shock waves that travel inside the component to create compressive residual stresses on the surface regions. The relaxation of the material to achieve equilibrium is a relatively slow process compared to laser firing. During the simulation of the LP process, this mismatch of time is modeled using ABAQUS/Explicit and ABAQUS/Standard for efficient computation.

4.1.1 Thick and Thin Geometries

This section describes the overview of the simulation models that can be developed for the LP simulation. Figure 12 shows the overview.

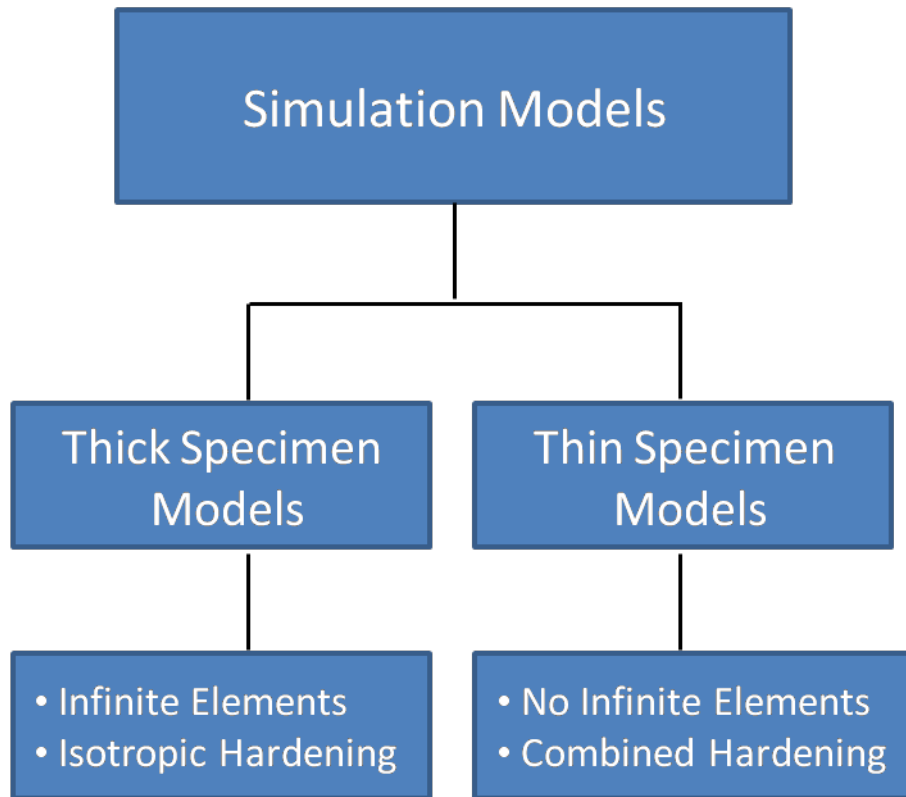


Figure 12: Overview of Simulation Models

The simulation models can be divided into two categories, i) thick specimen models ii) thin specimen models. Thick specimen models are defined as the models where the shock waves that are reflected from the bottom surface are not significant. There is no standard way of defining the exact thickness that differentiates the specimen. It depends on the material being used and also on the process parameters. Infinite elements are used for the thick specimens that represent the boundary condition of shock waves not reflecting back. Isotropic hardening works well for the thick specimens. For modeling the thin specimens, infinite elements cannot be used since the shock waves that reflect back are significant in prediction of the residual stresses. A combined hardening model must be used since isotropic hardening does not capture the effect of shock waves from both the direction. All the models developed in this work are for thick geometries.

4.2 Material Model Details

The plastic deformation during the LP process is caused by laser-induced shock waves. The waves that causes stresses beyond the yield limit is generally referred to as plastic waves. These plastic waves are known as shock waves when the wave front is steep. LP is a very high strain rate process. The component can experience strain rates up to $10^6/s$, which is very high compared to conventional strain rates. At low strain rates the material behavior is independent of strain rates. The material response to impact loading may be significantly different from static or quasi-static loading [68]. Accurate material modeling is needed to simulate the material behavior. Various

constitutive models have been suggested by researchers such as Bodner [69], Miller [70], Bommann et al [71], Johnson and Cook [72] and Zerilli and Armstrong [73] for different applications. The later two models are investigated in this work along with the EPP model because of their popularity in literature.

4.2.1 The EPP Model

In the EPP model, no strain hardening and/or strain rate dependence of flow stress is considered. Once the plastic regime is reached, the stress remains constant. The yield stress is derived based on Hugoniot elastic limit (HEL) because LP is a shock wave phenomenon. HEL is defined as the axial stress required for plastic deformation under uniaxial strain conditions. It is assumed that yielding occurs when the stress in the direction of shock wave reaches the HEL. The relationship between HEL and yield strength (σ_y) is shown in Equation 1:

$$\sigma_y = HEL \frac{(1 - 2\nu)}{(1 - \nu)} \quad (1)$$

where ν is Poisson's ratio. The advantage of this model is that only a small amount of data is required to estimate the yield stress. The disadvantage is that it does not account for strain hardening and/or strain rate dependence.

4.2.2 The JC Model

The JC model is one of the most frequently used models for impact studies [72]. The JC model describes the flow stress of the material as a product of three terms: a strain hardening term, a strain rate dependent term, and a temperature term. It is described in Equation 2:

$$\sigma = [A + B\varepsilon^n] \left[1 + C \ln \frac{\dot{\varepsilon}}{\dot{\varepsilon}_0} \right] [1 - T'^m] \quad (2)$$

where A , B , n , C , $\dot{\varepsilon}_0$, and m are experimentally determined constants. ε and $\dot{\varepsilon}$ are strain and strain rate, respectively. T' is a non-dimensionalized temperature:

$$T' = \frac{T - T_r}{T - T_m} \quad (3)$$

T_r and T_m are room temperature and melting temperature, respectively. Parameter A is the initial yield strength at room temperature. Parameters B and n take strain hardening into account, while parameter m models the thermal softening. Parameter C represents strain rate sensitivity. The main advantage of the JC model is that the estimation of the parameters is simple and easy because it allows for isolation of the three effects.

4.2.3 The ZA Model

The ZA constitutive model is based on dislocation mechanics and the crystal structure of the material [73]. There are several generations of the model. Initially, the model addressed Face Centered Cubic (FCC) and Body Centered Cubic (BCC) structures. The flow stress relationship is shown in Equations 4 and 5 for FCC and BCC structures, respectively:

$$\sigma = C_1 + C_5 \epsilon^n \exp(-C_3 T + C_4 T \ln \dot{\epsilon}) \quad (4)$$

$$\sigma = C_1 + C_2 \exp(-C_3 T + C_4 T \ln \dot{\epsilon}) + C_5 \epsilon^n \quad (5)$$

C_1 , C_2 , C_3 , C_4 , C_5 , and n are material constants that need to be determined. C_1 , C_5 , and n are similar to A , B , and n , respectively, of the JC model. The work has been extended to include strain recovery for Hexagonal Closely Packed (HCP) metals [74]. Equation 6 shows the constitutive model

$$\sigma = \sigma_a + B e^{-(\beta_0 - \beta_1 \ln \dot{\epsilon})T} + B_0 \sqrt{\epsilon_r (1 - e^{-\epsilon/\epsilon_r})} e^{-(\alpha_0 - \alpha_1 \ln \dot{\epsilon})T} \quad (6)$$

where σ_a , B , β_0 , β_1 , B_0 , ϵ_r , α_0 , and α_1 are the constants that need to be estimated. The term in the square root is the strain recovery term. This addresses the shear instability, an important consideration for HCP structures (Ti-6Al-4V). The ZA model considers the interaction effect between strain rate and temperature. The disadvantage of the ZA model is that it has a high number of constants that must be determined.

4.2.4 Parameter Estimation

Ti-6Al-4V material is used in this work. The material properties are listed in Table 1 [38].

Table 1: Material Properties of Ti-6Al-4V

| Property | Value |
|-------------------------|-------|
| Young's Modulus (GPa) | 113.8 |
| Poisson's Ratio | 0.342 |
| Density ($kg m^{-3}$) | 4500 |
| HEL (MPa) | 2800 |

The material constants for the JC and ZA models are estimated by fitting the experimental data of stress-strain curves for different strain rates [75]. Although more recent experimental data is available in the literature [76], these results are not used because the experiments were conducted on low grade Ti-6Al-4V, which is not used for aerospace applications. Higher strain rate experiment data [77] was found and will be used for the simulation in the next chapter. Equation 6, which considers the strain recovery term, is used as the ZA material model. Temperature effects are not considered in this work because LP is a mechanical process [78]. MATLAB's lsqcurvefit [79] function is used for fitting the experiment data. lsqcurvefit is a nonlinear curve fitting function in a least square sense. Figures 13 and 14 show the fit to the experimental data for the JC and ZA models respectively.

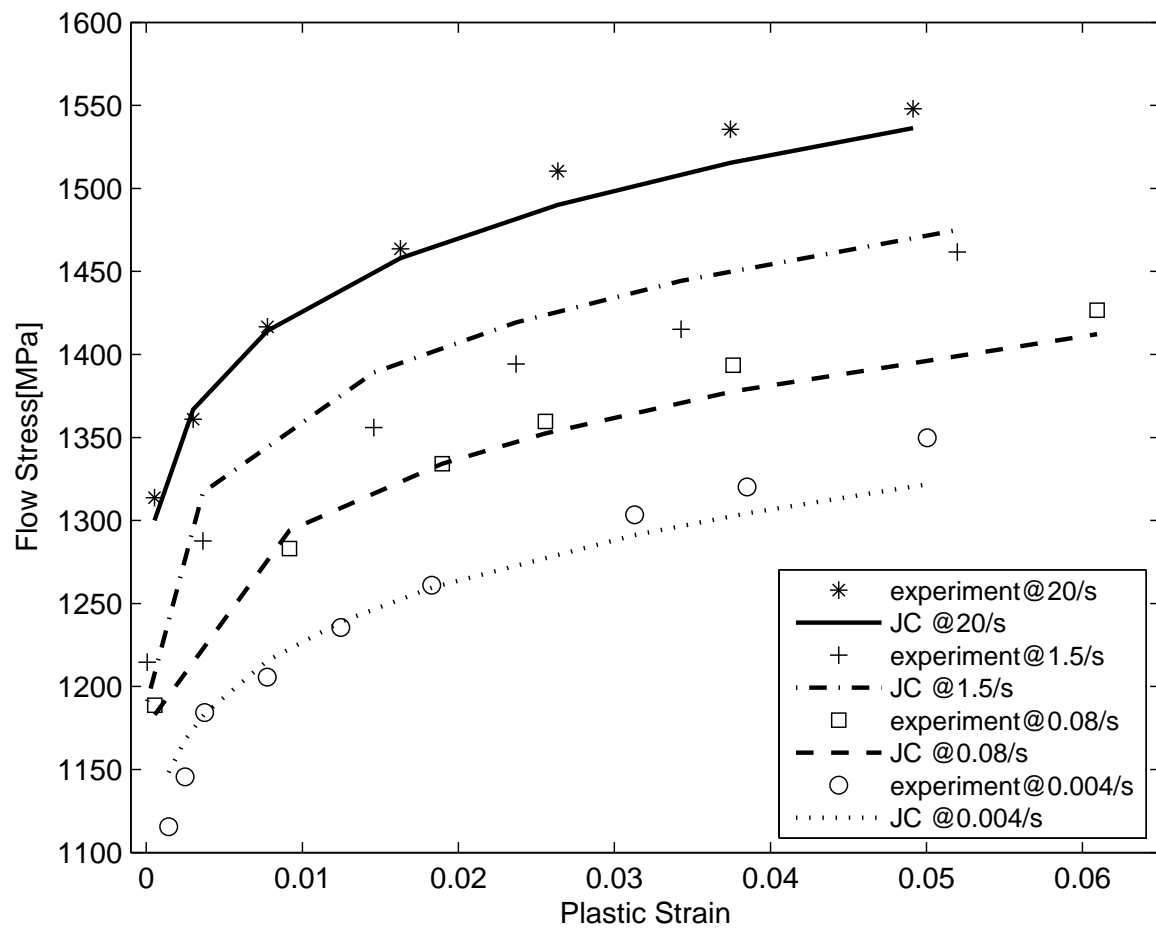


Figure 13: The JC Model Fit to Experimental Data [75] of Multiple Strain Rates

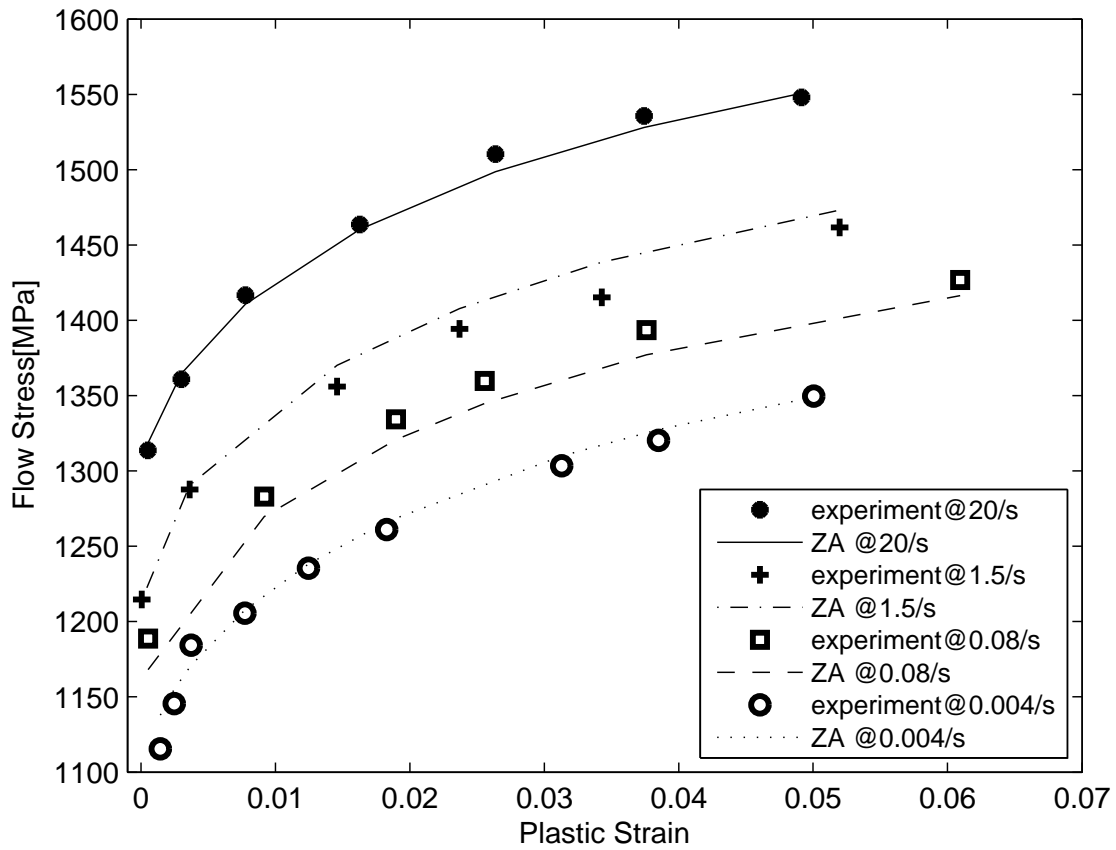


Figure 14: The ZA Model Fit to Experimental Data [75] of Multiple Strain Rates

The constants obtained for the JC model and the ZA model are shown in tabular format in Tables 2 and 3.

Table 2: Model Constants for the JC Model

| Parameter | Value |
|--------------------|--------------|
| A | 950.228 MPa |
| B | 603.3825 MPa |
| n | 0.1992 |
| C | 0.0198 |
| $\dot{\epsilon}_0$ | 0.0009/s |

Table 3: Model constants for the ZA Model

| Parameter | Value |
|-----------------|-------------------------|
| σ_a | 945.1961MPa |
| B | 246.6467MPa |
| β_0 | 1.1636×10^{-6} |
| β_1 | 0.1065 |
| B_0 | 1481.249 MPa |
| ε_r | 0.0538 |
| α_0 | 10^{-6} |
| α_1 | 3.1564×10^{-4} |

Figures 15 and 16 show the strain rate dependence curves at different strains for the JC and ZA models.

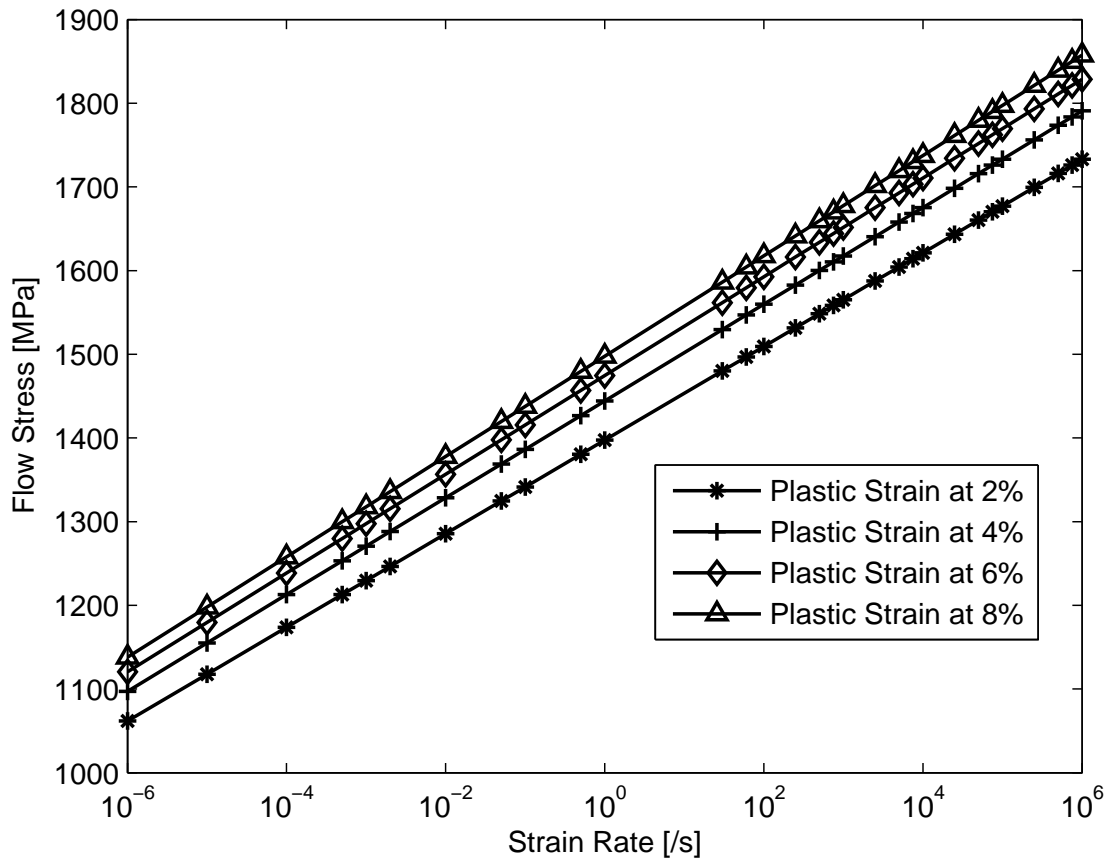


Figure 15: Strain Rate Dependence Curve for the JC Model

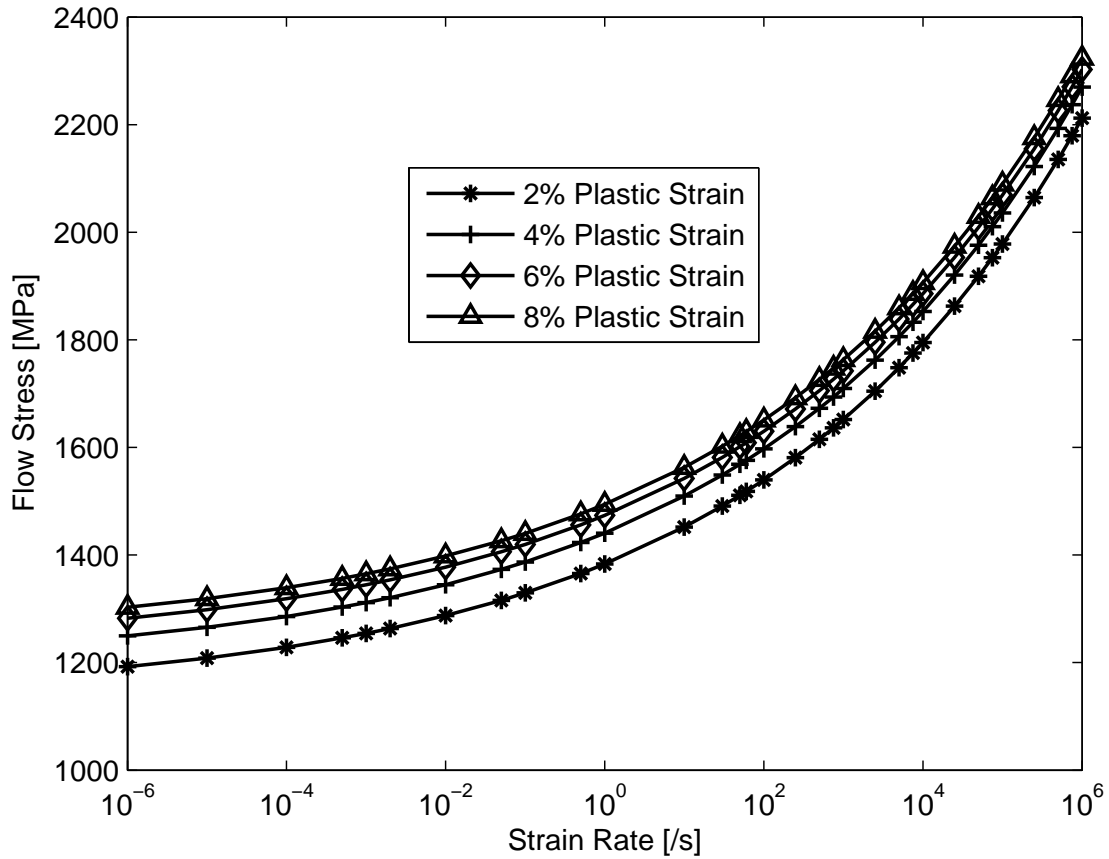


Figure 16: Strain Rate Dependence Curve for the ZA Model

These figures indicate that for the JC model, the stress varies linearly with strain rate and the curves are approximately parallel for different strains. Nonlinear variation is observed for the ZA model. In the ZA model, more strain rate hardening is observed for higher strain. This model could be closer to the real behavior because the material hardens at a faster rate at higher strains.

4.3 Simulation Procedure

In this work, FEA is used to simulate the LP process. ABAQUS [80] software is used to perform FEA. Figure 17 shows the two-dimensional representative mesh. It is an axi-symmetric model made up of finer and infinite elements. CAX4R (continuum axi-symmetric 4 noded reduced integration) elements are used for finer elements and CINAX4 (continuum infinite axi-symmetric 4 noded) elements are used for the infinite part. LP is a highly localized process.

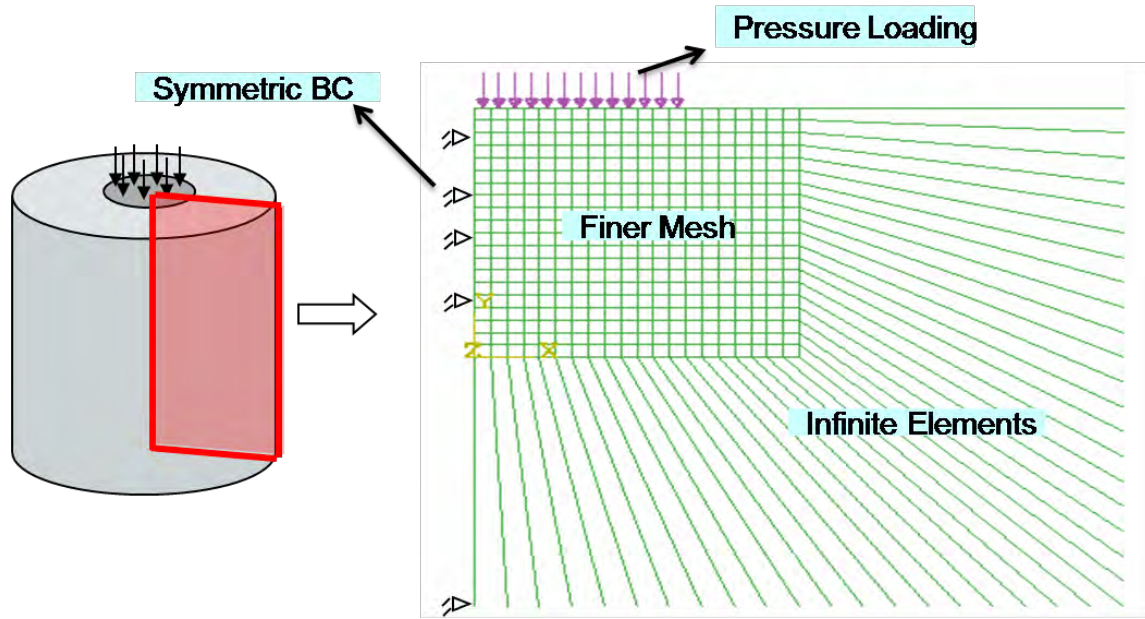


Figure 17: Representative Axi-symmetric FE Mesh

The size of the region treated with the shot is very small relative to the component size. Finer elements are modeled for the treated region and infinite elements represent the rest of the component. The dimension of the finer mesh region depends on the size of the laser spot. Researchers [37, 41] have used 2 times and 3.5 times the laser spot size for the finer mesh. In this work, the radius of the laser spot is 2.8mm, and the dimensions of the fine mesh region are 6mm \times 6mm, with symmetric boundary conditions as shown in Figure 17. The results with higher dimensions for finer mesh are very similar to the current mesh of 6mm \times 6mm. To achieve computational efficiency, the dimensions of 6 mm \times 6 mm were used. A refined mesh is required to accurately capture the shock wave imparted by the laser. A mesh size of 241 \times 241 nodes is used for finer elements after performing the convergence study. The element size is 0.025 mm \times 0.025 mm for the mesh size used for the finer mesh.

4.3.1 Pressure Loads

Pressure loading is applied on the top surface of the model as shown in Figure 17. The shock wave generated during the LP process is applied as a pressure pulse in FEA. There are different forms of pulse shapes used in the literature. The shape of the pressure pulse depends on the laser system. Ding and Ye [78] used a Gaussian shape and Braisted and Brockman [37] used a triangular shape. The pressure pulse applied in this work is shown in Figures 18 and 19 and is similar to the one used by Nam [38]. It has both time and spatial variation. A plot of peak pressure vs. power density was developed using quartz gages and this plot was used to estimate the average peak pressure profile. The pressure rises for the first few nanoseconds (ns) and gradually decreases after that.

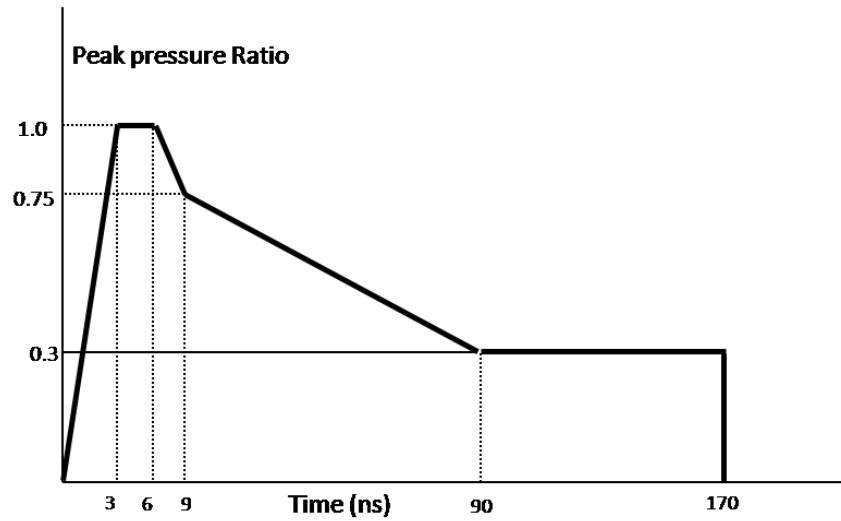


Figure 18: Temporal Pressure Profile of Shock Wave

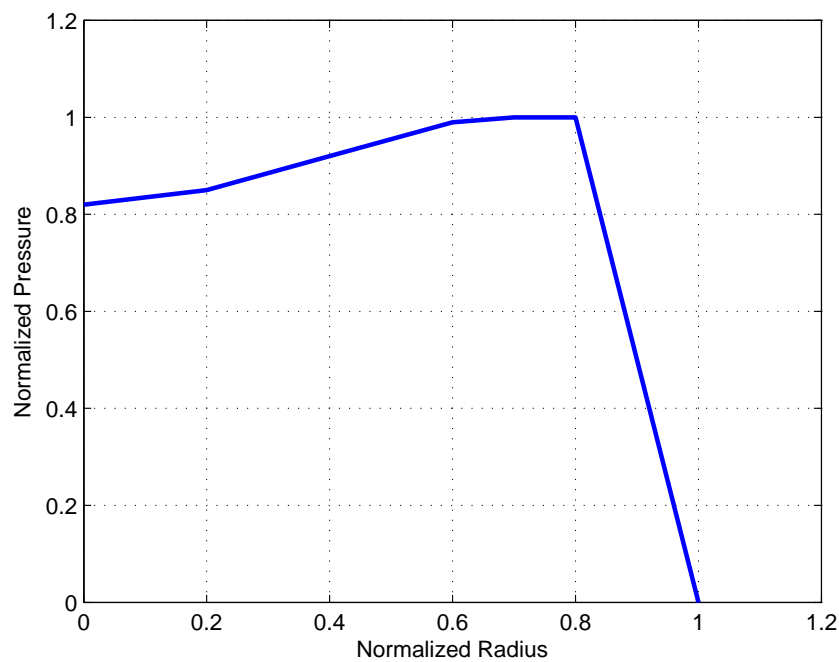


Figure 19: Spatial Pressure Profile of Shock Wave

4.3.2 Material Models

For all the FEA performed in this work, finer elements are assumed to be elastic–plastic in nature, while the infinite elements are assumed to be elastic only because the shock wave affects a small

portion of the component. These distinctions help to achieve efficient computation. As mentioned previously, the EPP, JC and ZA material models are investigated.

4.3.3 Analysis Procedure

The analysis can be categorized into two stages: dynamic loading analysis and static equilibrium analysis. During the first stage, the high speed, intense pressure transient loading is modeled until all plastic deformation has taken place. The second stage is the static equilibrium analysis that is performed to obtain the residual stress field. The data from the end of the dynamic analysis, such as nodal stresses, strains, and displacements are transferred to the equilibrium analysis using a restart file in ABAQUS. After the static equilibrium analysis is completed, there are two options: (i) one more LP shot or (ii) no further LP shots. If no further LP shots are required, residual stress data is obtained. If further LP shots are required, the residual stress data obtained from equilibrium analysis act as a starting point for the new LP shot. The procedure is shown schematically in Figure 20.

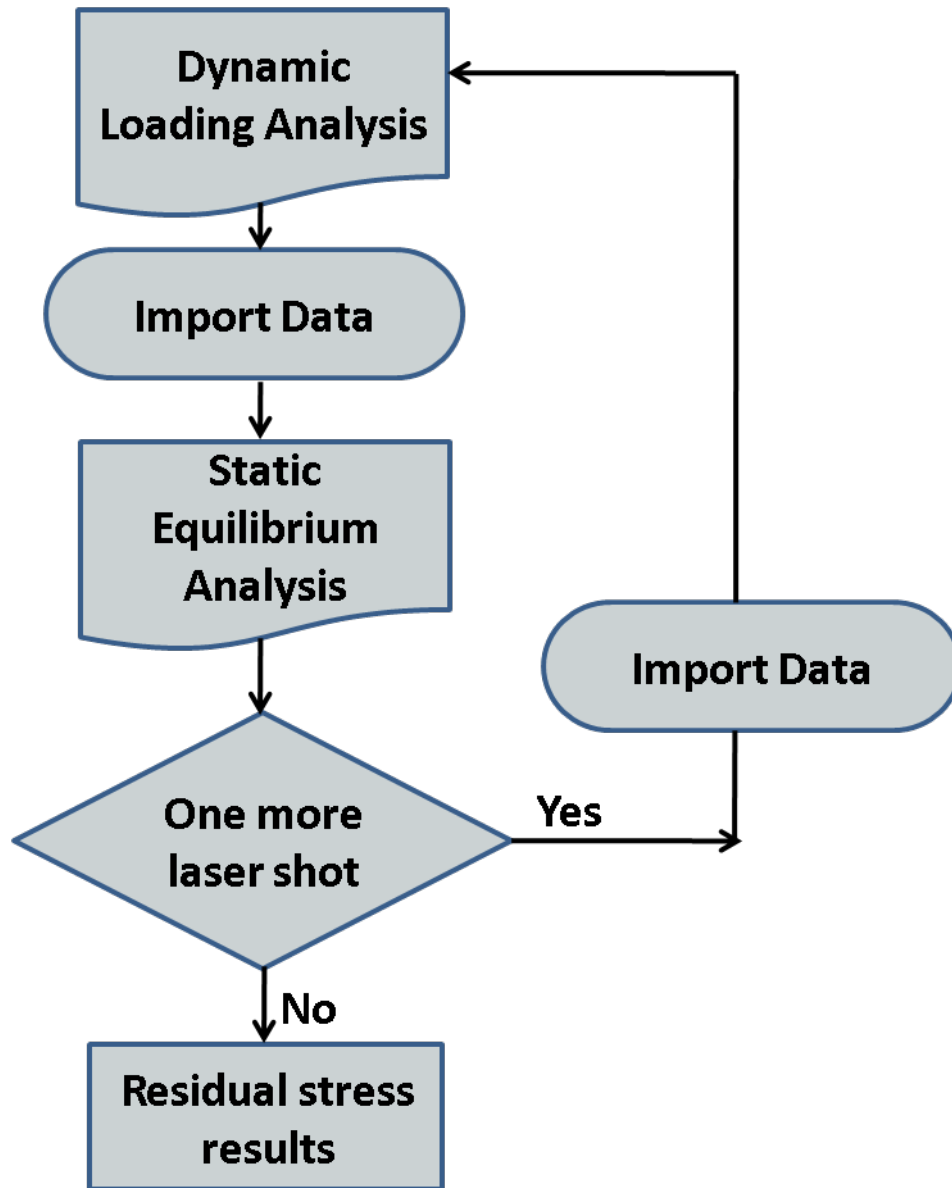


Figure 20: Schematic Representation of Analysis Procedure

4.3.3.1 Dynamic Loading Analysis

ABAQUS/Explicit is used for the loading part of the analysis. Two of the important parameters to be determined for the analysis are (i) time increment and (ii) final time to complete the analysis. Time increment (Δt) plays an important role in the convergence and accuracy of the analysis. If the time increment is greater than the critical limit (Δt_{crit}), it may lead to an unbounded solution [80]. There are different ways to estimate the critical limit [78]. A simple estimate is based on element length and wave speed of the material (C_d). The critical limit is calculated as $\Delta t_{crit} = \frac{L}{C_d}$, where L is the length of the smallest element and $C_d = \sqrt{E/\rho}$, where E and ρ are

Young's modulus and density, respectively. The time steps for each model are optimized from convergence studies. The loading analysis is performed until all the plastic deformation has taken place. This is shown in Figure 21, the history plot of kinetic energy. This plot indicates that the final time of 4000 ns is suitable for LP.

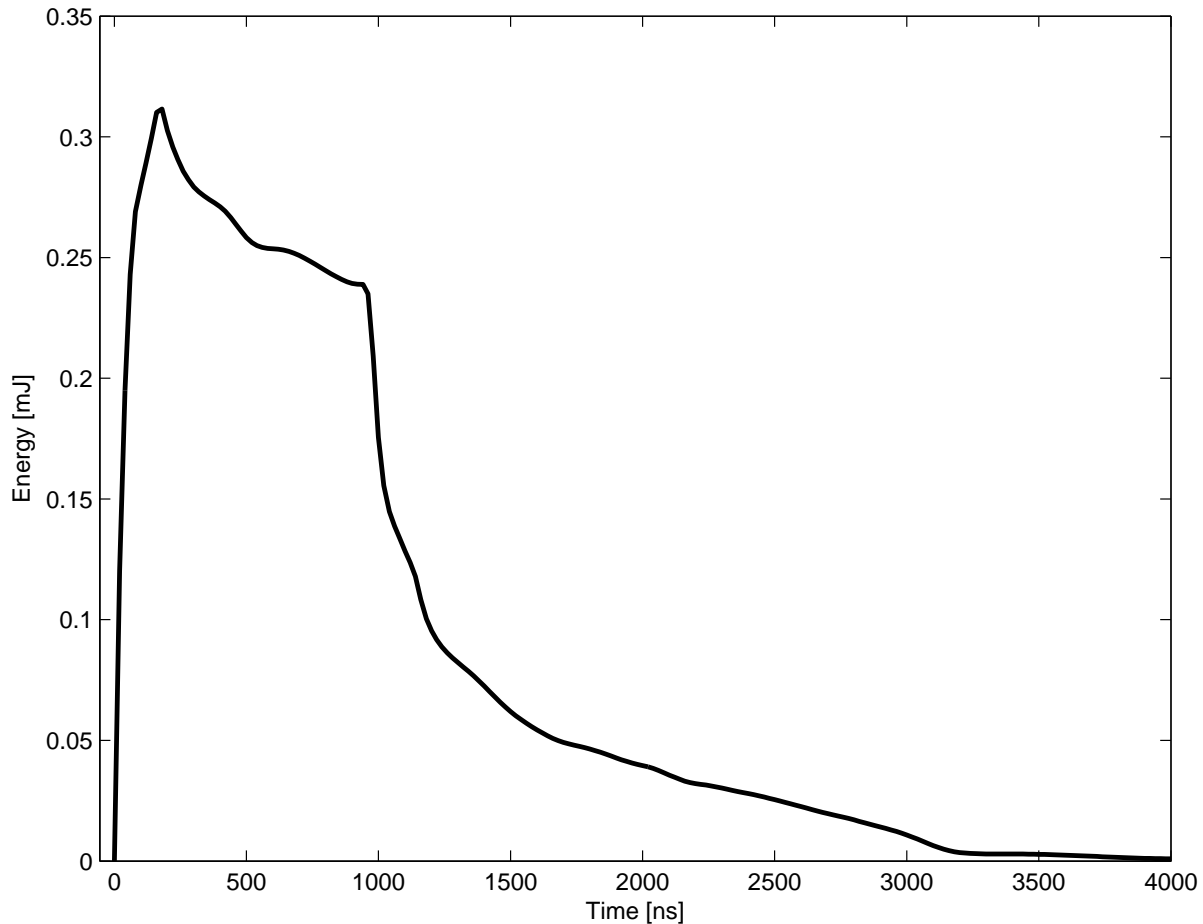


Figure 21: History of Kinetic Energy

4.3.3.2 Static Equilibrium Analysis

ABAQUS/Standard is used for the equilibrium analysis. The state of the deformed component from the end of dynamic loading analysis is transferred using a restart file to achieve static equilibrium. This step is used to calculate the residual stress profile.

4.3.3.3 Comparison between Explicit and Implicit Algorithms

ABAQUS/Explicit and ABAQUS/Standard are the two solvers used by ABAQUS in the FEA procedure. ABAQUS/Explicit uses an explicit algorithm and ABAQUS/Standard uses implicit algorithm for the numerical analysis. This section describes a brief comparison between the two

algorithms. Explicit and implicit are direct integration methods for solving the equation of motion (Equation 7)

$$[M] \{\ddot{D}\} + [C] \{\dot{D}\} + [K] \{D\} = \{R^{ext}\} \quad (7)$$

where $[M]$, $[C]$, and $[K]$ are mass, damping, and stiffness matrices respectively. $\{D\}$ is the displacement vector. $\{R^{ext}\}$ corresponds to external loads. These loads are in general a function of time. The direct integration methods are alternative to modal analysis methods [81]. In direct integration methods, displacement vector is associated with subscript n to denote the time step. The solution methodology for explicit algorithm have the form shown in Equation 8:

$$\{D\}_{n+1} = f(\{D\}_n, \{\dot{D}\}_n, \{\ddot{D}\}_n, \{D\}_{n-1}, \dots) \quad (8)$$

This displacement $\{D\}_{n+1}$ is determined in terms of completely historical information of displacements and its time derivatives. The displacement at the current step is a function f of displacements and their time derivatives of previous steps. Implicit methods have the form shown in Equation 9:

$$\{D\}_{n+1} = f(\{\dot{D}\}_{n+1}, \{\ddot{D}\}_{n+1}, \{D\}_n, \dots) \quad (9)$$

The computation of $\{D\}_{n+1}$ requires knowledge of the time derivatives of $\{D\}_{n+1}$. The implicit algorithm determines the solution with iterations, but the explicit algorithm determines the solution by advancing the kinematic state from the previous state. Central difference scheme is popularly used for the explicit algorithm. In comparison, the explicit algorithm is a clear choice for wave propagation analysis, especially for short duration. The implicit algorithm is better suited for long duration to achieve equilibrium.

4.4 Results and Discussion

Three peak pressures of 5.5, 6.1, and 8.3GPa are considered in this work. These three peak pressures are selected based on the availability of experimental data [38]. Three LP shots are used for a peak pressure of 6.1GPa, and one LP shot is used for the other two peak pressures. The in-depth experimental results of radial residual stresses at a distance of 1mm from the center for all three peak pressures are shown in Figures 22, 23, and 24 for the EPP model, the JC model, and the ZA model respectively.

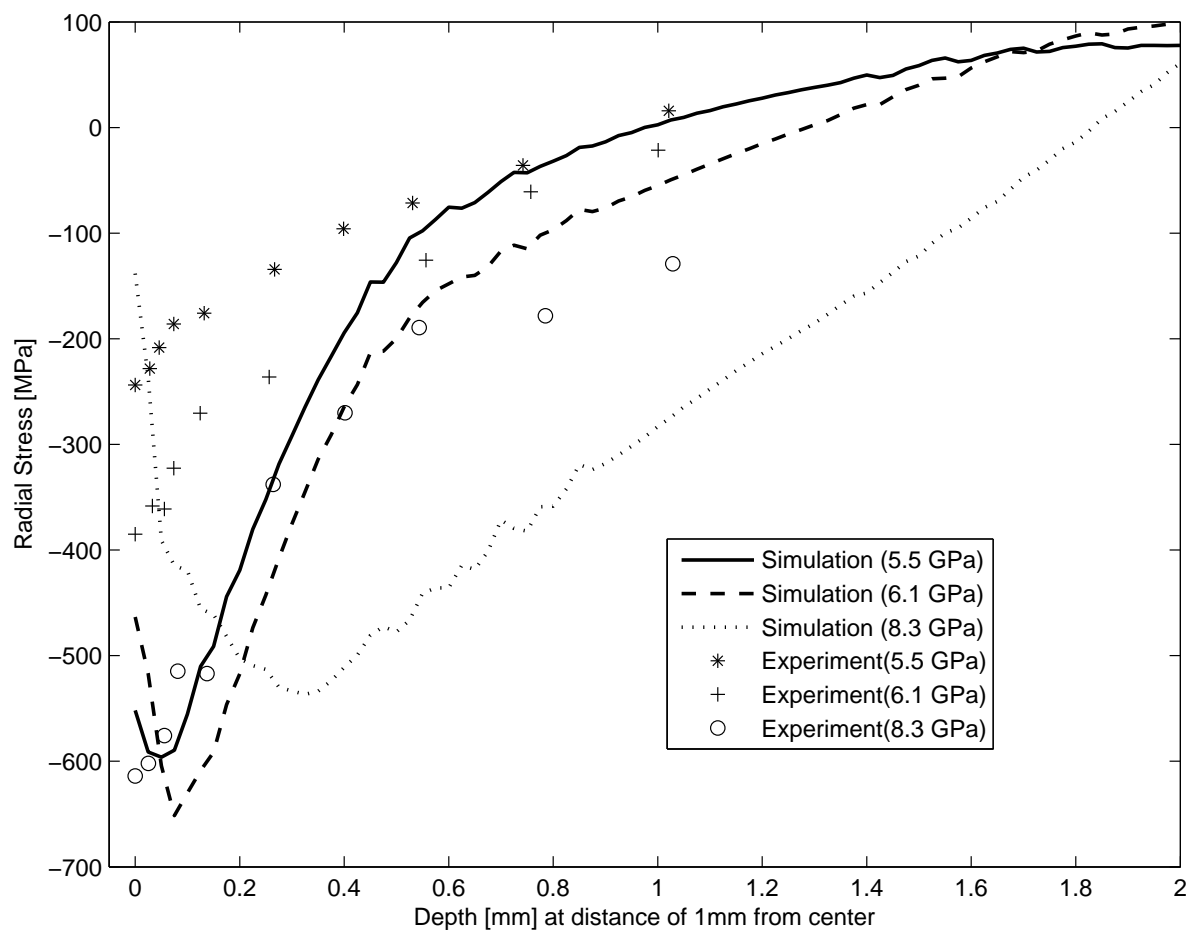


Figure 22: Residual Stress Comparison Between Simulation and Experiment for the EPP model

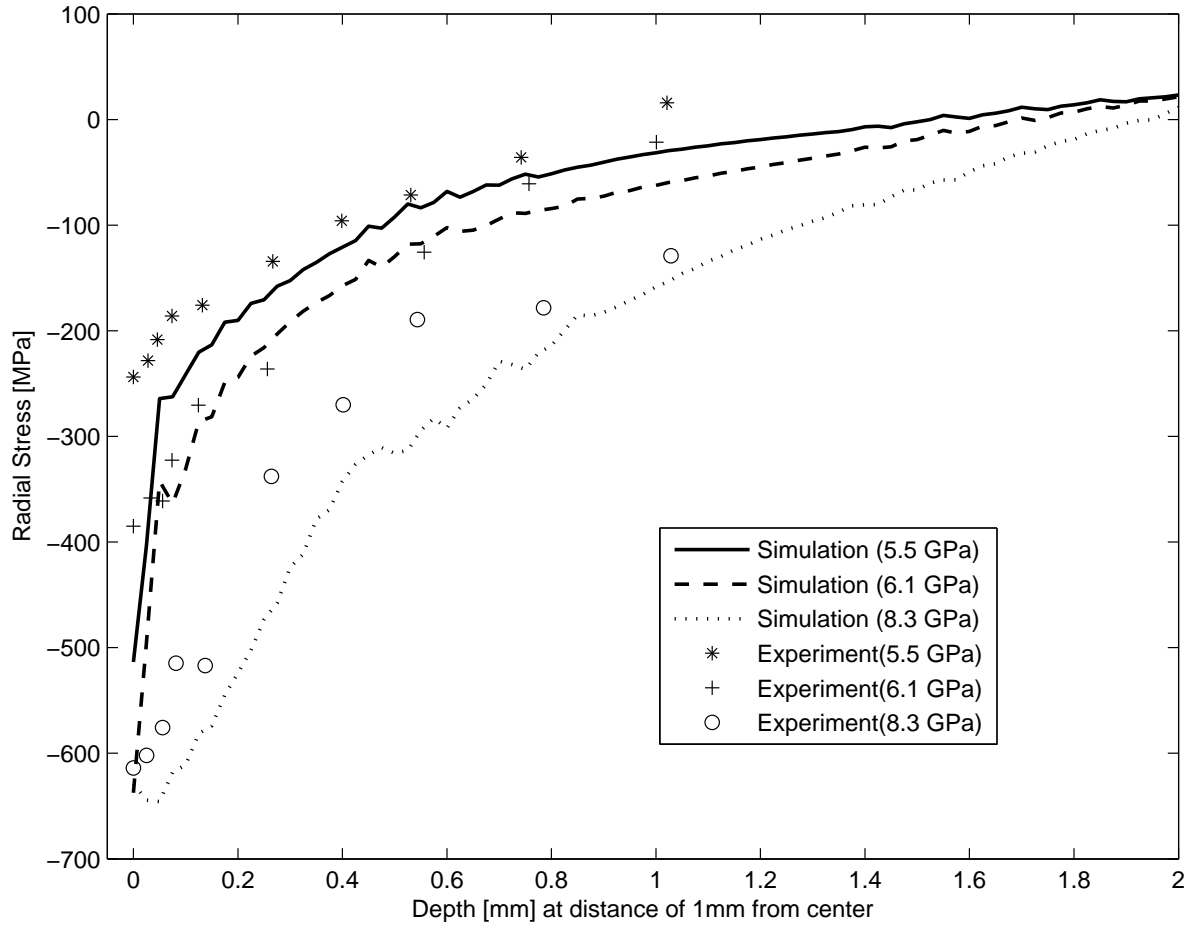


Figure 23: Residual Stress Comparison Between Simulation and Experiment for the JC model

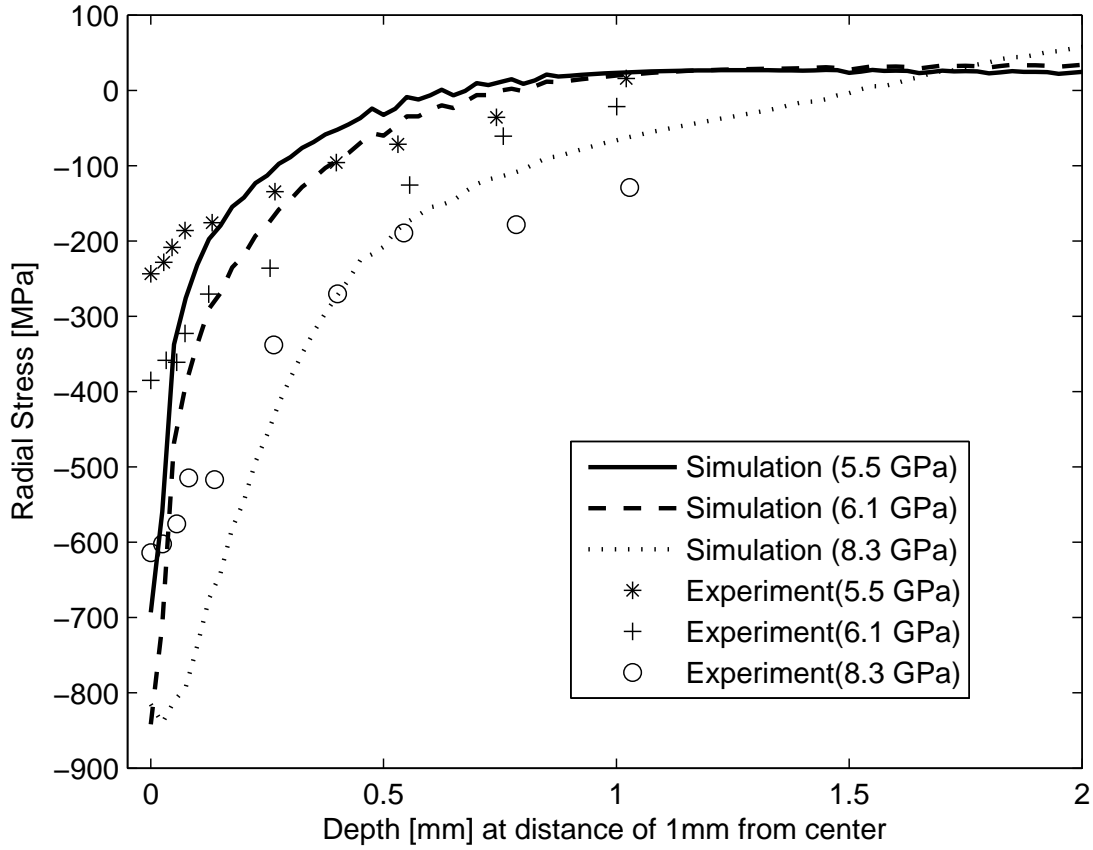


Figure 24: Residual Stress Comparison Between Simulation and Experiment for the ZA model

The x-ray diffraction technique was used to measure the residual stresses [38]. This is a destructive technique used to measure residual stresses along depth. First, the measurement is made on the surface. A thin layer is removed using electropolishing and the procedure is repeated for each depth measurement. This technique averages the residual stress over a square area. To compare the results of FEA and experiments, the same kind of averaging is performed for stresses resulting from FEA. A $1\text{mm} \times 1\text{mm}$ area is considered, and the x and y coordinates of the locations are converted into cylindrical coordinates as $r = \sqrt{x^2 + y^2}$ and $\theta = \tan^{-1} [y/x]$. The transformation of the stress components from cylindrical to rectangular is $\sigma_x = \sigma_r \cos^2 \theta + \sigma_\theta \sin^2 \theta - 2\tau_{r\theta} \sin \theta \cos \theta$. The shear component ($\tau_{r\theta}$) is zero (definition of axi-symmetric). The results comparison is discussed for each model separately.

4.4.1 EPP Model

Figure 25 shows the equivalent plastic strain variation versus depth for different peak pressures. The plastic strain data is obtained at a distance of 1mm from the center of the spot. The strains are higher on the surface and decrease with depth. The higher the magnitude of peak pressure, the

greater is the magnitude of plastic strain. This shows that the model is predicting the general trends with respect to strain.

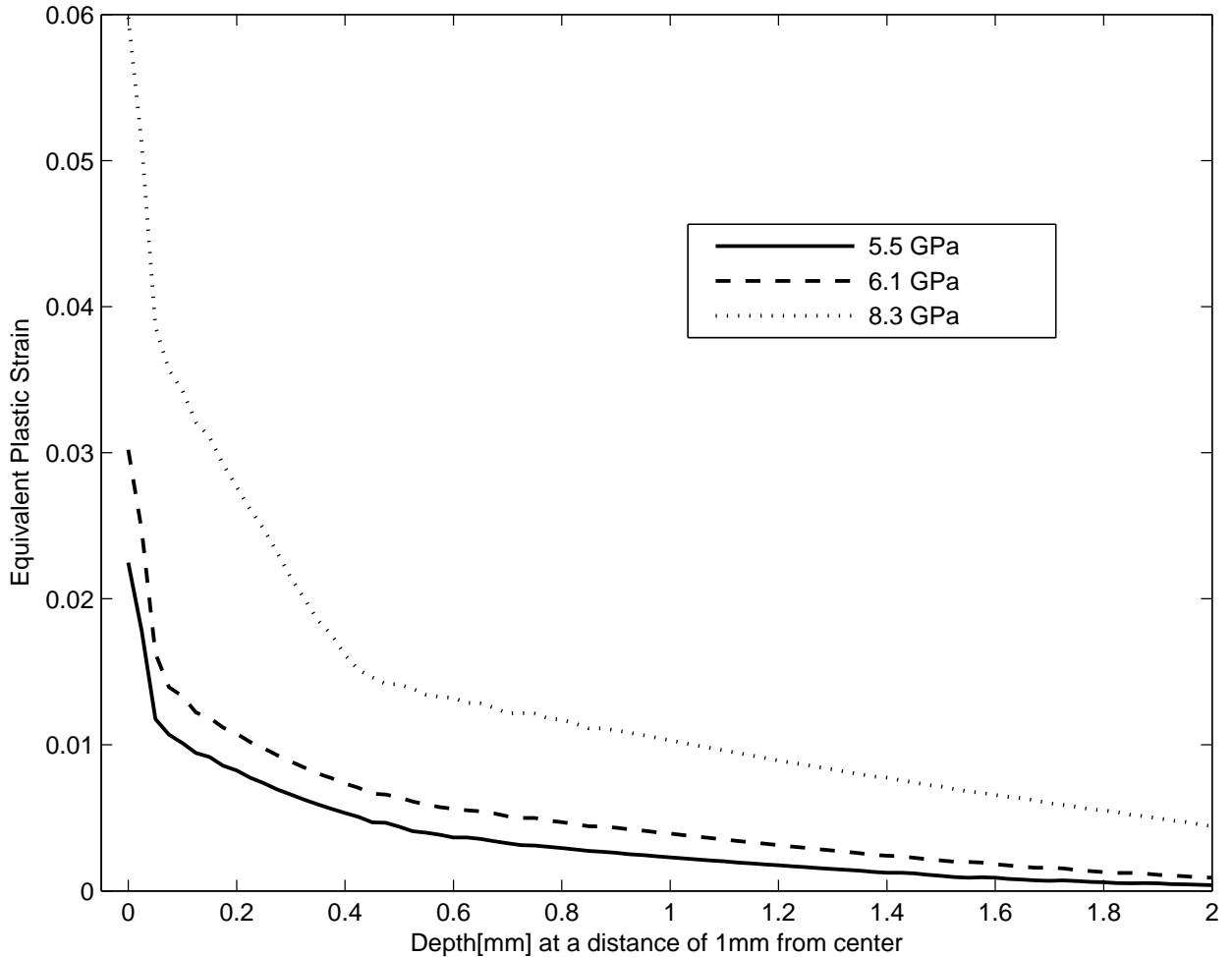


Figure 25: Equivalent Plastic Strain Variation with Depth for the EPP Model

Figure 22 shows the radial residual stress variation with depth, for different peak pressures. It includes both simulation and experimental results. A comparison between the simulation results for different peak pressures indicates that a higher magnitude of compressive residual stresses are generated for greater peak pressures only after a certain depth. For surface and near-surface regions, the model is not able to predict the experimentally observed trends. A higher magnitude of stress is obtained for lower peak pressure, and for all three peak pressures, there is a decrease in the magnitude of residual stress on the surface and near-surface region. The propagation of stress waves into the material for peak pressures of 5.5 GPa for the EPP model is shown in Figure 26 and for the 8.3 GPa is shown in Figure 27. Figures 28 and 29 show the stress wave propagation of peak pressures of 5.5 GPa and 8.3 GPa for the JC model respectively.

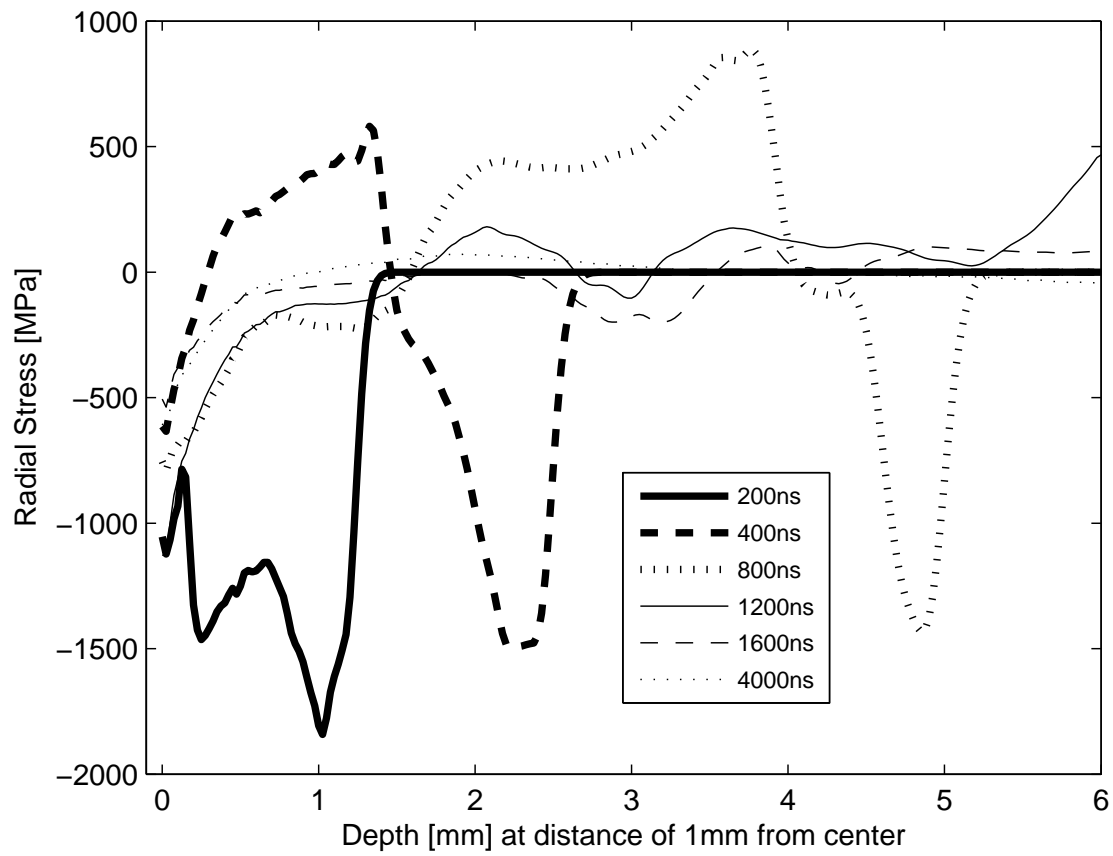


Figure 26: Propagation of Stress Waves for the EPP model at 5.5 GPa Peak Pressure

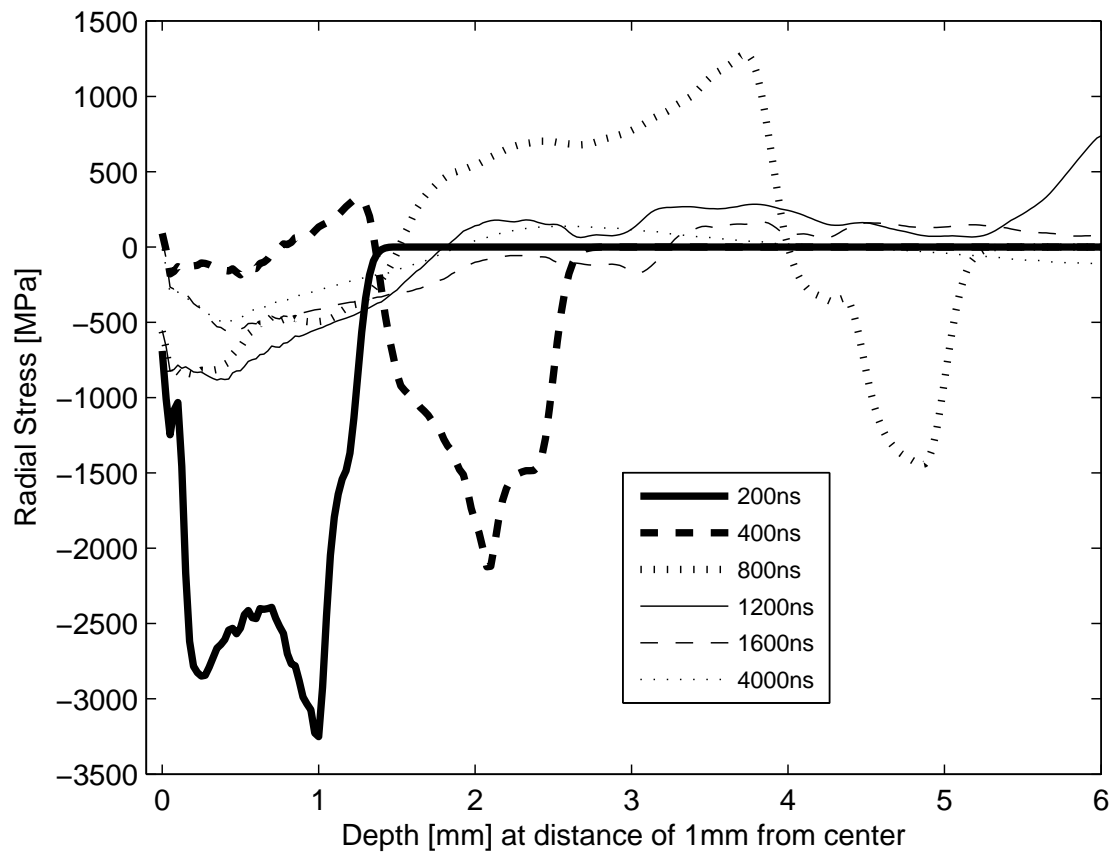


Figure 27: Propagation of Stress Waves for the EPP model at 8.3 GPa Peak Pressure

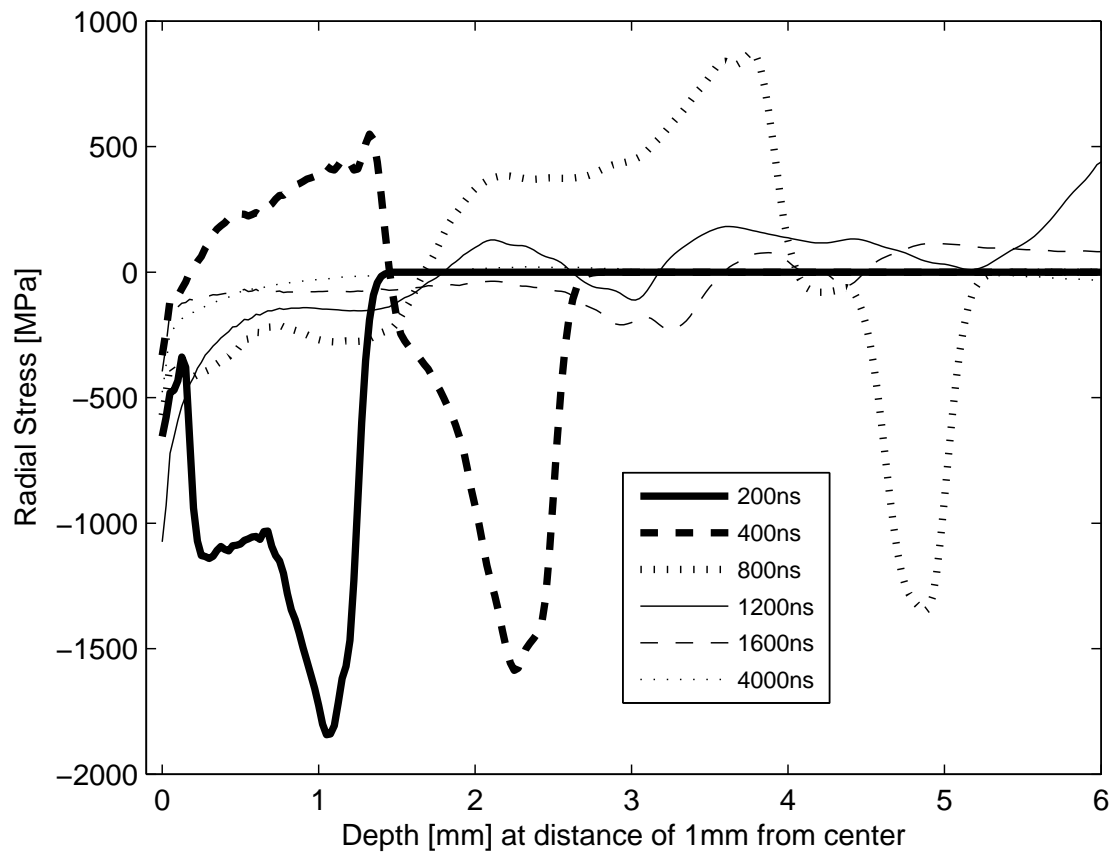


Figure 28: Propagation of Stress Waves for the JC Model at 5.5 GPa Peak Pressure

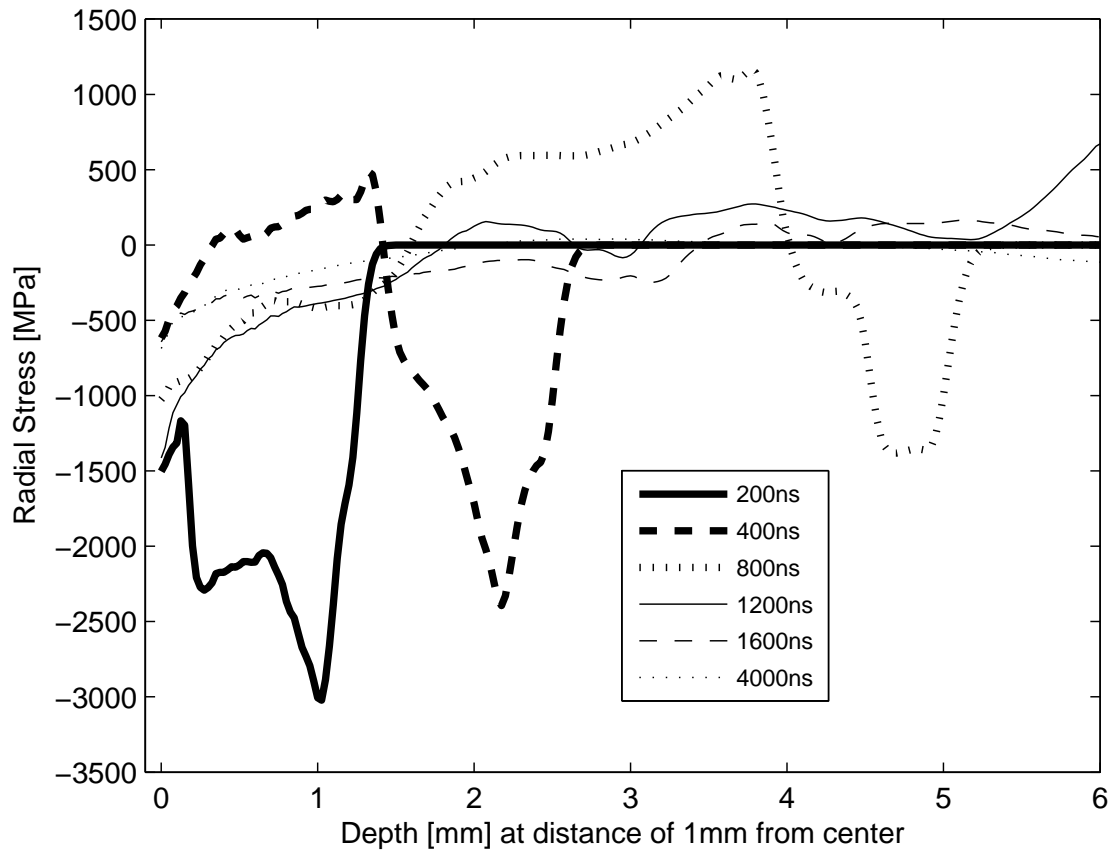


Figure 29: Propagation of Stress Waves for the JC model at 8.3 GPa Peak Pressure

During the first 200 ns the compressive wave declines steeply at the surface for both peak pressures for the EPP model. This decline is predominant for a peak pressure of 8.3GPa. There is no decline observed in the stress wave propagation for the JC model for either of the peak pressures. This initial stress wave has a significant effect on the residual stress, due to the magnitude of the wave. A comparison between the simulation and the experimental data for three peak pressures of 5.5, 6.1 and 8.3GPa can be seen in Figure 30.

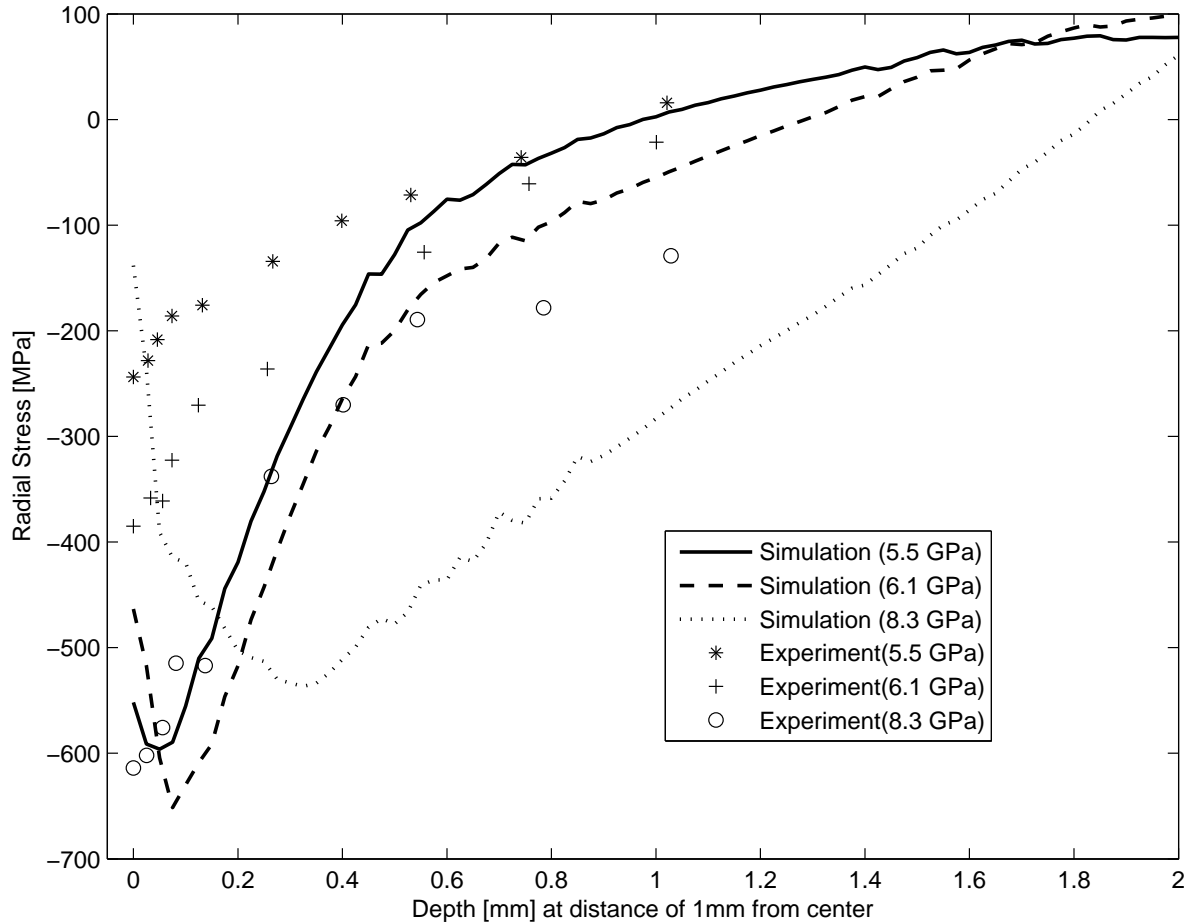


Figure 30: Residual Stress Comparison Between Simulation and Experiment for the EPP Model

For a peak pressure of 5.5GPa, the EPP model overestimates the residual stresses relative to the experimental data for the entire depth of 2mm. The EPP model overestimates the stresses after a certain depth for peak pressures of 6.1 and 8.3GPa. The EPP model is generally considered to be a conservative model for prediction of internal stresses. However, for residual stress determination, the EPP model always overestimates compared to experimental data since the EPP model does not take strain hardening into consideration. In the LP process, strain rate plays an important role, and the current EPP model does not consider strain rate dependence.

4.4.2 JC Model

Figure 31 shows the equivalent plastic strain variation with depth, for different peak pressures.

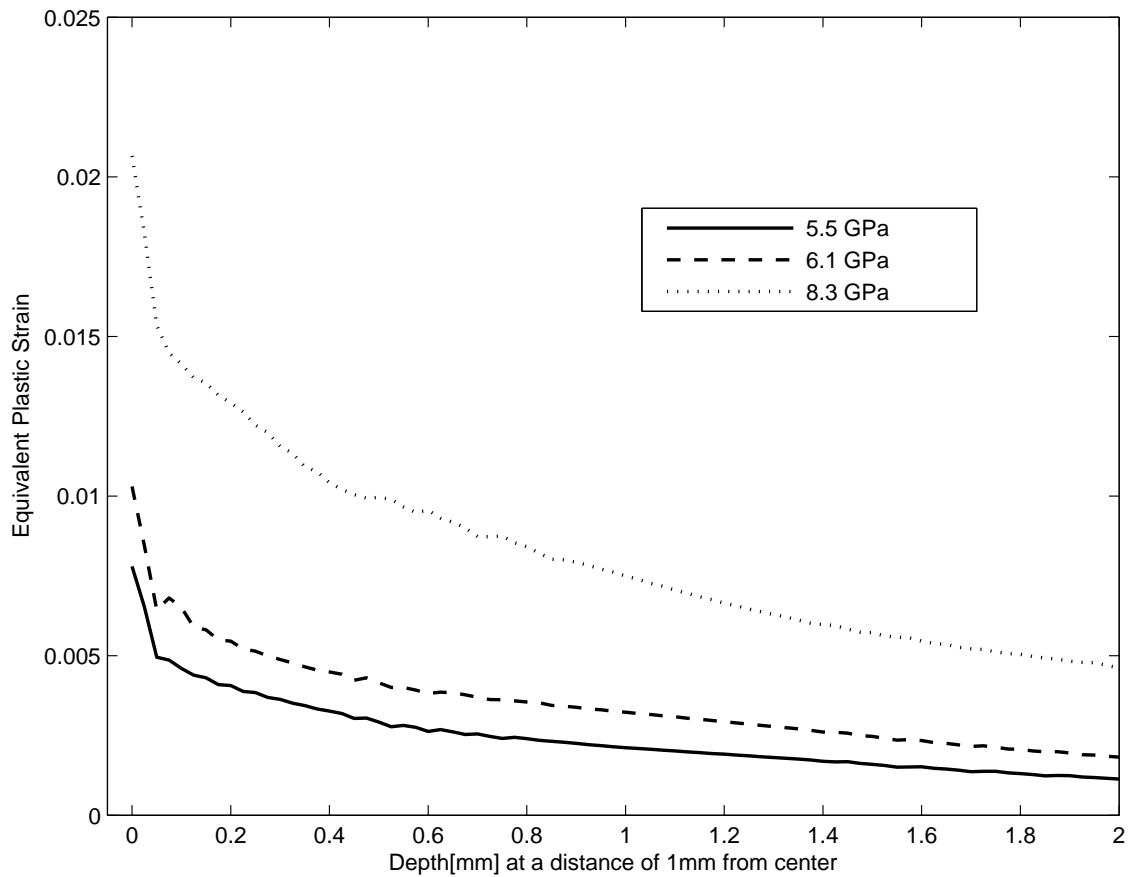


Figure 31: Equivalent Plastic Strain Variation with Depth for the JC Model

The same trends as observed in the EPP model can be seen here. There is a higher magnitude of plastic strain obtained for greater peak pressure. However, the magnitude of plastic strain is much lower than the EPP model for the three peak pressures. For the peak pressure of 8.3 GPa, a steep decrease in the strain can be seen up to a depth of 0.5mm, then a gradual decrease is observed. A comparison between radial residual stresses for three peak pressures is shown in Figure 32.

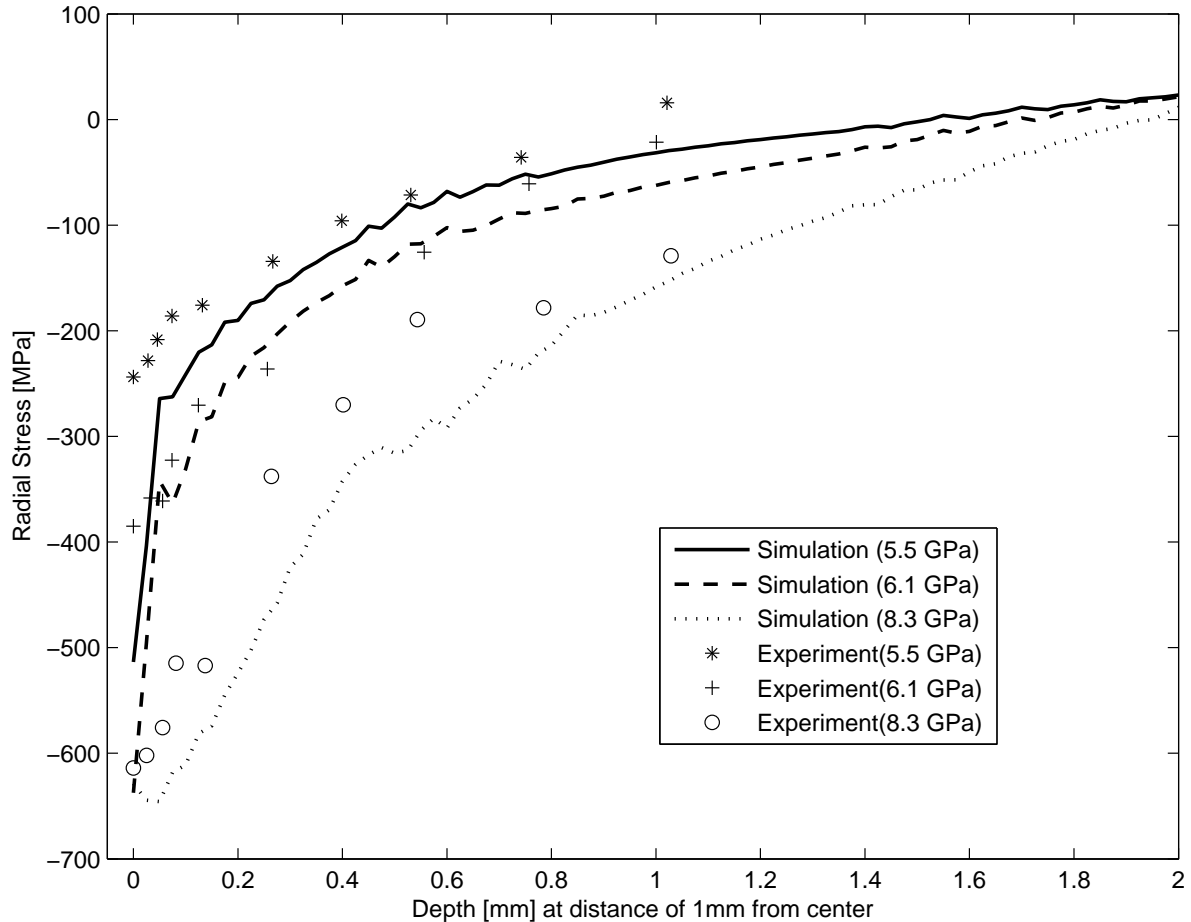


Figure 32: Residual Stress Comparison Between Simulation and Experiment for the JC Model

Figure 32 indicates that the JC model is able to predict the trends for the entire depth of 2 mm, unlike the EPP model. A higher magnitude of stress is obtained for greater peak pressure. The magnitudes of stress at the surface for peak pressures of 6.1 and 8.3 GPa are nearly equal. This can be attributed to the number of shots. For the peak pressure of 6.1 GPa, the number of shots is three, while for the peak pressure of 8.3 GPa, it is only one. A comparison between the simulation and the experimental data at all three peak pressures for the JC model can be seen in Figure 32. The JC model is in better agreement with experimental results for the three peak pressures, indicating the consistency of the model. However, the JC model overestimates the residual stress on the surface compared with the experimental data for peak pressures of 5.5 and 6.1 GPa. The JC model maintains the trend of overestimating the residual stress compared with experimental data for the three peak pressures (except from two data points for peak pressure of 6.1 GPa). In the next section, the results for the ZA model are discussed. Unlike the JC model, the ZA model overestimates on the surface and underestimates at higher depth.

4.4.3 ZA Model

Figure 33 shows the equivalent plastic strain variation with depth for the three peak pressures.

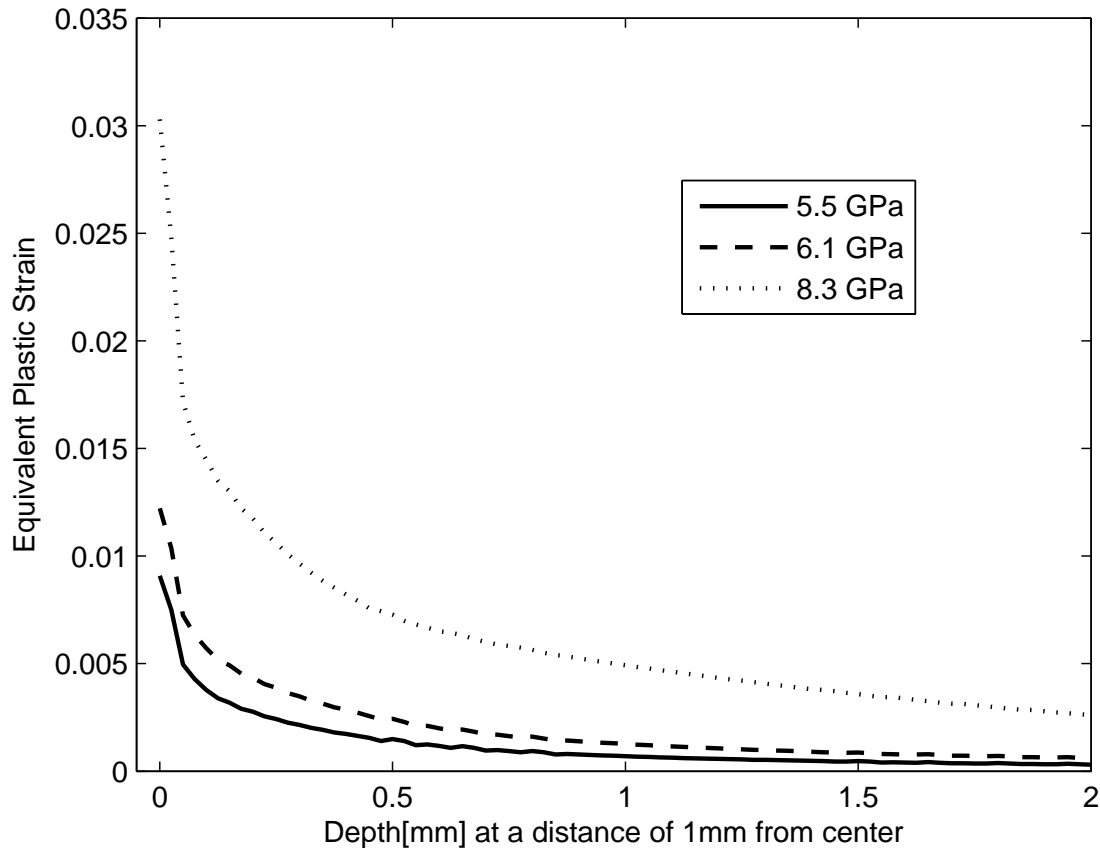


Figure 33: Equivalent Plastic Strain Variation with Depth for the ZA Model

The ZA model is able to predict the general trend of higher magnitude of plastic strain for greater peak pressure. The magnitude of strain predicted by the ZA model at the near-surface region is in between the predictions of the EPP and JC models. However, at higher depth, the ZA model has the lowest strain, followed by the EPP model, and the JC model as the highest magnitude of strain. There is also a steep decrease in strain at the near-surface region as seen in the other two models. The plastic strain curves at peak pressures of 5.5 and 6.1 GPa are relatively close to each other compared with the other two models. Radial residual stress variation with depth for different peak pressures is shown in Figure 34.

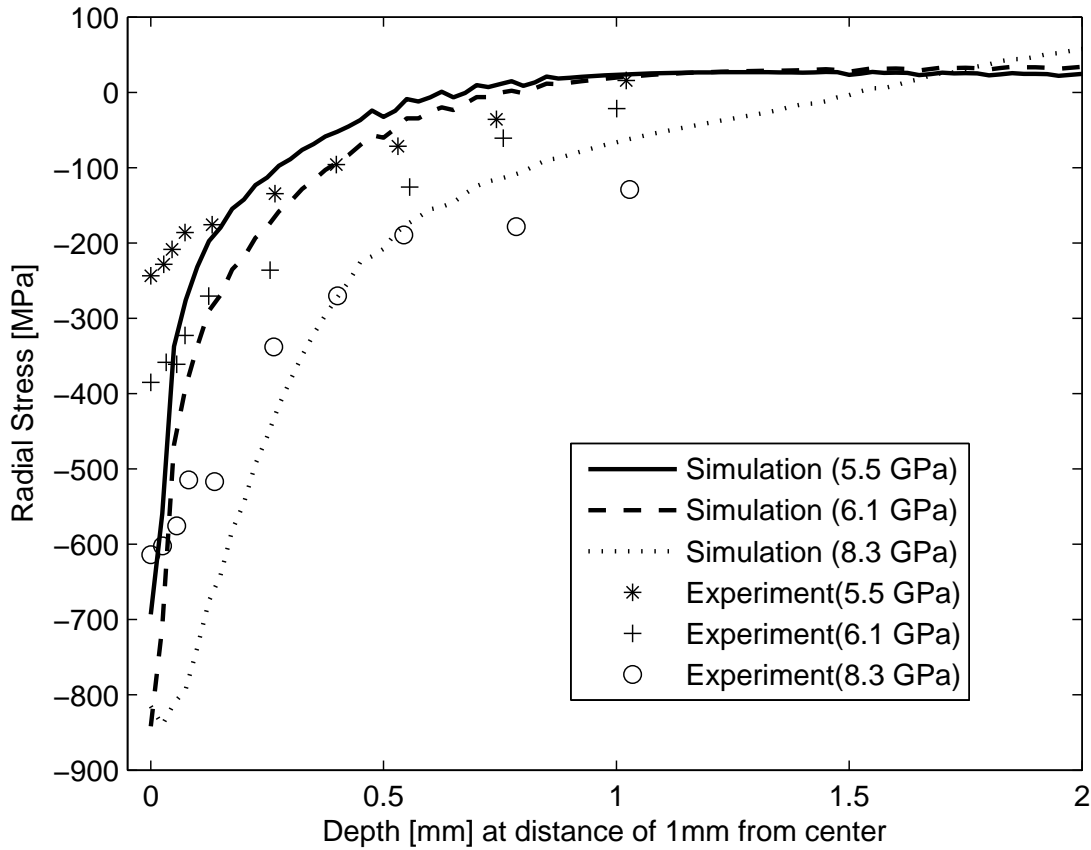


Figure 34: Residual Stress Comparison Between Simulation and Experiment for the ZA Model

The ZA model is also able to predict the trend for the entire depth. A higher magnitude of stress is obtained for greater peak pressures. The magnitude of stress at the surface for peak pressures of 6.1 and 8.3 GPa are nearly equal, as seen in the JC model. The magnitude of stress at the surface and near-surface regions is high compared to the JC model. A comparison between the simulation results and the experimental data shows that the ZA model overestimates the residual stress on the surface and near-surface regions for all three peak pressures. On the surface it overestimates not only with respect to the experimental data, but also with respect to the JC and EPP models. At higher depths, even though the ZA model underestimates relative to the experimental data, there seems to be a better agreement with experimental results of residual stress results on the surface.

4.4.4 Additional performance metrics

For further comparison between the models, four performance metrics are developed: (a) maximum compressive stress, (b) maximum tensile stress, (c) area of compressive stress and (d) depth of compressive stress. The area of compressive stress is a normalized area. It is calculated as the ratio of the number of nodes with compressive stress to the total number of nodes. The depth of the compressive stress is considered at a distance of 1mm from the center. A region with

a depth of 2 mm is considered, and a distance of 0.5mm from both ends is left out for the above mentioned metrics. Tables 4, 5, and 6 show the performance metrics for peak pressures of 5.5 GPa, 6.1 GPa, and 8.3 GPa respectively.

Table 4: Performance Metrics Comparison Between the Models for Peak Pressure of 5.5 GPa

| Performance Metrics | Peak Pressure of 5.5 GPa | | |
|---|--------------------------|---------|---------|
| | EPP | JC | ZA |
| Depth of Compressive Stress [mm] | 0.9959 | 1.4938 | 0.6473 |
| Area of Compressive Stress [normalized] | 0.5891 | 0.8624 | 0.5778 |
| Maximum Compressive Stress [MPa] | -669.84 | -600.60 | -778.38 |
| Maximum Tensile Stress [MPa] | 90.24 | 24.53 | 27.8 |

Table 5: Performance Metrics Comparison Between the Models for Peak Pressure of 6.1 GPa

| Performance Metrics | Peak Pressure of 6.1 GPa | | |
|---|--------------------------|---------|---------|
| | EPP | JC | ZA |
| Depth of Compressive Stress [mm] | 1.2448 | 1.668 | 0.7967 |
| Area of Compressive Stress [normalized] | 0.6528 | 0.9222 | 0.6113 |
| Maximum Compressive Stress [MPa] | -745.84 | -738.48 | -968.62 |
| Maximum Tensile Stress [MPa] | 112.40 | 23.23 | 37.53 |

Table 6: Performance Metrics Comparison Between the Models for Peak Pressure of 8.3 GPa

| Performance Metrics | Peak Pressure of 8.3 GPa | | |
|---|--------------------------|---------|---------|
| | EPP | JC | ZA |
| Depth of Compressive Stress [mm] | 1.8174 | 1.9917 | 1.4689 |
| Area of Compressive Stress [normalized] | 0.6528 | 0.9925 | 0.763 |
| Maximum Compressive Stress [MPa] | -642.20 | -778.12 | -963.21 |
| Maximum Tensile Stress [MPa] | 57.05 | 39.49 | 63.51 |

Compared to both the EPP and ZA models, the JC model predicts a higher depth of compression for all three peak pressures. The ZA model predicts the highest compressive stress for all three peak pressures, while the JC model predicts the lowest compressive stress for peak pressures of 5.5 and 6.1GPa. The JC model predicts the highest area of compressive stress for all three peak pressures, which shows consistency in the results.

4.5 Section Summary

Numerical simulation of the LP process is addressed in this chapter. FEA is shown to be a useful method to simulate the process. The strain rates involved in the LP process are on the order of $10^6 s^{-1}$, and experimental results of material behavior are typically not available at such high strain rates. Accurate material models help in providing a benchmark simulation. The nonlinear regression method is used to fit the experimental data to obtain the parameters for the corresponding models. The EPP model, which is most often used in the literature, is shown to produce inconsistent results. The ZA model, which is based on dislocation mechanics, produces consistent trends but overestimates the results compared to experimental data. The JC model is shown to produce consistent results matching the trends and better agreement with experimental results.

5.0 INVERSE OPTIMIZATION OF MATERIAL MODELS FOR SIMULATION OF LASER PEENED RESIDUAL STRESSES

The limitation of the existing simulation methodology is described in this chapter. This leads to the development of a new optimization-based approach for simulation of residual stresses induced by LP. Brief description of the experimental residual stress results is provided.

5.1 Limitation of Existing Simulation Methodology

The existing simulation methodology of residual stresses induced from LP is based on experimental data about the material behavior. Figure 35 shows a flow chart of the simulation process. The JC model is used as an illustration.

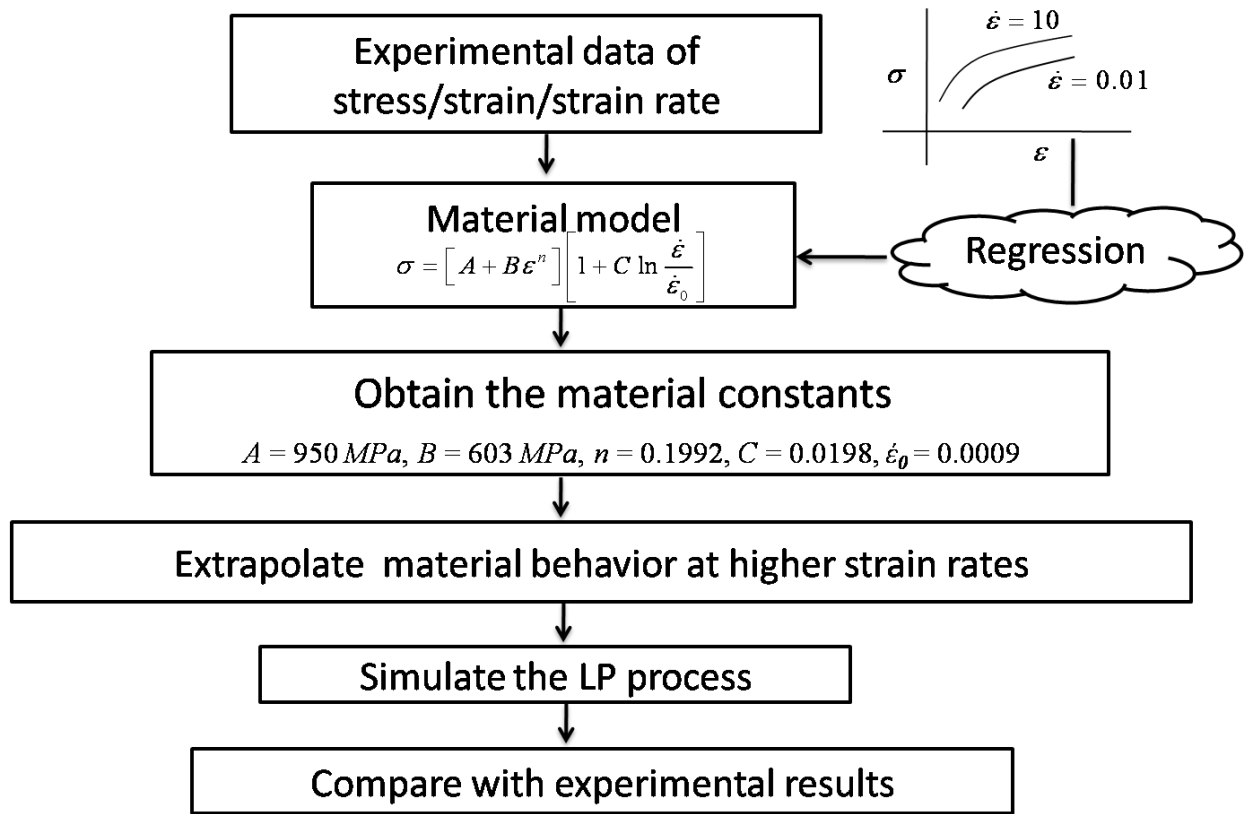


Figure 35: Traditional Approach for Simulation of Laser Peened Residual Stresses

Stress-Strain data at lower strain rates of a material is used to curve fit the material model under investigation. The material behavior is extrapolated at higher strain rates where no experimental data is available. Stress-strain data at different strain rates is typically not available for many materials. Inconel®718 is one such material. The limitation of the existing simulation methodology demands a new approach to simulate the residual stresses induced by LP.

5.2 Optimization-based Approach

The proposed optimization-based approach is shown in Figure 36.

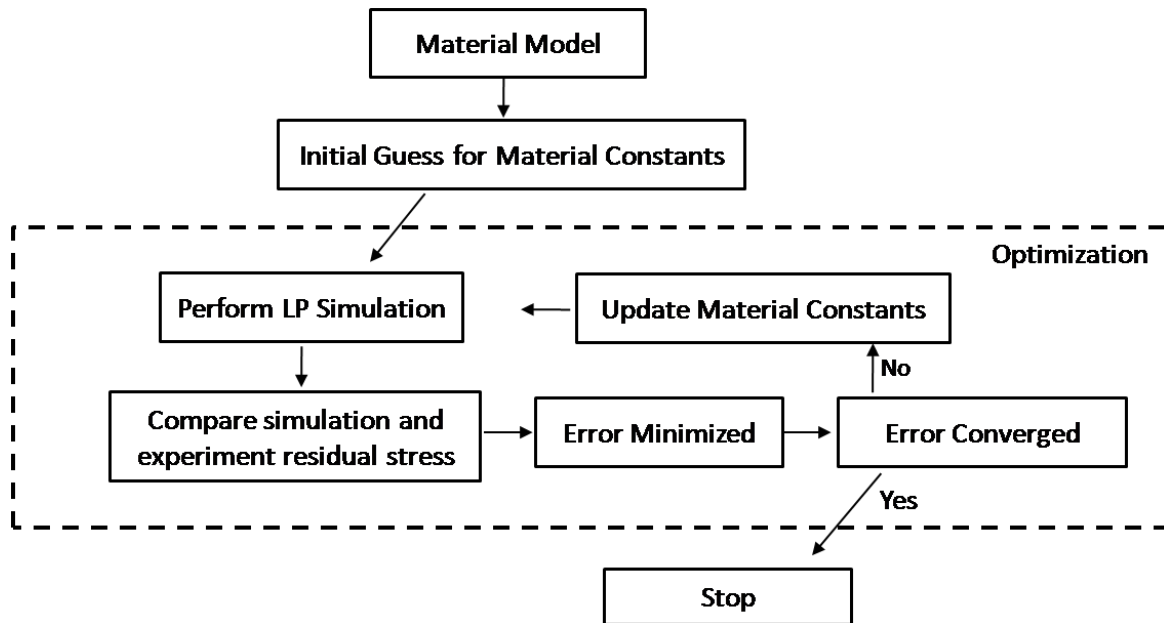


Figure 36: Optimization-Based Approach for Simulation of Laser Peened Residual Stresses

Material model constants are the design variables during the optimization procedure. An initial guess is provided for the material model constants. These initial values are obtained from the user experience or knowledge about the material. In this work, the initial guess for Inconel®718 is based on user experience and the initial guess for Ti-6Al-4V material is based on results from traditional approach. The drawback of the optimization-based approach is that the optimum model constants obtained are dependent on the initial guess. LP simulation is performed and the compressive residual stress is computed at locations for which the experimental data is available. The simulated compressive residual stress is compared with the experimental residual stress and the error between them is quantified. This error is considered as the objective function. An unconstrained optimization formulation is solved to obtain the optimum model constants as shown in Equation 10:

$$\text{Min Error} \quad (10)$$

$$\text{Lower Bounds} \leq \text{Model Constants} \leq \text{Upper Bounds} \quad (11)$$

The error is minimized and the model constants are iteratively solved until convergence. The convergence criterion to stop the iterations is that the difference between the objective function from the previous iteration should be less than a threshold value. The objective function used in this work is weighted least squares as shown in Equation 12:

$$e = w_1 \times \sqrt{\sum_{\text{Region I}} (RS_{exp} - RS_{sim})^2} + w_2 \times \sqrt{\sum_{\text{Region II}} (RS_{exp} - RS_{sim})^2} + w_3 \times \sqrt{\sum_{\text{Region III}} (RS_{exp} - RS_{sim})^2} \quad (12)$$

The experimental data is divided into three regions based on the location. w_1 , w_2 , and w_3 in Equation 12 act as weights for regions I, II, and III respectively. Details of each region are provided in the results section. The terms RS_{exp} and RS_{sim} are experimental residual stress and the residual stress predicted by the simulation respectively. In this work the regions are weighted equally, but the weights can be changed based on the agreement between simulation and experimental results. MATLAB's optimization toolbox [79], that uses a gradient-based approach, is used to perform optimization. Side bounds are placed considering the practicality of the model constants. The above-mentioned approach is performed for one set of LP conditions and optimum model constants are obtained. The same model constants are used for other operating conditions and the residual stress predictions are compared with the experimental data to demonstrate the consistency of the approach. The advantage of this approach is that the results obtained from the simulation will be consistent with the experimental results. The power of the approach can be seen when there is very little or no stress-strain data available at different strain rates. Using this inverse optimization approach, a material model can be employed to simulate the residual stresses induced by the LP process.

5.3 Material Model Details

Three material models are investigated for the validation of the optimization-based method. Two of the models are the JC and the ZA models that were previously used. Description of these two models are provided in the previous chapter. The Khan-Huang-Liang (KHL) [77] model is the third material model under investigation. The JC and KHL models are considered phenomenological models, while the ZA model is a physics-based model.

5.3.1 KHL Model

The KHL model is based on the JC model. The flow stress equation is shown in Equation 13

$$\sigma = \left[A + B \left(1 - \frac{\ln \dot{\epsilon}}{\ln D_0^p} \right)^{n_1} \right] \left[\frac{\dot{\epsilon}}{\dot{\epsilon}^*} \right]^C \quad (13)$$

A major feature of this model, compared to the JC model, is that it can accommodate decreasing work-hardening with an increasing strain rate through the constant n_1 . ϵ and $\dot{\epsilon}$ are the plastic

strain and strain rate, respectively. Model constants A and B are similar to the constants in the JC model. A represents initial yield strength at room temperature. B and n represent strain sensitive parameters. D_0^p is an arbitrarily chosen upper bound on the strain rate. In this work, D_0^p is assumed to be 10^8 . $\dot{\epsilon}^*$ is the reference strain rate at which the model constants are determined. In most cases, $\dot{\epsilon}^*$ is assumed to be equal to $1s^{-1}$.

5.4 Simulation Procedure

The simulation procedure described in the previous chapter is used. The addition of KHL model is implemented and the material properties [82] for Inconel®718 are shown in Table 7.

Table 7: Material Properties for Inconel®718

| Property | Value |
|-----------------------|---------|
| Young's Modulus (GPa) | 199.95 |
| Poisson's Ratio | 0.29 |
| Density(kgm^{-3}) | 8193.25 |

5.5 Results and Discussion

For Inconel®718, the residual stress predictions through depth are compared with experimental data at the center of the laser spot, while the comparison is performed at a distance of 1mm from the center of the spot for Ti-6Al-4V. The averaging procedure described in the previous chapter is implemented. For Ti-6Al-4V material, residual stress results using the traditional approach are available [83]. A comparison is made between two approaches to demonstrate the consistency of the optimization-based approach. The residual stress results for Inconel®718 material are presented first, followed by Ti-6Al-4V material.

5.5.1 Validation of Optimization-Based Approach for Inconel®718

Inconel®718 is a nickel-based super alloy used in several gas turbine components that operate at high temperatures such as $1000^{\circ}C$. The experimental procedure to perform LP experiments is discussed followed by comparison with simulation predictions.

5.5.1.1 LP Experimental Procedure

LP experiments were performed at LSP Technologies, Dublin, OH. Four coupons were laser peened to provide experimental residual stress profiles to compare with the simulation results. The coupons were 25 mm \times 25 mm square with a thickness of 12.7 mm. They were laser peened with one laser spot with a diameter of 5.6 mm in the center of one face. The surface to be laser peened was electropolished to remove machining stresses before LP. The LP was performed with an Nd-glass laser using black paint as the opaque overlay and water as the transparent overlay. The LP conditions are shown in Table 8.

Table 8: LP Conditions Used for Inconel®718

| Energy Density [J/cm^2] | Laser Pulse Length [ns] | Power Density [GW/cm^2] |
|-----------------------------|-------------------------|-----------------------------|
| 105 | 25 | 4.2 |
| 132 | 21 | 6.3 |
| 181 | 28 | 7.2 |
| 146 | 18 | 8.1 |

X-ray diffraction method was used for the measurement of residual stress profiles from the laser peened surface. With this technique, the measurements were made using a 2 mm square x-ray diffraction spot on the coupon surface, centered within the laser spot. After taking a surface measurement, the material was incrementally removed from surface by electropolishing and another measurement was taken on the exposed surface. This was done for each depth in the residual stress profile. The x-ray diffraction result provides a measurement of the elastic strain. The elastic modulus is then used to derive the residual stress at each depth. Corrections are applied to account for the x-ray penetration depth and the stress relaxation accompanying the removal of material from the surface. The residual stress data at different depths and peak pressures shown in Table 9 are measured at LSP Technologies Inc, provided Dr. Alan H. Clauer.

5.5.1.2 Residual Stress Comparison Between Simulations and Experiments

The regions are divided based on the location of the experimental data. Region I is considered up to a depth of 0.5 mm from the surface, Region II is from 0.5 mm to 1.5 mm and Region III is from 1.5 mm onwards. The optimization-based approach is adapted to the JC model and the KHL model. A peak pressure of 6.6 GPa is arbitrarily chosen to perform the optimization. The constants obtained for the JC model are shown in Table 10. The model constants obtained for the KHL model are shown in Table 16. The same model constants are used for other peak pressures of 5.3, 7.1, and 7.6 GPa to demonstrate the consistency of the inverse optimization approach. Figures 37, 38, 39, and 40 show the residual stress comparison between simulations and experimental results for peak pressures of 5.3, 6.6, 7.1, and 7.6 GPa respectively.

Table 9: In-Depth Residual Stresses for Inconel®718 [Courtesy: LSP Technologies, Inc.]

| 5.3 GPa Peak Pressure | | 6.6 GPa Peak Pressure | | 7.1 GPa Peak Pressure | | 7.6 GPa Peak Pressure | |
|-----------------------|--------------|-----------------------|--------------|-----------------------|--------------|-----------------------|--------------|
| Depth [mm] | Stress [MPa] | Depth [mm] | Stress [MPa] | Depth [mm] | Stress [MPa] | Depth [mm] | Stress [MPa] |
| 0.000 | -955 | 0.000 | -843 | 0.000 | -734 | 0.000 | -959 |
| 0.025 | -926 | 0.028 | -997 | 0.028 | -1001 | 0.028 | -770 |
| 0.051 | -847 | 0.053 | -906 | 0.053 | -852 | 0.056 | -1006 |
| 0.135 | -474 | 0.132 | -670 | 0.127 | -599 | 0.135 | -647 |
| 0.254 | -265 | 0.254 | -369 | 0.262 | -584 | 0.272 | -481 |
| 0.511 | -32 | 0.516 | -227 | 0.541 | -318 | 0.513 | -544 |
| 1.011 | -110 | 1.054 | -64 | 1.039 | -286 | 1.034 | -163 |
| 1.542 | -61 | 1.547 | -27 | 1.562 | -147 | 1.585 | -191 |
| 2.098 | -1 | 2.055 | -23 | 2.070 | 10 | 2.106 | -134 |

Table 10: Model Constants Using Optimization-Based Approach for the JC Model for Inconel®718

| Parameter | Value |
|--------------------|-------------------------|
| A | 506.44MPa |
| B | 1578.86MPa |
| n | 7.94×10^{-4} |
| C | 2.03×10^{-3} |
| $\dot{\epsilon}_0$ | $6.45 \times 10^{-4}/s$ |

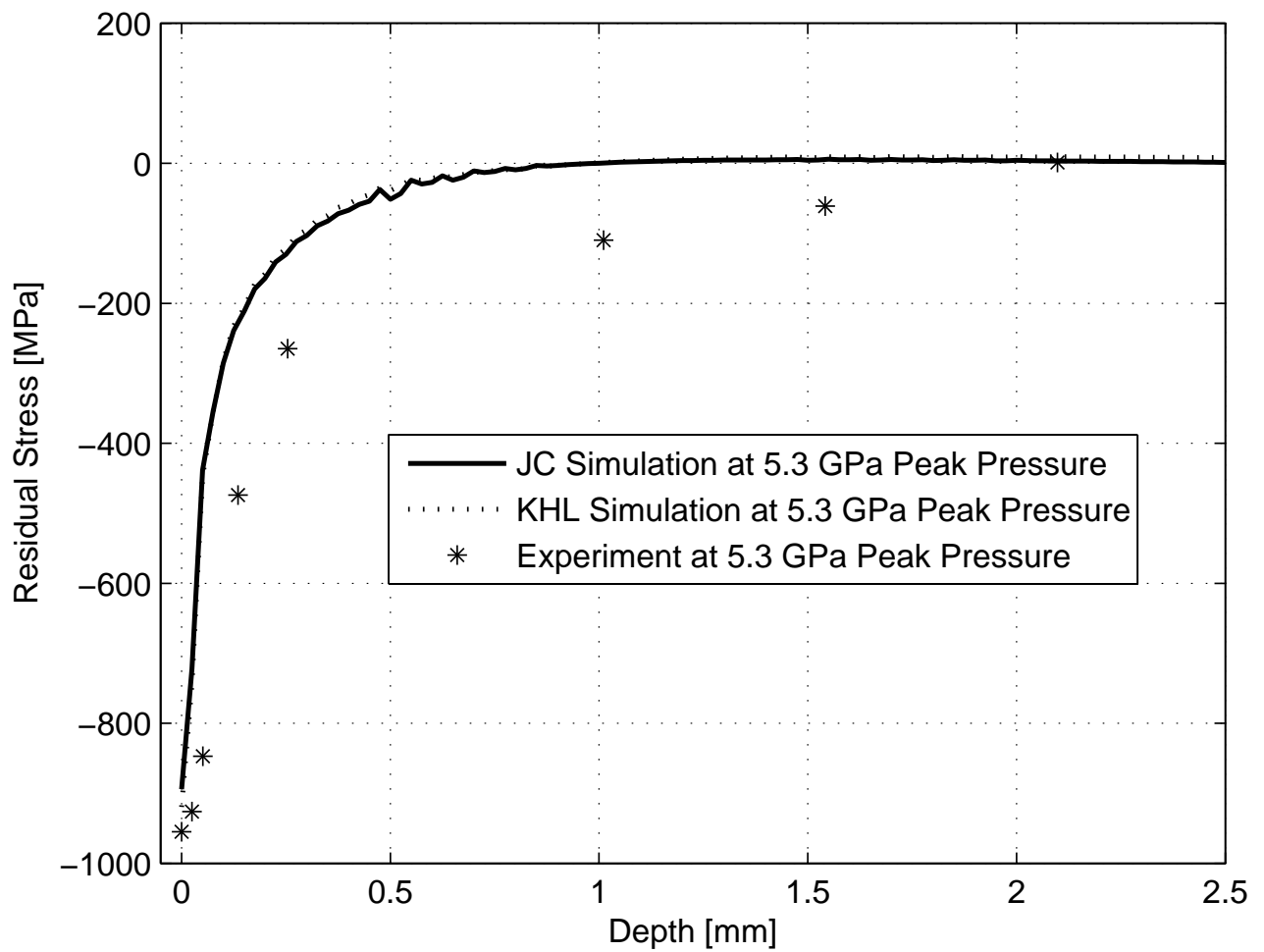


Figure 37: Residual Stress Comparison for Inconel®718 with 5.3 GPa Peak Pressure

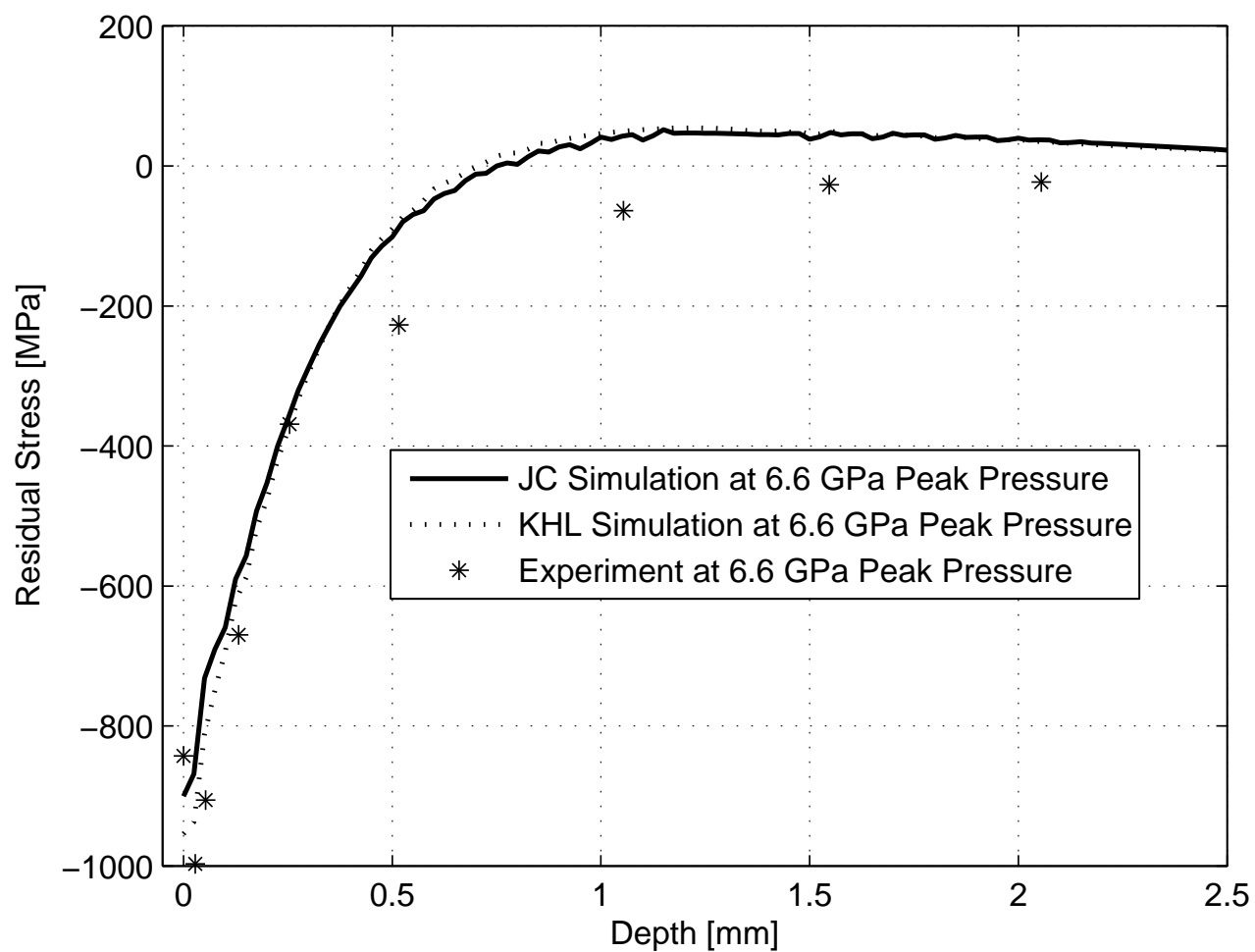


Figure 38: Residual Stress Comparison for Inconel®718 with 6.6 GPa Peak Pressure

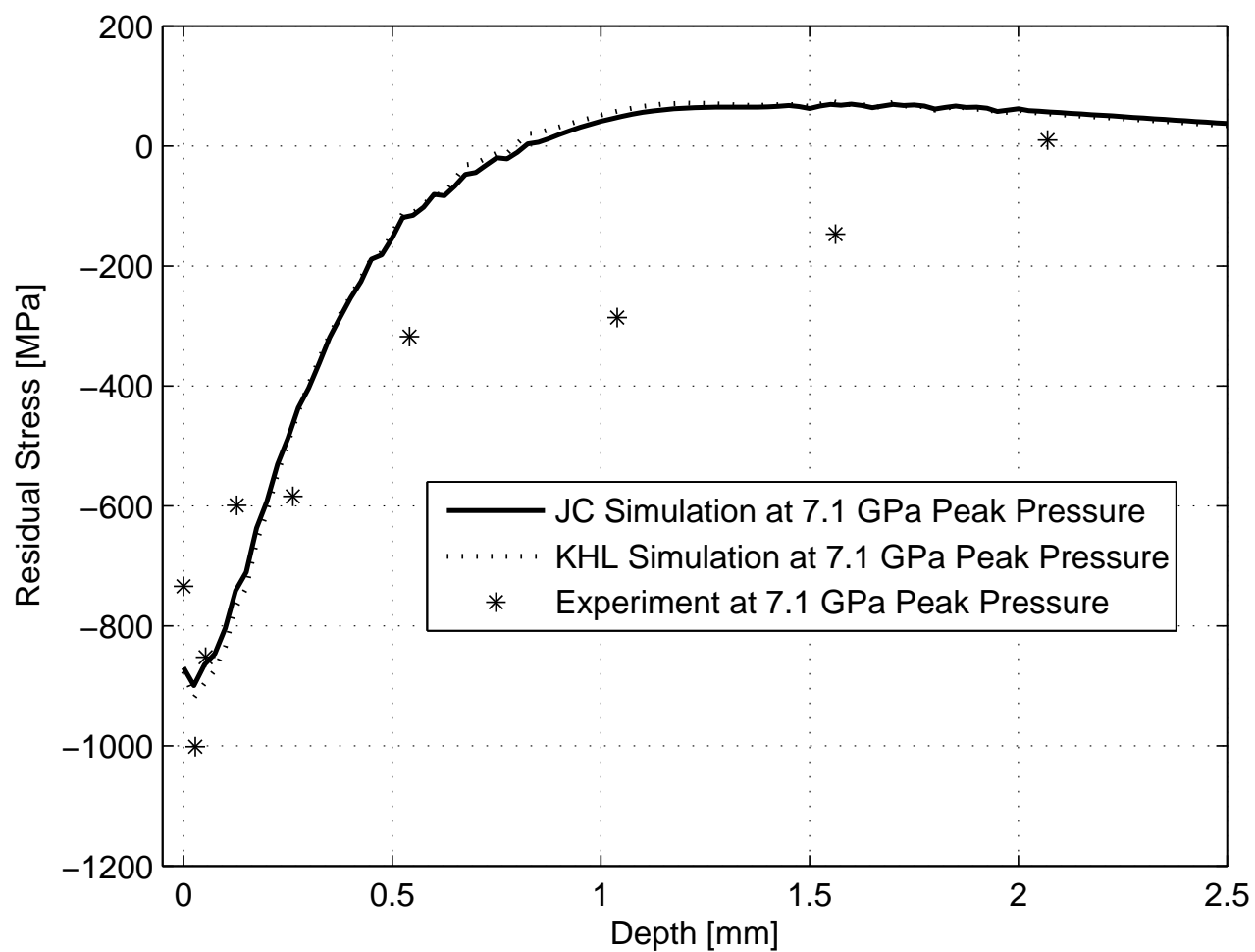


Figure 39: Residual Stress Comparison for Inconel®718 with 7.1 GPa Peak Pressure

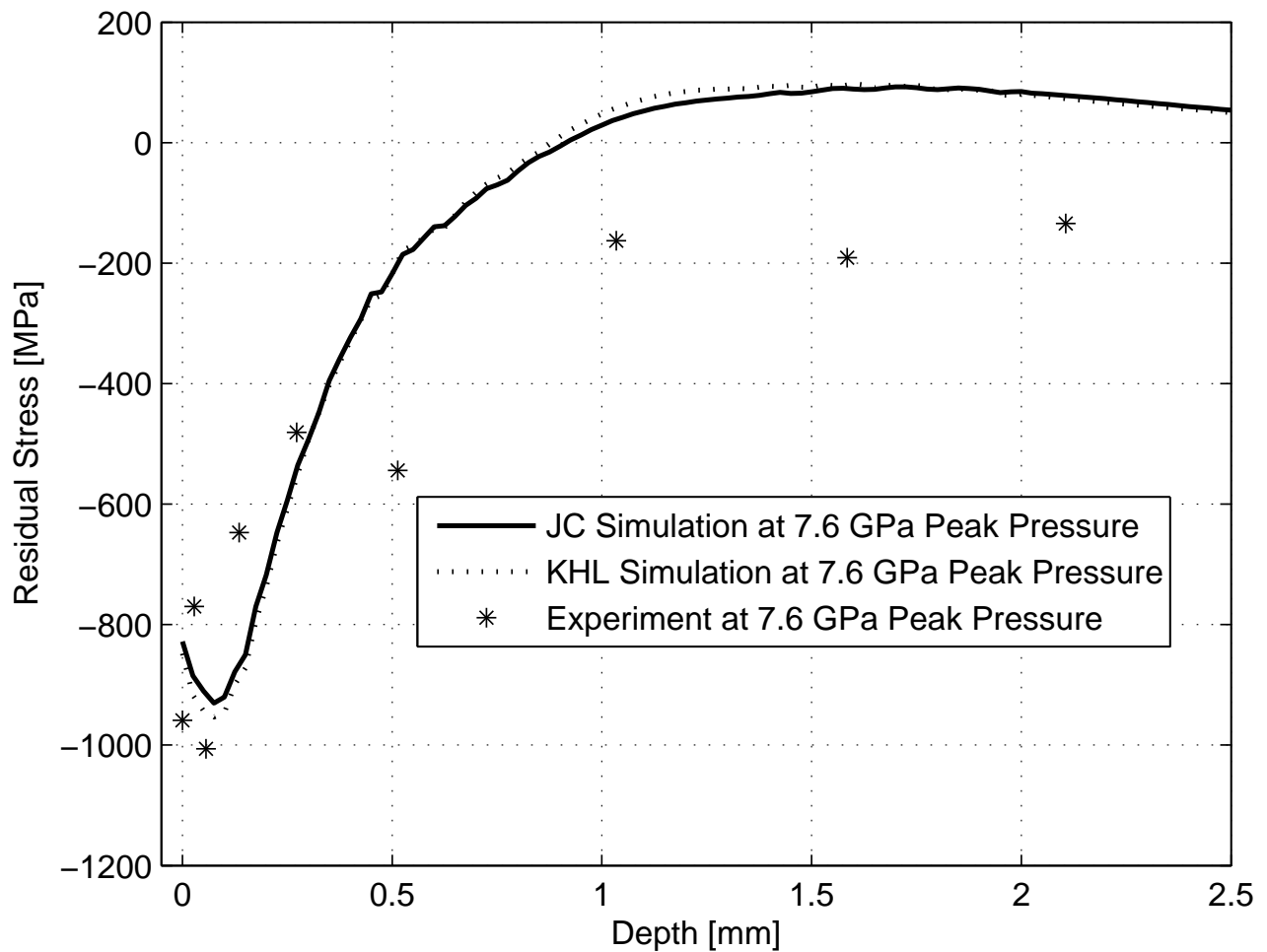


Figure 40: Residual Stress Comparison for Inconel®718 with 7.6 GPa Peak Pressure

Simulation results follow the trends of the experimental results for all peak pressures in both the JC and the KHL models. The results predicted by the JC model and the KHL model are similar to each other. The reason for this could be attributed to the fact that the KHL model is based on the JC model. The simulation results show a consistent trend of underestimating the experimental results for all peak pressures. For peak pressures of 5.3 and 6.6 GPa, the simulation prediction performs consistently for the entire depth. For peak pressures of 7.1 and 7.6 GPa, the simulation results are in relatively poor agreement with the experimental data as compared to the previous two peak pressures. The simulation predictions tend to overestimate at near surface regions and underestimate at lower depths. The error between the experimental data and simulation results is quantified. Table 11 shows the least square error between the experimental data and simulation results for different models. The error is computed using all nine experimental data locations and the corresponding simulation predictions. Equation 10 is used to obtain the least square error. In Table 11, the lowest error is for peak pressure of 6.6 GPa for both the JC and the KHL models.

Table 11: Least Square Error Comparison for Inconel®718

| Inconel®718 | | | | | | | | |
|---------------------|------------|------------|------------|------------|------------|------------|------------|------------|
| | JC Model | | | | KHL Model | | | |
| Peak Pressure (GPa) | 5.3 | 6.6 | 7.1 | 7.6 | 5.5 | 6.6 | 7.1 | 7.6 |
| Optimized (MPa) | 261.76 | 241.19 | 547.94 | 634.95 | 288.82 | 241.19 | 553.04 | 638.66 |
| Normalized | 1.08 | 1.0 | 2.27 | 2.63 | 1.19 | 1.0 | 2.29 | 2.64 |

The error is normalized to the least error value (set = 1.0) since the relative error is a more important factor than the absolute value. The normalized error values from Table 11 demonstrates that both models perform very similarly at all peak pressures. Table 11 indicates the error between the experimental data and simulation result at a peak pressure of 7.6GPa is 2.64 times the error at the peak pressures of 5.3 GPa for the KHL model.

5.5.2 Validation of Optimization-based Approach and Comparison with Traditional Approach for Ti-6Al-4V

Three different peak pressures of 5.5, 6.6, and 8.3 GPa were selected for the simulation of the residual stresses based on the availability of the experimental data [38]. Region I is considered up to a depth of 0.2 mm from the surface, Region II is from 0.2 mm to 0.6 mm and Region III is from 0.6 mm onwards. The optimization-based approach was implemented for the peak pressure of 5.5 GPa for all three material models (the JC, the ZA, and the KHL models). The same model constants are used for the other two peak pressures to evaluate the consistency of the approach. The constants obtained for the JC model using the optimization-based approach are shown in Table 12:

Table 12: Material Model Constants Using Optimization-Based Approach for the JC Model

| Parameter | Value |
|--------------------|------------------------|
| <i>A</i> | 1092.68MPa |
| <i>B</i> | 1266.94MPa |
| <i>n</i> | 0.0851 |
| <i>C</i> | 9.39×10^{-3} |
| $\dot{\epsilon}_0$ | $9.0 \times 10^{-4}/s$ |

By comparison, the model constants obtained from the traditional approach [83] are shown in Table 13

Table 13: Material Model Constants Using Traditional Approach for the JC Model [83]

| Parameter | Value |
|--------------------|-------------------------|
| A | $950.23MPa$ |
| B | $603.28MPa$ |
| n | 0.19921 |
| C | 0.0198 |
| $\dot{\epsilon}_0$ | $9.32 \times 10^{-4}/s$ |

The constants obtained for the ZA model using the optimization-based approach are shown in Table 14

Table 14: Material Model Constants Using Optimization-Based Approach for the ZA Model

| Parameter | Value |
|--------------|-----------------------|
| σ_a | $472.89MPa$ |
| B | $247.13MPa$ |
| β_0 | 1.16×10^{-6} |
| β_1 | 0.01598 |
| B_0 | $2221.87MPa$ |
| ϵ_r | 0.0308 |
| α_0 | 10^{-6} |
| α_1 | 1.85×10^{-4} |

By comparison, the model constants obtained from the traditional approach are:

Table 15: Material Model Constants Using Traditional Approach for the ZA Model [83]

| Parameter | Value |
|--------------|-----------------------|
| σ_a | $945.19MPa$ |
| B | $246.65MPa$ |
| β_0 | 1.16×10^{-6} |
| β_1 | 0.1065 |
| B_0 | $1481.25MPa$ |
| ϵ_r | 0.0538 |
| α_0 | 10^{-6} |
| α_1 | 3.16×10^{-4} |

The constants obtained for the KHL model using the optimization-based approach are shown in Table 16

Table 16: Model Constants Using Optimization-Based Approach for the KHL Model

| Parameter | Value |
|-----------|---------------------|
| A | 677.71MPa |
| B | 917.761MPa |
| n_1 | 0.1526 |
| n_0 | 0.0931 |
| C | 0.0415 |

The constants obtained for the KHL model using the traditional approach are:

Table 17: Material Model Constants Using Traditional Approach for the KHL Model

| Parameter | Value |
|-----------|---------------------|
| A | 1170.10MPa |
| B | 812.511MPa |
| n_1 | 0.4481 |
| n_0 | 0.3301 |
| C | 0.0212 |

Figure 41, 42, and 43 shows the residual stress results at peak pressures of 5.5, 6.1, and 8.3 GPa respectively for the JC model. For the peak pressure of 5.5 GPa, the results predicted by the optimization-based approach are closer to the experimental results than the traditional approach. Compared to the traditional approach, the new approach performs well, especially at the surface. The consistency of the new approach can be seen in Figures 42 and 43, where the results predicted by simulations follow the trends with the experimental results. However for the peak pressure of 6.1 GPa, the new approach underestimates at the surface. This could be attributed to the number of shots. The number of shots for peak pressures of 5.5 and 8.3 GPa is only one, while the number of shots for 6.1 GPa is three. The constitutive material model is not optimized for multiple shots.

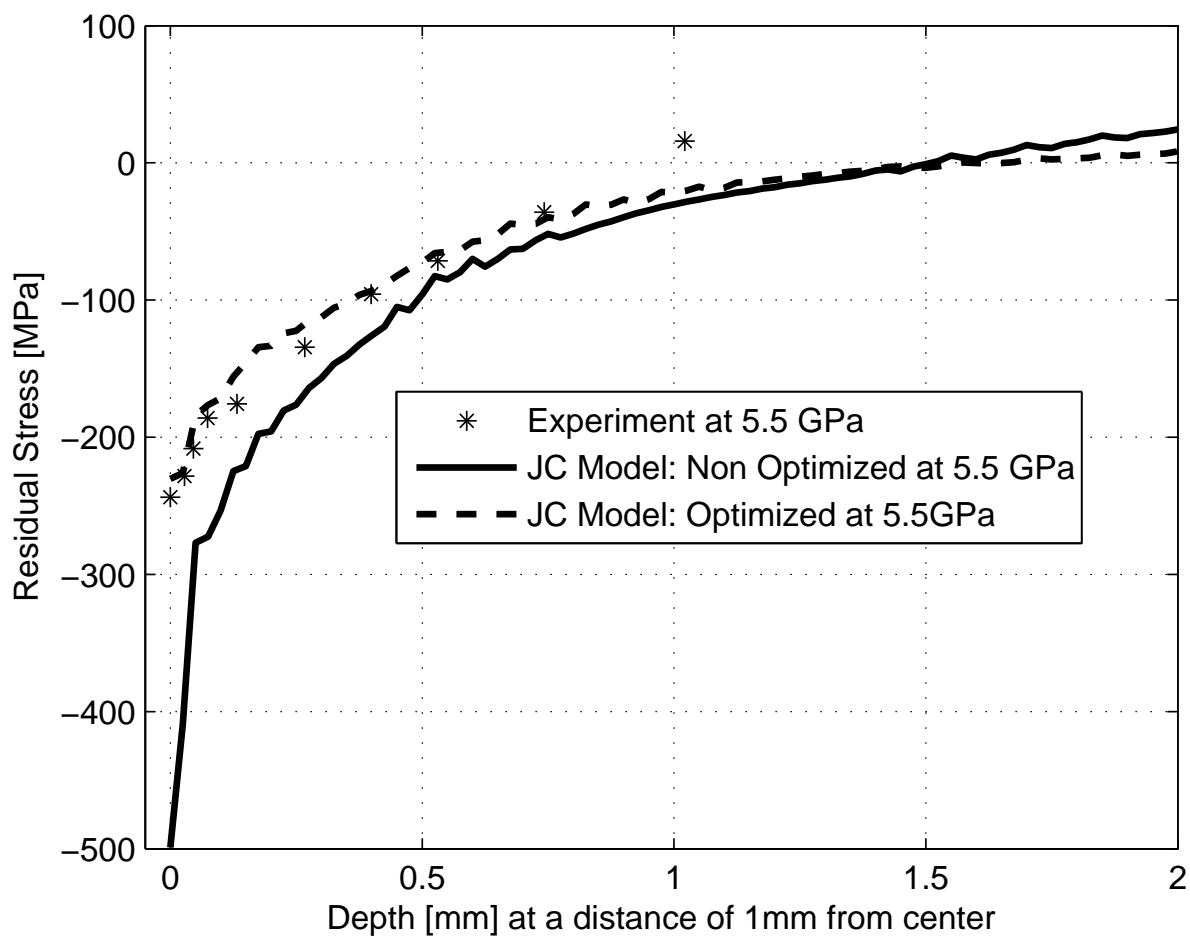


Figure 41: Residual Stress Comparison for Ti-6Al-4V for the JC Model with 5.5 Peak Pressures

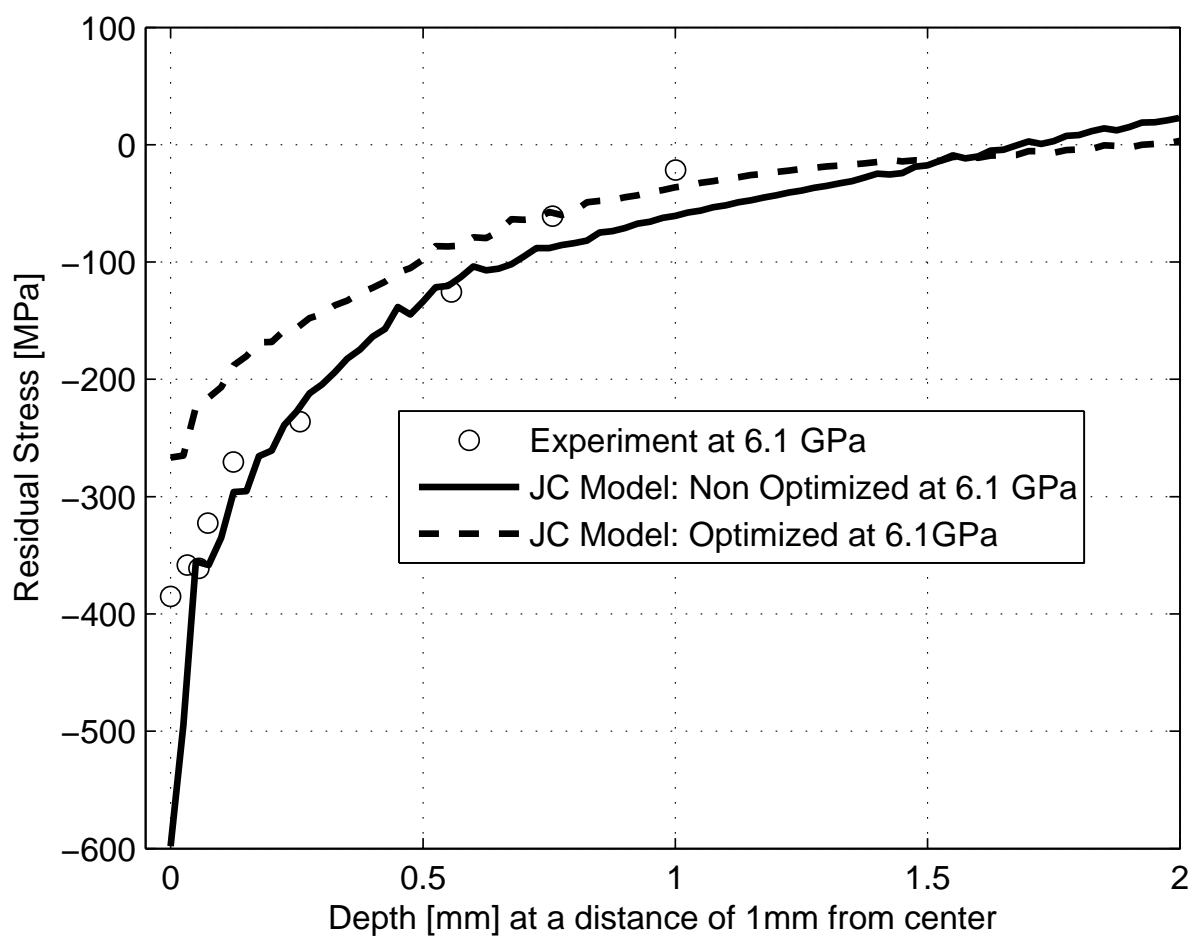


Figure 42: Residual Stress Comparison for Ti-6Al-4V for the JC Model with 6.1 Peak Pressures

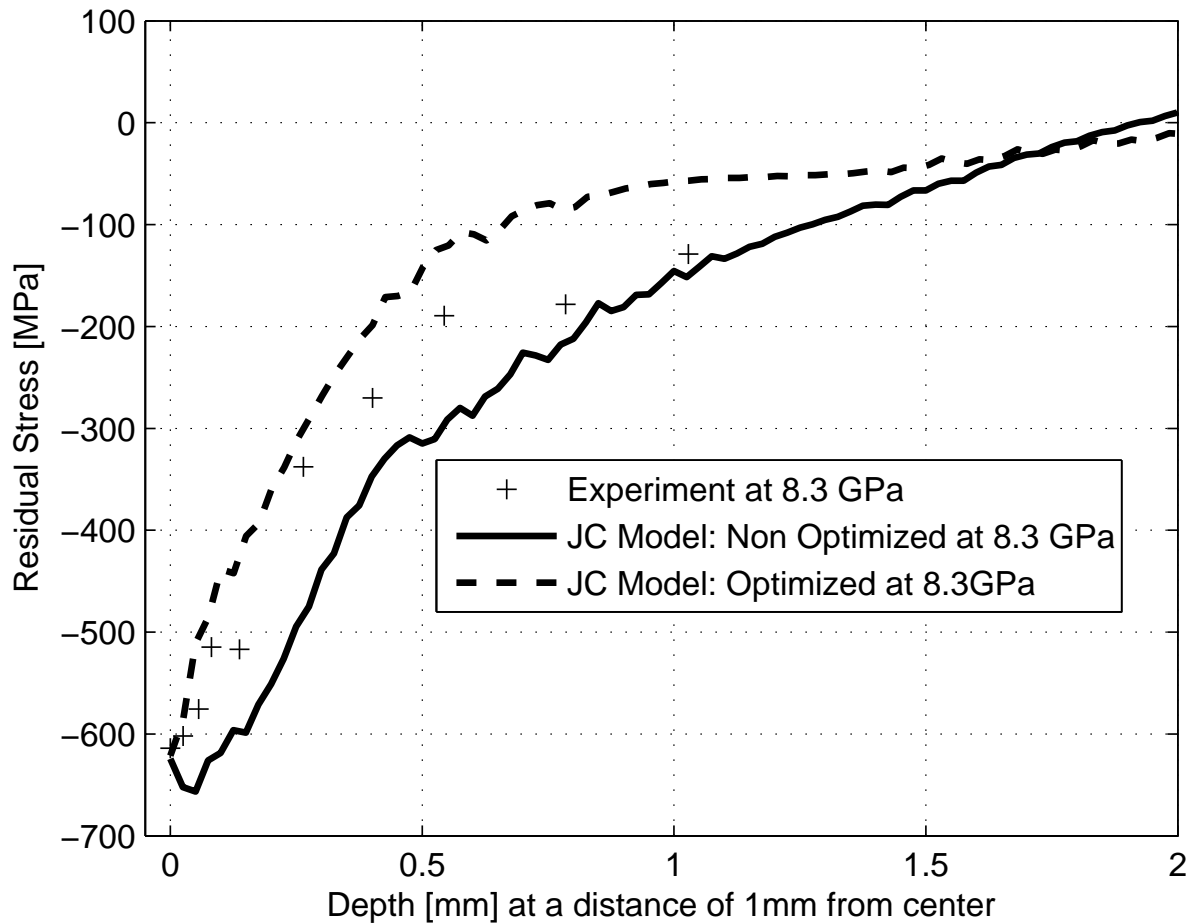


Figure 43: Residual Stress Comparison for Ti-6Al-4V for the JC Model with 8.3 Peak Pressures

The common feature of all three peak pressures in the new approach is underestimation of the residual stresses predictions compared to the experimental results. This approach could be considered as a conservative design. The results of the residual stress using the ZA model for the three peak pressures of 5.5, 6.1, and 8.3 GPa are shown in Figures 44, 45, and 46 respectively.

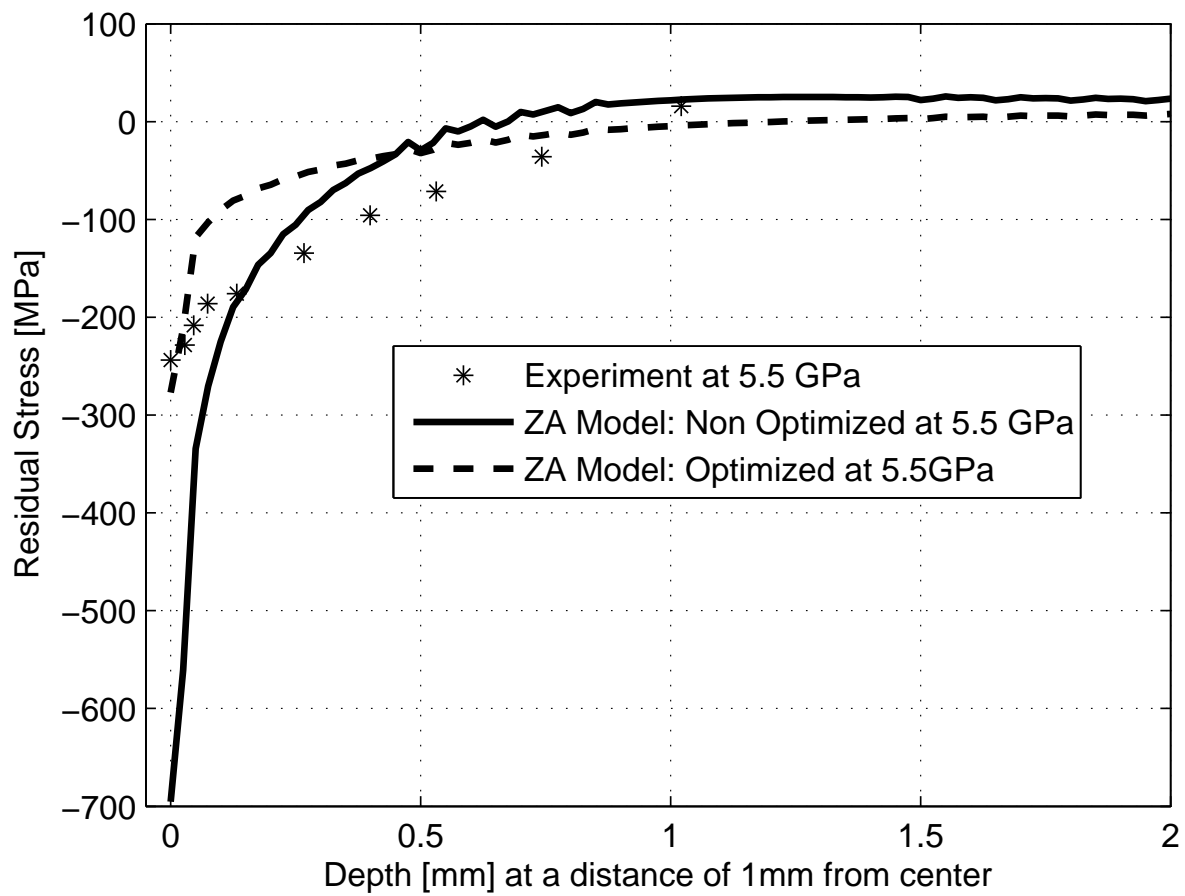


Figure 44: Residual Stress Comparison for Ti-6Al-4V for the ZA Model with 5.5 Peak Pressures

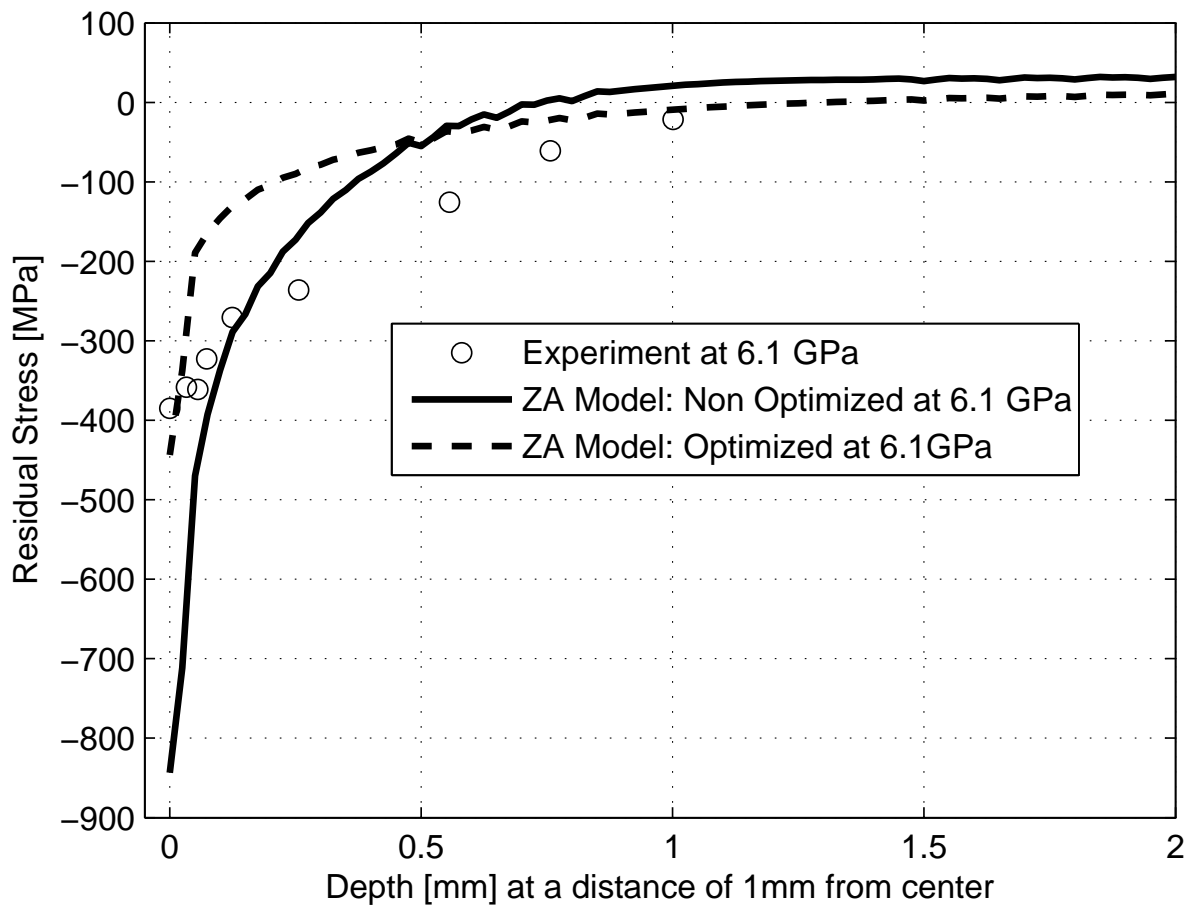


Figure 45: Residual Stress Comparison for Ti-6Al-4V for the ZA Model with 6.1 Peak Pressures

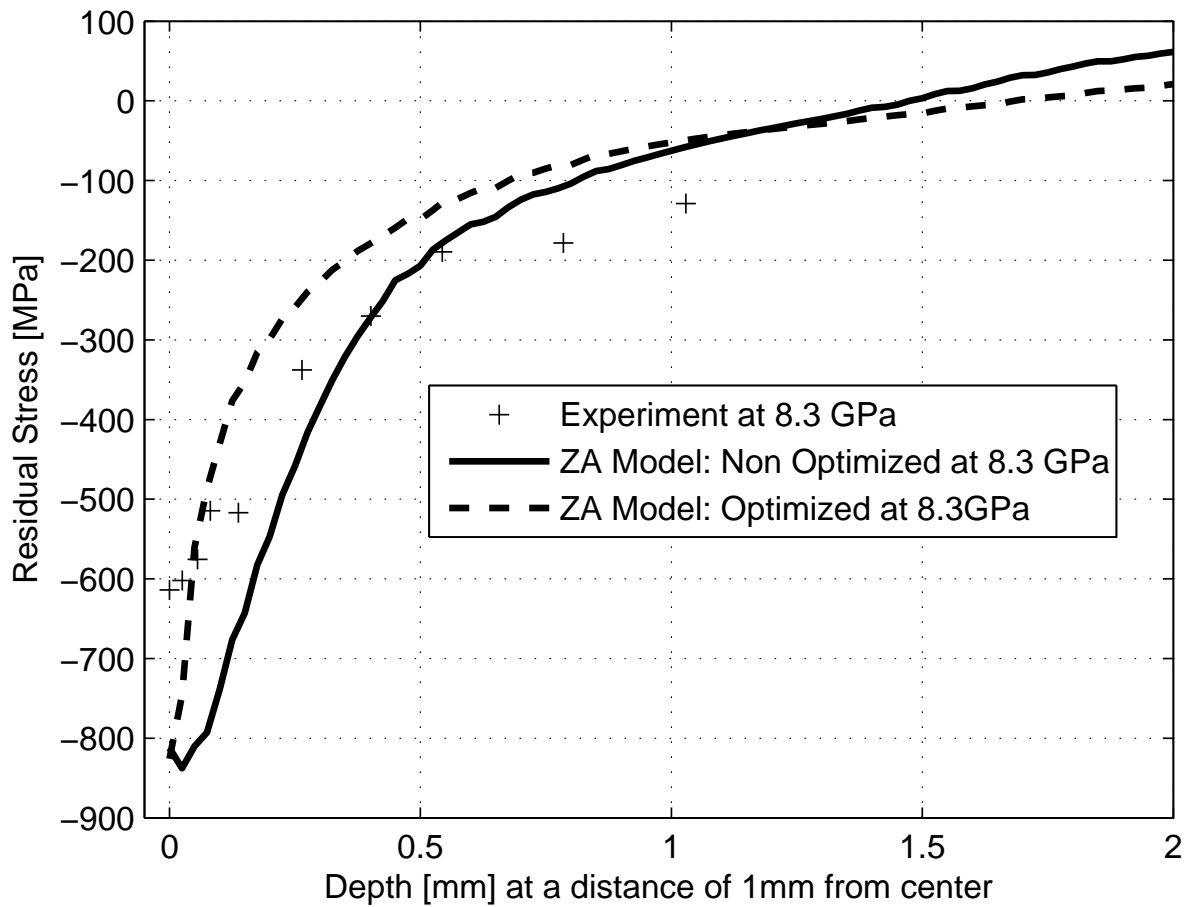


Figure 46: Residual Stress Comparison for Ti-6Al-4V for the ZA Model with 8.3 Peak Pressures

The consistency of the approach is evident in these figures compared to experimental results. The new approach performs well at the surface for peak pressure of 5.5 GPa and 6.1 GPa, while it overestimates at the surface for the peak pressure of 8.3 GPa. On the other hand, the traditional approach overestimates for all the peak pressures compared to the experimental results. Figures 47, 48, and 49 show the residual stress comparison between the experiment and simulations for the KHL model at peak pressures of 5.5, 6.1, and 8.3 GPa respectively. As seen in the previous two models, the KHL model performs well compared to the experimental results for three different peak pressures including the surface. The same model using the traditional approach over predicts at the surface for peak pressures of 5.5 and 6.1 GPa. This shows that the optimization-based approach is consistent in predicting the residual stresses using three different models. In most cases in this work, it performs better than the traditional approach. However, we cannot include this for every case because the residual stress prediction based on the traditional approach is dependent on the amount and quality of the experimental data available.

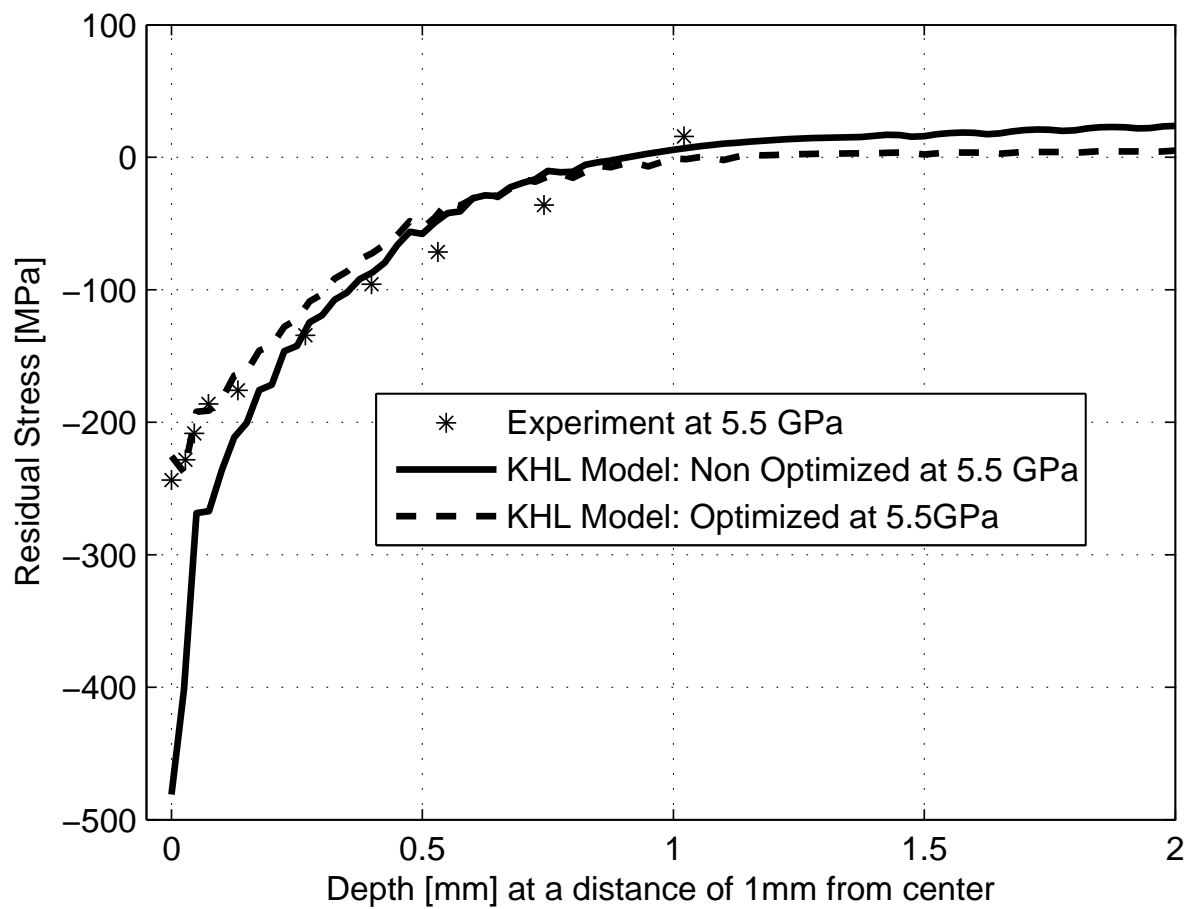


Figure 47: Residual Stress Comparison for Ti-6Al-4V for the KHL Model with 5.5 Peak Pressures

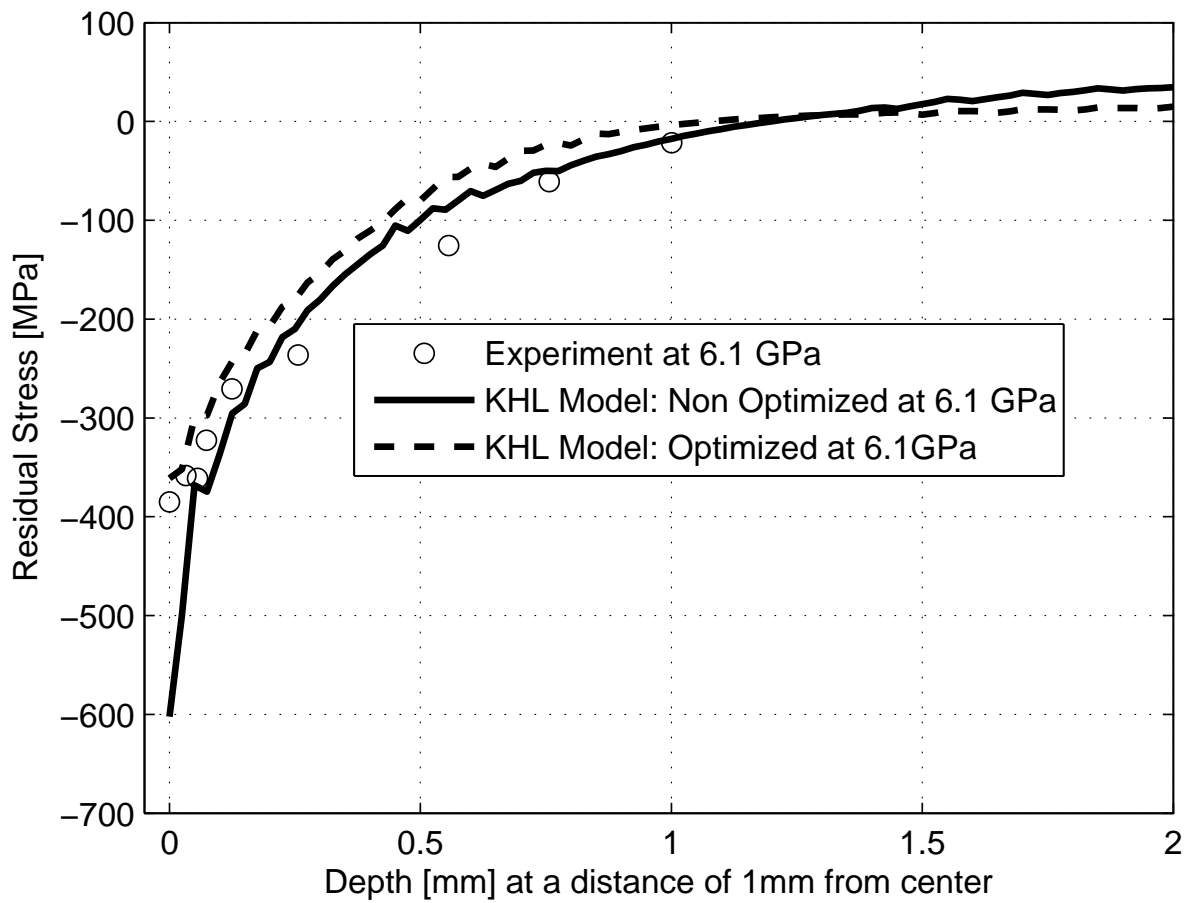


Figure 48: Residual Stress Comparison for Ti-6Al-4V for the KHL Model with 6.1 Peak Pressures

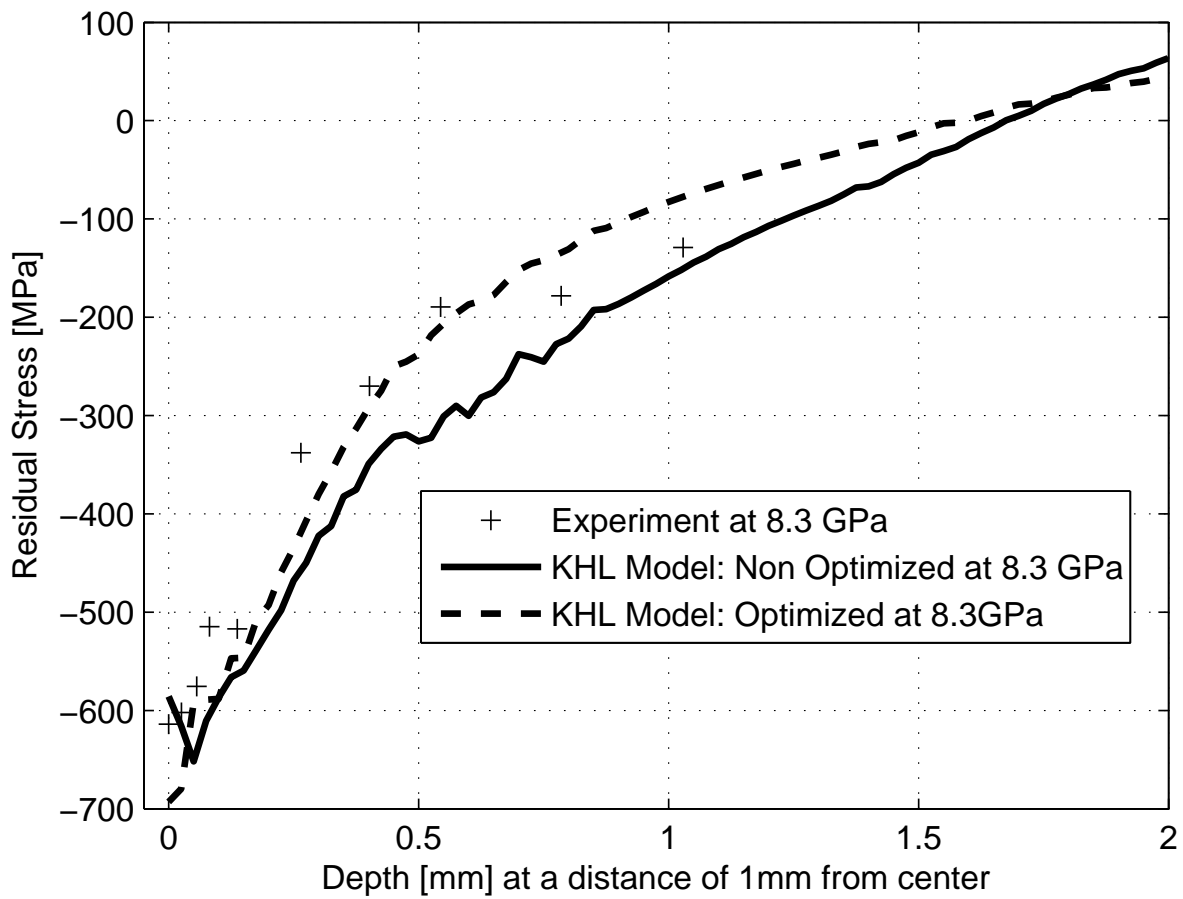


Figure 49: Residual Stress Comparison for Ti-6Al-4V for the KHL Model with 8.3 Peak Pressures

Table 18 shows the least square error using Equation 12 and the normalized error between the experimental data and the simulation results for all models. The simulation predictions include the traditional approach (non-optimized) and the optimization-based approach.

Table 18: Least Square Error Comparison for Ti-6Al-4V

| Ti-6Al-4V | | | | | | | | | |
|----------------------------|----------|--------|--------|-----------|--------|--------|----------|--------|--------|
| | JC Model | | | KHL Model | | | ZA Model | | |
| | 5.5 | 6.1 | 8.3 | 5.5 | 6.1 | 8.3 | 5.5 | 6.1 | 8.3 |
| Peak Pressure (GPa) | | | | | | | | | |
| Non-Optimized (MPa) | 446.46 | 358.14 | 300.74 | 410.84 | 365.99 | 278.33 | 759.47 | 780.87 | 559.04 |
| Optimized (MPa) | 46.43 | 231.15 | 178.13 | 51.80 | 90.08 | 228.08 | 164.39 | 269.08 | 404.89 |
| Normalized (Non-Optimized) | 9.62 | 7.71 | 6.47 | 8.84 | 7.88 | 5.99 | 17.48 | 16.80 | 12.04 |
| Normalized (Optimized) | 1.0 | 4.98 | 3.83 | 1.12 | 1.94 | 4.91 | 3.54 | 5.79 | 8.72 |

This table provides a quantitative comparison between the two approaches. In Table 18, the least squared error is normalized to the least value that occurs for the JC model using the optimized approach at the peak pressure of 5.5 GPa. The JC and the KHL models perform very well compared to the ZA model for all the peak pressures for both approaches. It can be seen that the maximum error for the optimization-based approach is 8.72 times the least error value while it is 12.04 times the least error value for the traditional approach.

5.6 Section Summary and Conclusions

In this chapter, an inverse optimization-based approach is used to obtain model constants when very little or no experimental data of stress-strain curves is available. The optimization-based approach is shown to predict residual stresses that are consistent with experimental results. The consistency of the approach is shown by validating for two materials of Inconel®718 and Ti-6Al-4V. LP experiments were performed with a Nd-glass laser for Inconel®718 at four different energy densities and the residual stress measurements were made using an x-ray diffraction method. For the Inconel®718, the JC and the KHL models predicted the trends and the simulation results are in agreement with the experimental results for the lower two peak pressures. The JC and the KHL models are shown to perform better than the ZA model in prediction of residual stresses compared to experimental data for Ti-6Al-4V.

6.0 PROBABILISTIC FRAMEWORK FOR LASER PEENED RESIDUAL STRESS FIELD BY PROPAGATION OF REGRESSION UNCERTAINTY

This chapter develops a methodology to quantify the uncertainty in residual stress field, i.e., residual stress value along the depth induced by the LP process simulation. The LP process simulation is described in the context of uncertainty quantification. The cause of uncertainty in simulation of LP is discussed. The input uncertainty is the regression estimates obtained from the non-linear regression analysis. The effect of these uncertainties on the residual stress field is presented.

6.1 Deterministic LP Simulation Procedure

The simulation procedure to predict residual stress field induced by the LP process has been discussed in the previous chapters. The simulation procedure is described in this section with the purpose of making distinctions between deterministic simulation procedure with stochastic simulation procedure. A schematic of the simulation procedure is shown in Figure 50.

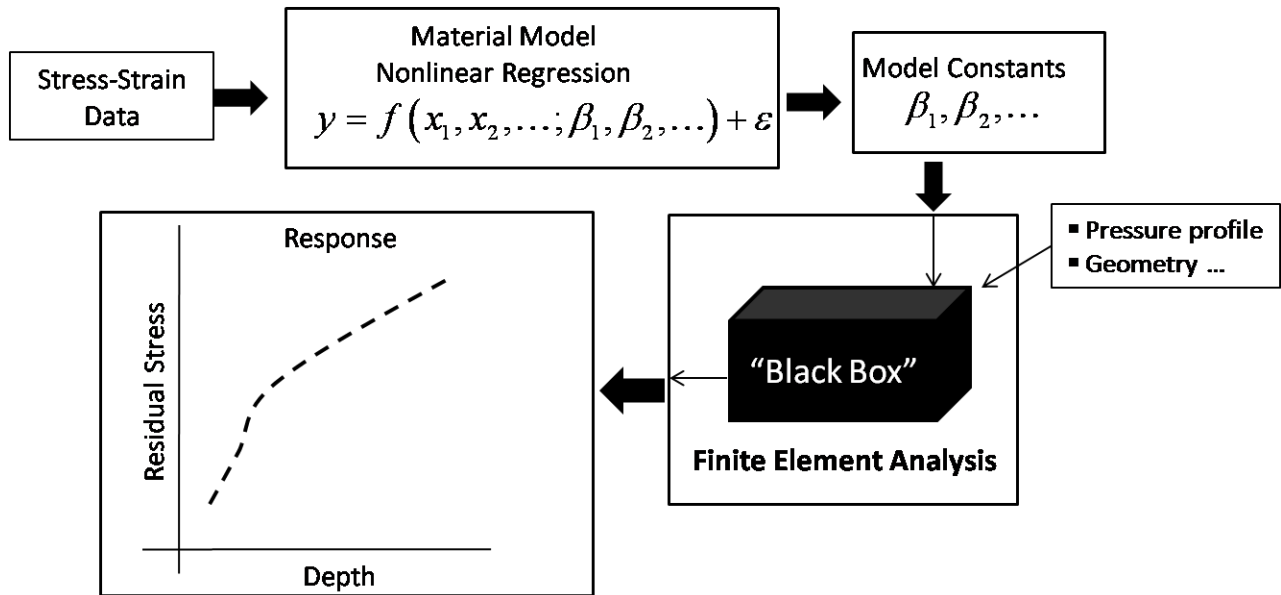


Figure 50: Deterministic Simulation Procedure of the LP Process

The deterministic simulation procedure can be divided into three components:

1. Obtain the estimates of material model constants from a non-linear regression analysis based on limited experimental data
2. Input the model constant estimators and other process parameters such as peak pressure, spatial and temporal pressure profile, and spot size into FEA
3. Compare the predicted residual stress field at different depths with the experimental data

The material model constant estimates act as one set of inputs to the FEA and residual stress field is obtained as the response from the FEA.

6.2 Cause and Effect of Uncertainty in LP Simulation

During the simulation process, a material model is required which acts as one of the inputs to FEA. The residual stress field obtained is considered as the response. A material model is an equation relating stresses to strains at different strain rates and predicts the behavior of the material under different loading conditions. Each material model has certain parameters or model constants that must be estimated. These model constants are determined using non-linear regression and least squares approach is typically used to estimate the model constants. An error term in the non-linear model is assumed to be random and therefore estimates of the model constants obtained are also random. This randomness in the model constant estimates causes uncertainty in the input and is termed as regression uncertainty. This uncertainty represents the variability of the material model to predict the material behavior. The uncertainty in the input is propagated through the system (FEA) or black box to obtain the uncertainty in the response (residual stress field). The uncertainty in the response is expressed as confidence band on the residual stress field.

6.3 Probabilistic Framework for LP Simulation

In this research, a framework is developed to address the uncertainty in the model constant estimates that leads to variability in the residual stress field. The schematic representation of the framework is shown in Figure 51.

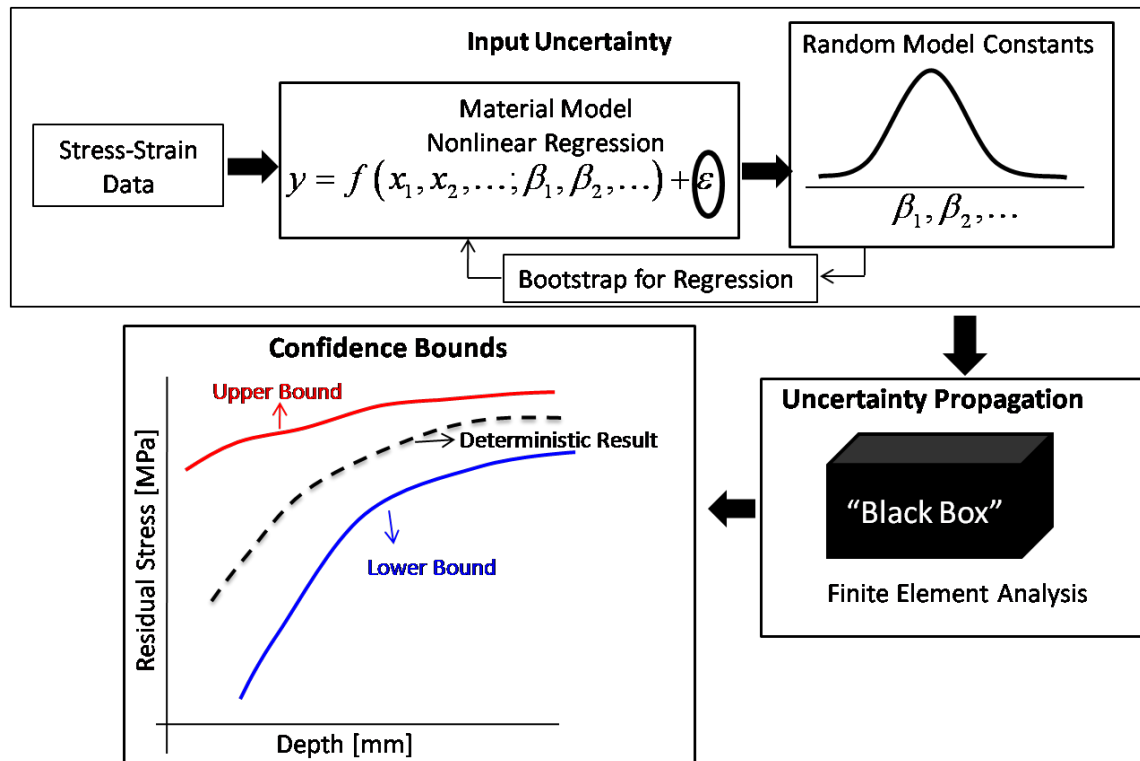


Figure 51: Probabilistic Framework for LP Simulation

The framework is divided into three components:

1. Regression (Input) Uncertainty Quantification
2. Uncertainty Propagation
3. Residual Stress Field Confidence Band

6.3.1 Regression (Input) Uncertainty

Regression analysis is a technique from statistics that can be used to investigate the relationship between a dependent variable and one or more independent variables. Applications of the regression technique are found in many fields including engineering, physical sciences, economics, management, and biological sciences. According to Montgomery and Peck [84], regression analysis is the most widely used statistical technique. Regression analysis can be used for purposes such as data description, parameter estimation, prediction and estimation, and control. Regression analysis can be categorized into two divisions:

1. Linear Regression Analysis
2. Non-linear Regression Analysis

The simplest linear regression model is shown in Equation 14.

$$y = \beta_0 + \beta_1 x + \varepsilon \quad (14)$$

where x is the independent variable, β_0 and β_1 are the regression coefficients that need to be estimated, y is the dependent variable, and ε is a random error. Equation 14 is considered a linear regression model because the equation is linear in coefficients. The least squares method is typically used to estimate the regression coefficients. The error term is assumed to be $NID(0, \sigma^2)$, normal and independently distributed with zero mean and constant variance of σ^2 . The assumption of zero mean in the error is primarily used for simplifying the number of unknown regression coefficients. A non-zero mean is absorbed in the intercept (β_0) of the model. The assumption of constant variance of value σ^2 simply states that the observed experimental data values obtained are equally unreliable. Further analysis can be performed to test this assumption and variance-stabilization transformation can also be implemented [85]. The least squares estimator of vector $\underline{\beta}$ is shown in Equation 15:

$$\underline{\hat{\beta}} = (X^T X)^{-1} X^T \underline{y} \quad (15)$$

where X is a matrix of levels of the independent variables and a column of ones for the intercept and \underline{y} is the vector of observations. The size of \underline{y} is $n \times 1$, where n is the number of observations. The size of X is $n \times k$, where k represents the number of regression coefficients which includes the intercept term β_0 . The size of the vector $\underline{\hat{\beta}}$ is $k \times 1$. The fitted regression model is shown in Equation 16:

$$\underline{\hat{y}} = X \underline{\hat{\beta}} \quad (16)$$

where $\underline{\hat{y}}$ is known as fitted values or predicted values. The difference between actual observation y_i and fitted value \hat{y}_i is the residual, $e_i = y_i - \hat{y}_i$. The vector of residuals $n \times 1$ is $\underline{e} = \underline{y} - \underline{\hat{y}}$. The formula for estimating the error variance (σ^2) is shown in Equation 17:

$$\hat{\sigma}^2 = \frac{\underline{y}^T \underline{y} - \underline{\hat{\beta}}^T X^T \underline{y}}{n - k} \quad (17)$$

The variance property of $\underline{\hat{\beta}}$ is expressed as a covariance matrix obtained by $Cov(\underline{\hat{\beta}}) = \sigma^2 (X^T X)^{-1}$ [86]. Error variance estimated in Equation 17 is used for the error variance term to obtain the estimate of the covariance matrix. The size of the covariance matrix is $k \times k$. The covariance matrix is a symmetric matrix whose i^{th} diagonal element is the variance of the individual regression coefficient estimate $\hat{\beta}_i$ and ij^{th} element is the covariance between estimates $\hat{\beta}_i$ and $\hat{\beta}_j$. Assuming a normal error, the regression coefficient estimators $\underline{\hat{\beta}}$ will have multivariate normality distribution. Confidence intervals for individual regression coefficients can be found in Montgomery's work [86].

Engineers experience non-linear regression models in day to day life. The common notation for a non-linear regression model is shown in Equation 18:

$$y = g(x; \beta_0, \beta_1, \dots, \beta_k) + \varepsilon \quad (18)$$

where \underline{x} is the vector of independent variables and β_i $i = 1, 2, \dots, k$ are the regression coefficients that need to be estimated. The term 'non-linear' is used because the function g is non-linear in the coefficients (β_i). Unlike linear regression models, there is no closed form solution available to estimate the regression coefficients in a non-linear model. Instead, iterative optimization techniques such as Gauss-Newton algorithm is used. The basic idea of the Gauss-Newton algorithm is approximating the function g by a first order Taylor series expansion. This linear approximation is used in least squares approach. A Jacobian matrix, which is composed of partial differential of function g with respect to each parameter β_i , $\frac{\partial g}{\partial \beta_i}$ is obtained. An initial value is proposed for the regression coefficients and the coefficients are updated until convergence is reached. The details of the algorithm can be found in the work of Ratkowsky [87].

The covariance matrix $[\psi]$ between the regression coefficient estimates can be estimated from the linearized approximation of the function g . The partial differential of function g with respect to each regression estimate β_j for an independent variable x_i is denoted by Equation 19:

$$c_{ij} = \frac{\partial g(\hat{\beta}, x_i)}{\partial \hat{\beta}_j} \quad (19)$$

and $[C] = \{c_{ij}\}$. Compared to the linear regression analysis, matrix $[C]$ is analogous to matrix $[X]$. The size of the matrix $[C]$ is $n \times k$, where n is number of observations and k represents the number of regression coefficients. The equation for the estimated covariance between the regression estimates is shown in Equation 20:

$$[\psi] = \hat{\sigma}^2 [C^T C]^{-1} \quad (20)$$

where $\hat{\sigma}^2$ is the estimated error variance as shown in Equation 17.

The estimates of the regression coefficients are approximately normal. The approximate normal distribution gets closer to the asymptotic limit as the sample size gets larger based on law of large numbers and central limit theorem. For a limited sample size, which is mostly the case in engineering, it is desirable to validate the normality assumption. In this research an approach from statistics known as "bootstrap for regression" is used to verify the normality assumptions of the regression coefficient estimates [88]. The following section details bootstrapping.

6.3.2 What is Bootstrapping?

Bootstrapping is a modern, computer-intensive statistical technique. It has been initiated by Efron and the first monograph was published in 1993 [89]. Bootstrapping can be used to estimate the standard errors of means, variances as well as more complicated statistics. It can also be used to construct hypothesis tests. Bootstrapping falls into the category of sampling with replacement (except few exceptions). Bootstrapping provides additional details than a simple statistic from a sample. Figure 52 shows a generic flow chart of the bootstrapping method. The figure can be easily understood with an example. Suppose the initial sample data of an observed quantity is 10, 13, 15, 18, and 20. 'Mean' of the data can be obtained and represents the sample statistic. The mean of the above data is 15.2. Bootstrapping can provide us additional information such as the

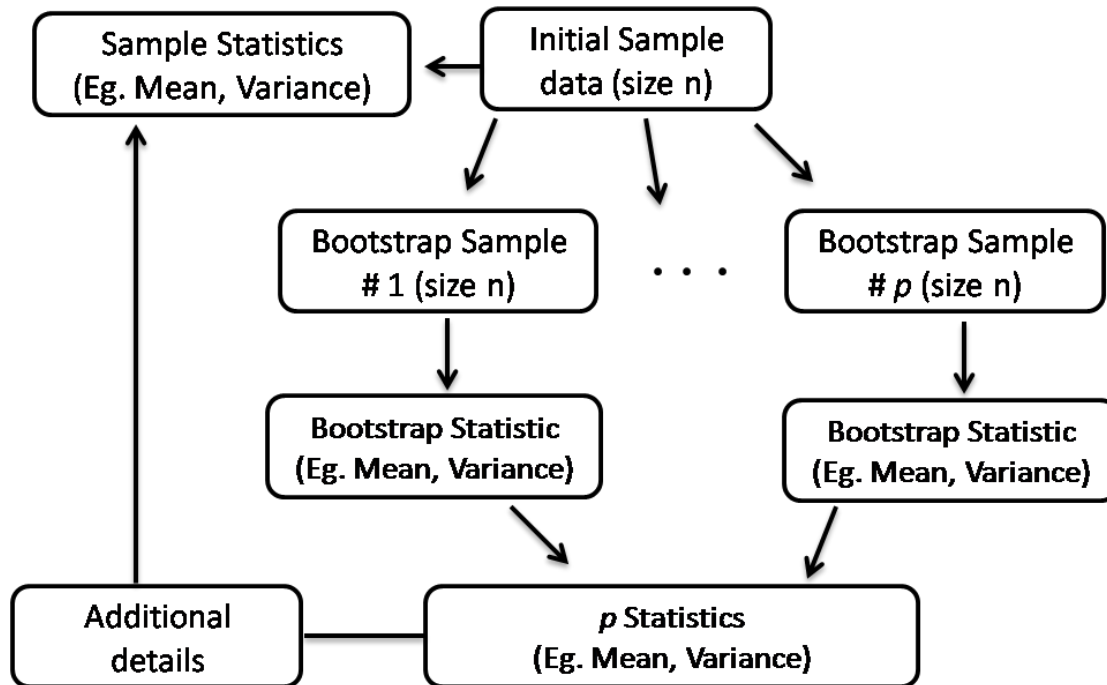


Figure 52: Schematic Representation of Bootstrap Method

distribution of the mean. It can be assumed that there are five balls in a basket numbered 10, 13, 15, 18, and 20. A ball is randomly sampled and then placed back in the basket. This is known as sampling with replacement. There are again all five balls in the basket when the next ball is randomly sampled. The procedure is repeated five times to obtain the first bootstrap sample. The first bootstrap sample obtained using MATLAB [90] is 18, 13, 20, 13, and 18 and the mean of the bootstrap sample is 16.4. As it can be seen from the first bootstrap sample, the numbers 13 and 18 appears twice, the numbers 10 and 15 does not appear at all. Another possible bootstrap sample can be that all five samples can be the same number. In this manner p bootstrap samples are generated from the initial sample. The typical values of p range from 500 to 5000. Figure 53 shows the histogram of the 3000 bootstrap samples. The number of bootstrap samples (3000) is chosen large enough so that the results are invariant of the number of bootstrap samples. The variation of the mean that is centered around the sample mean can be seen from the histogram data. The power of the method lies in the fact that additional samples are being generated from the initial sample. This indicates that no new experiments are conducted to obtain the additional information. In the above example, the sample statistic was the mean of the data, but the technique can also be used for other sample statistics. Bootstrap method has been used by Picheny et. al. to conservatively estimate the reliability of engineering structures. Probability of failure of a composite panel is estimated using different methods and the results are compared with the bootstrap method [91].

6.3.2.1 Bootstrapping for Regression

Bootstrapping can also be used for regression. There are three ways to bootstrap a regression analysis [92], which are divided into two categories: (i) parametric bootstrap and (ii)

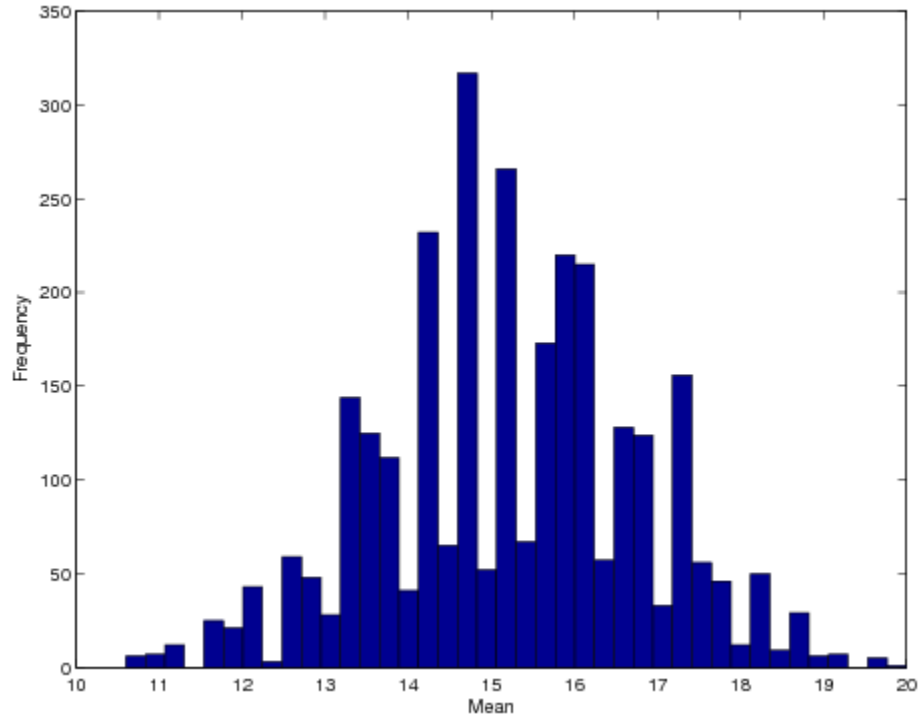


Figure 53: Histogram of Mean of the Sample Data

non-parametric bootstrap. Example 10-1 from Montgomery's book [86] in Chapter 10 is used to demonstrate the bootstrap methods. Sixteen observations of an experiment on the viscosity of a polymer (y) and two process variables, reaction temperature (x_1) and catalyst feed rate (x_2), are shown in Table 19. A linear regression model as shown in Equation 21 is used to fit the experimental data.

$$y = \beta_0 + \beta_1 x_1 + \beta_2 x_2 + \varepsilon \quad (21)$$

Table 19: Viscosity Data of Demonstration Example [86]

| Observation | Temperature (x_1) | Catalyst Feed Rate (x_2) | Viscosity (y) |
|-------------|-----------------------|------------------------------|-------------------|
| 1 | 80 | 8 | 2256 |
| 2 | 93 | 9 | 2340 |
| 3 | 100 | 10 | 2426 |
| 4 | 82 | 12 | 2293 |
| 5 | 90 | 11 | 2330 |
| 6 | 99 | 8 | 2368 |
| 7 | 81 | 8 | 2250 |
| 8 | 96 | 10 | 2409 |
| 9 | 94 | 12 | 2364 |
| 10 | 93 | 11 | 2379 |
| 11 | 97 | 13 | 2440 |
| 12 | 95 | 11 | 2364 |
| 13 | 100 | 8 | 2404 |
| 14 | 85 | 12 | 2317 |
| 15 | 86 | 9 | 2309 |
| 16 | 87 | 12 | 2328 |

The least squares estimates of $\underline{\beta}$ obtained using Equation 15 are shown in Table 20:

Table 20: Regression Coefficients for Linear Regression Model

| Parameter | Value |
|-----------------|---------|
| $\hat{\beta}_0$ | 1566.08 |
| $\hat{\beta}_1$ | 7.62 |
| $\hat{\beta}_2$ | 8.58 |

The variance estimated for the error (σ^2) using the Equation 17 is 16.36. Table 21 shows the observations, the predicted values, and the corresponding residuals or errors. The predicted values are calculated using Equation 16.

Table 21: Observations, Predicted Values, and Residuals for Demonstration Example [86]

| # | Observation (y_i) | Predicted value (\hat{y}_i) | Residual ($e_i = y_i - \hat{y}_i$) |
|----|-----------------------|---------------------------------|--------------------------------------|
| 1 | 2256 | 2244.5 | 11.5 |
| 2 | 2340 | 2352.1 | -12.1 |
| 3 | 2426 | 2414.1 | 11.9 |
| 4 | 2293 | 2294.0 | -1.0 |
| 5 | 2330 | 2346.4 | -16.4 |
| 6 | 2368 | 2389.3 | -21.3 |
| 7 | 2250 | 2252.1 | -2.1 |
| 8 | 2409 | 2383.6 | 25.4 |
| 9 | 2364 | 2385.5 | -21.5 |
| 10 | 2379 | 2369.3 | 9.7 |
| 11 | 2440 | 2416.9 | 23.1 |
| 12 | 2364 | 2384.5 | -20.5 |
| 13 | 2404 | 2396.9 | 7.1 |
| 14 | 2317 | 2316.9 | 0.1 |
| 15 | 2309 | 2298.8 | 10.2 |
| 16 | 2328 | 2332.1 | -4.1 |

Parametric Bootstrap

The parametric bootstrap is based on the belief that the error term in the regression analysis shown in Equation 14 or 18 is $NID(0, \sigma^2)$, normal and independently distributed with zero mean and constant variance. The estimates of the regression coefficients ($\hat{\beta}$) are obtained from the regression analysis as shown in Table 20. The variance of the error is estimated using Equation 17 and the value obtained is 16.36 for the above demonstration example. It is termed as $\hat{\sigma}^2$. Samples of the error are generated based on normal distribution $\underline{\varepsilon}^* \sim N(0, \hat{\sigma}^2)$. The method is termed as 'parametric' because the bootstrap samples are generated from a distribution (e.g. normal) instead of resampling from the original data. The number of samples generated is equal to the number of observations. In the above example, since 16 observations are available, the number of normal random samples of error is also 16. New observation is generated by adding the sampled error to the predicted values, $y_i^* = \hat{y}_i + \varepsilon_i^*$, $i = 1, 2, \dots, n$, where n is the number of observations. In this way a new set of data (x_i, y_i^*) is generated. Using the newly generated data, regression analysis is performed to obtain the estimates of regression coefficients. The procedure is repeated p times, where p is the number of bootstraps. The method is not valid if the error is not normal and this can be a disadvantage of the parametric bootstrap approach. Step by step procedure of the method for the viscosity of polymer example discussed in the previous section is shown in the following.

Random samples of a normal distribution for the error with a mean of zero and variance of 16.36 (estimated variance) is generated. The size of the sample is equal to number of observations, which is 16. The errors are added to the fit or predicted values to generate a new observation.

Table 22 shows one example of the first randomly sampled error, the fit, and the generated observation.

Table 22: Randomly Sampled Error, Predicted Values, and Generated Observations

| # | Random sample of error (ϵ_i^*) | Predicted value (\hat{y}_i) | Generated observation ($y_i^* = \hat{y}_i + \epsilon_i^*$) |
|----|---|---------------------------------|--|
| 1 | 2.0667 | 2244.5 | 2246.57 |
| 2 | -43.5123 | 2352.1 | 2308.59 |
| 3 | 5.3382 | 2414.1 | 2419.44 |
| 4 | -8.8267 | 2294.0 | 2285.17 |
| 5 | 20.0801 | 2346.4 | 2366.48 |
| 6 | 14.4624 | 2389.3 | 2403.93 |
| 7 | 8.7680 | 2252.1 | 2260.87 |
| 8 | 12.9395 | 2383.6 | 2396.54 |
| 9 | 24.0032 | 2385.5 | 2409.50 |
| 10 | -21.8989 | 2369.3 | 2347.40 |
| 11 | 1.5361 | 2416.9 | 2418.44 |
| 12 | -7.9748 | 2384.5 | 2376.53 |
| 13 | -23.4989 | 2396.9 | 2373.40 |
| 14 | -15.8406 | 2316.9 | 2301.06 |
| 15 | 19.0240 | 2298.8 | 2317.82 |
| 16 | 14.7254 | 2332.1 | 2346.83 |

The first bootstrap estimates of $\underline{\beta}$ obtained for the newly generated observation using Equation 15 are $\hat{\beta}_0^* = 1579.12$, $\hat{\beta}_1^* = 7.37$, and $\hat{\beta}_2^* = 9.56$. The procedure of generating normal random samples of error is repeated, and for every sample a bootstrap estimate of the regression coefficients is obtained. Figures 54, 55, and 56 show the histogram of 3000 bootstrap estimates of $\hat{\beta}_0^*$, $\hat{\beta}_1^*$, and $\hat{\beta}_2^*$ respectively. The number of bootstrap samples (3000) is chosen large enough so that the results are invariant of the number of bootstrap samples. Additional information about the estimates is obtained at no further cost of performing an actual experiment.

Non-parametric Bootstrap

There are two methods in non-parametric bootstrap. They are termed as (i) observation resampling or random-x resampling and (ii) residual resampling or fixed-x resampling. Each method is described and comparison between the two are made later. The method is called as 'non-parametric' because the bootstrap samples are not generated from a known distribution, which is the case for a parametric bootstrap. Instead, the samples are generated by resampling the original data.

Random-x Bootstrap: Demonstration example discussed in the previous section is used to explain the method. The viscosity data of a polymer is a vector of observations (\underline{y}) and the

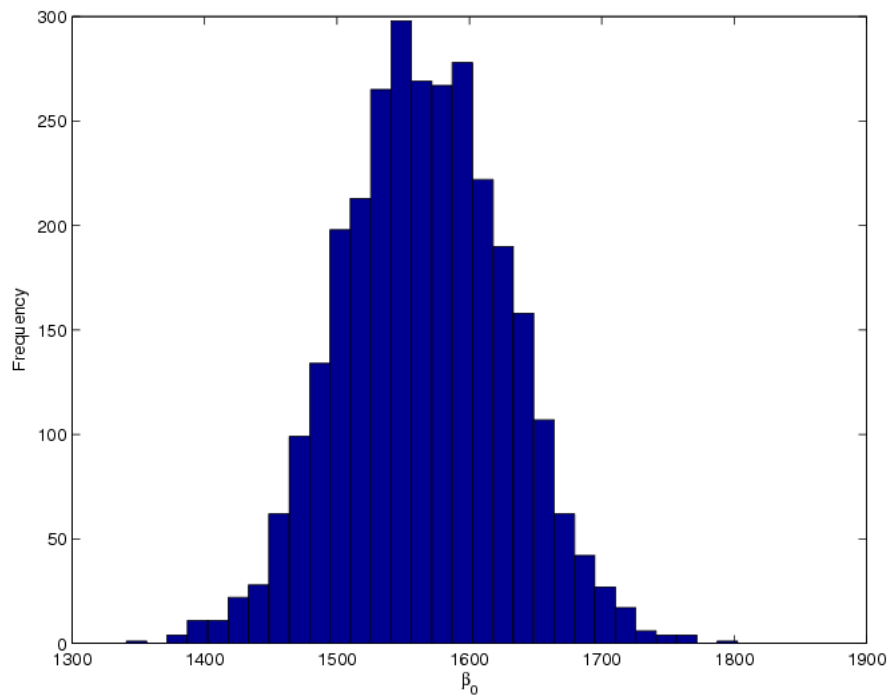


Figure 54: Parametric bootstrap histogram of $\hat{\beta}_0^*$ for the demonstration example

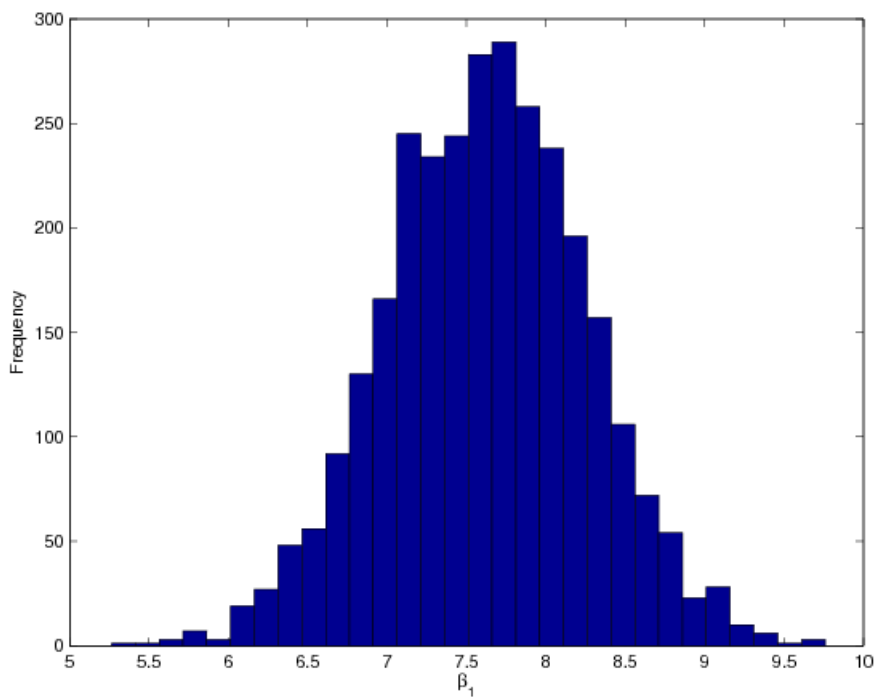


Figure 55: Parametric bootstrap histogram of $\hat{\beta}_1^*$ for the Demonstration Example

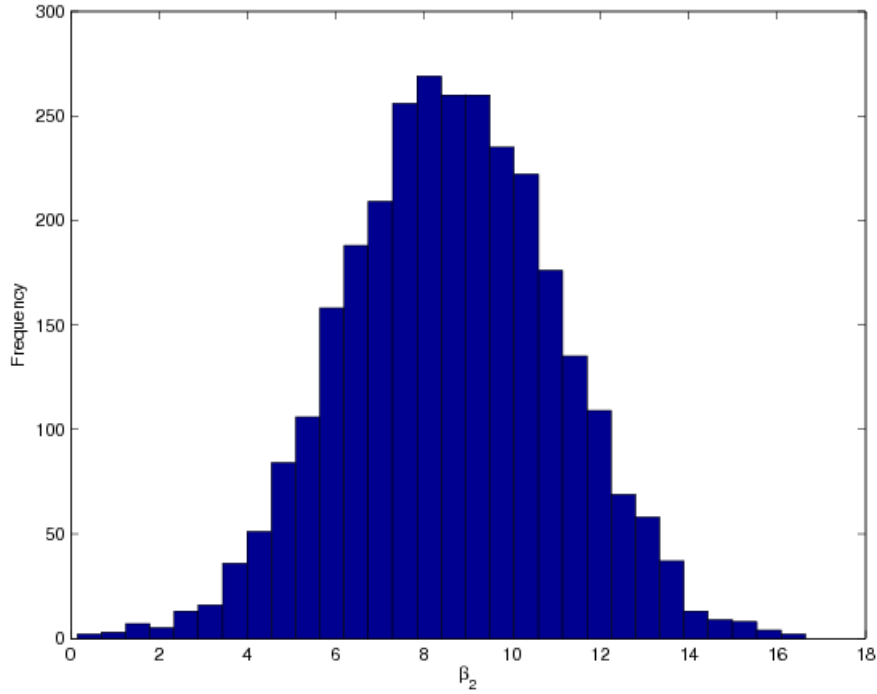


Figure 56: Parametric Bootstrap Histogram of $\hat{\beta}_2^*$ for the Demonstration Example

model-matrix (X) can be written as shown in Equation 22:

$$X = \begin{bmatrix} 1 & 80 & 8 \\ 1 & 93 & 9 \\ 1 & 100 & 10 \\ 1 & 82 & 12 \\ 1 & 90 & 11 \\ 1 & 99 & 8 \\ 1 & 81 & 8 \\ 1 & 96 & 10 \\ 1 & 94 & 12 \\ 1 & 93 & 11 \\ 1 & 97 & 13 \\ 1 & 95 & 11 \\ 1 & 100 & 8 \\ 1 & 85 & 12 \\ 1 & 86 & 9 \\ 1 & 87 & 12 \end{bmatrix}_{16 \times 3} \quad \underline{y} = \begin{bmatrix} 2256 \\ 2340 \\ 2426 \\ 2293 \\ 2330 \\ 2368 \\ 2250 \\ 2409 \\ 2364 \\ 2379 \\ 2440 \\ 2364 \\ 2404 \\ 2317 \\ 2309 \\ 2328 \end{bmatrix}_{16 \times 1} \quad (22)$$

A matrix Z is created by combining the model-matrix X and vector of observations \underline{y} . The first column of the Z matrix is the vector of observations and the remaining columns are from the model-matrix X . The Z matrix obtained for the demonstration example from the Equation 22 is

shown in Equation 23:

$$Z = \begin{bmatrix} 2256 & 1 & 80 & 8 \\ 2340 & 1 & 93 & 9 \\ 2426 & 1 & 100 & 10 \\ 2293 & 1 & 82 & 12 \\ 2330 & 1 & 90 & 11 \\ 2368 & 1 & 99 & 8 \\ 2250 & 1 & 81 & 8 \\ 2409 & 1 & 96 & 10 \\ 2364 & 1 & 94 & 12 \\ 2379 & 1 & 93 & 11 \\ 2440 & 1 & 97 & 13 \\ 2364 & 1 & 95 & 11 \\ 2404 & 1 & 100 & 8 \\ 2317 & 1 & 85 & 12 \\ 2309 & 1 & 86 & 9 \\ 2328 & 1 & 87 & 12 \end{bmatrix}_{16 \times 4} \quad (23)$$

Each row of the Z matrix is considered as a sample data. Bootstrap samples from the rows of the Z matrix are generated and is termed as Z^* . Equation 24 shows an example of a Z^* matrix.

$$Z^* = \begin{bmatrix} 2340 & 1 & 93 & 9 \\ 2250 & 1 & 81 & 8 \\ 2250 & 1 & 81 & 8 \\ 2309 & 1 & 86 & 9 \\ 2440 & 1 & 97 & 13 \\ 2317 & 1 & 85 & 12 \\ 2330 & 1 & 90 & 11 \\ 2404 & 1 & 100 & 8 \\ 2426 & 1 & 100 & 10 \\ 2309 & 1 & 86 & 9 \\ 2379 & 1 & 93 & 11 \\ 2328 & 1 & 87 & 12 \\ 2364 & 1 & 95 & 11 \\ 2340 & 1 & 93 & 9 \\ 2250 & 1 & 81 & 8 \\ 2330 & 1 & 90 & 11 \end{bmatrix}_{16 \times 4} \quad (24)$$

The first row the Z^* matrix is obtained from randomly sampling from one of the rows of the Z matrix. It can be seen from Equation 24, the first row of the Z^* matrix is the second row of the Z matrix. The sampled row from the Z matrix is replaced back so that all the rows of the Z matrix are available to randomly sample for the second row for the Z^* matrix. In this manner all the sixteen rows of the Z^* matrix are generated. It can be seen from the comparison between Equations 23 and 24 that rows 1, 4, 6, 8, and 9 of Z matrix don't appear in the Z^* matrix at all, where as row 7 appears thrice, rows 5 and 15 appears twice, and the remaining rows appear once.

The matrix Z^* can be decomposed into bootstrap model matrix X^* and bootstrap observation vector \underline{y}^* as shown in Equation 25:

$$X^* = \begin{bmatrix} 1 & 93 & 9 \\ 1 & 81 & 8 \\ 1 & 81 & 8 \\ 1 & 86 & 9 \\ 1 & 97 & 13 \\ 1 & 85 & 12 \\ 1 & 90 & 11 \\ 1 & 100 & 8 \\ 1 & 100 & 10 \\ 1 & 86 & 9 \\ 1 & 93 & 11 \\ 1 & 87 & 12 \\ 1 & 95 & 11 \\ 1 & 93 & 9 \\ 1 & 81 & 8 \\ 1 & 90 & 11 \end{bmatrix}_{16 \times 3} \quad \underline{y}^* = \begin{bmatrix} 2340 \\ 2250 \\ 2250 \\ 2309 \\ 2440 \\ 2317 \\ 2330 \\ 2404 \\ 2426 \\ 2309 \\ 2379 \\ 2328 \\ 2364 \\ 2340 \\ 2250 \\ 2330 \end{bmatrix}_{16 \times 1} \quad (25)$$

Bootstrap estimates of the coefficients obtained using Equation 15 are $\beta_0^* = 1536.85$, $\beta_1^* = 7.926$, and $\beta_2^* = 8.671$. The procedure is repeated 3000 times and each time the bootstrap estimates are saved. The number of bootstrap samples (3000) is chosen large enough so that the results are invariant of the number of bootstrap samples. Figures 57, 58, and 59 show the histograms of the bootstrap estimates of $\hat{\beta}_0^*$, $\hat{\beta}_1^*$, and $\hat{\beta}_2^*$ respectively.

Fixed-x Bootstrap: Regression analysis is performed using Equation 15 for a linear model to obtain the estimates. Table 20 shows the obtained estimates for the demonstration example. Table 21 shows the observations (y_i) , $i = 1, 2, \dots, n$, the predicted values or the fit (\hat{y}_i) , $i = 1, 2, \dots, n$, and the errors (e_i) , $i = 1, 2, \dots, n$. n is the number of observations. A bootstrap sample from the obtained errors (e_i) is generated and is termed as e_i^* , $i = 1, 2, \dots, n$. The number of bootstrap errors is equal to the number of observations. New observations are generated by adding the fit to the bootstrap errors, $y_i^* = \hat{y}_i + e_i^*$, $i = 1, 2, \dots, n$. In this way a new data set is generated. Using the newly generated data set, regression analysis is performed to obtain bootstrap estimates of the coefficients. The procedure of bootstrapping the errors is repeated and regression analysis is performed to obtain the bootstrap estimates. The bootstrap estimates are stored for each regression analysis to obtain a distribution of the regression estimates. The difference between the parametric bootstrap and the fixed-x bootstrap is that, for a parametric bootstrap, the errors are sampled from a normal distribution of zero mean and $\hat{\sigma}^2$ variance, while the errors are sampled with replacement from the original regression for the fixed-x bootstrap. Figure 60 shows the flow chart of the fixed-x resampling procedure. Step by step procedure of the method for the demonstration example is shown in the following.

Table 21 shows the observations, predicted values, and the errors of the 16 data points from the original regression analysis. The errors from the original regression analysis are sampled with

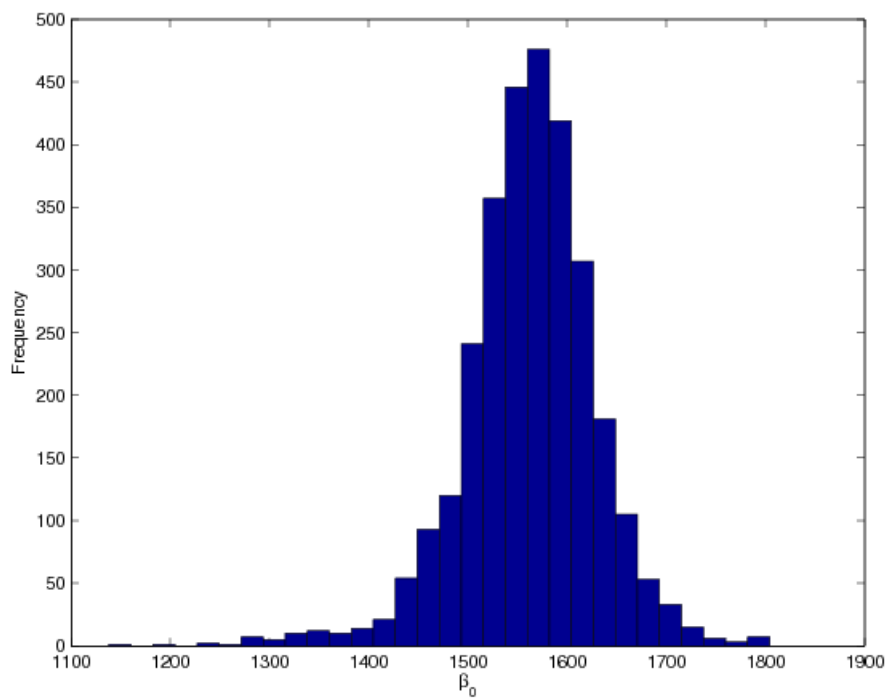


Figure 57: Random-x Bootstrap Histogram of $\hat{\beta}_0^*$ for the Demonstration Example

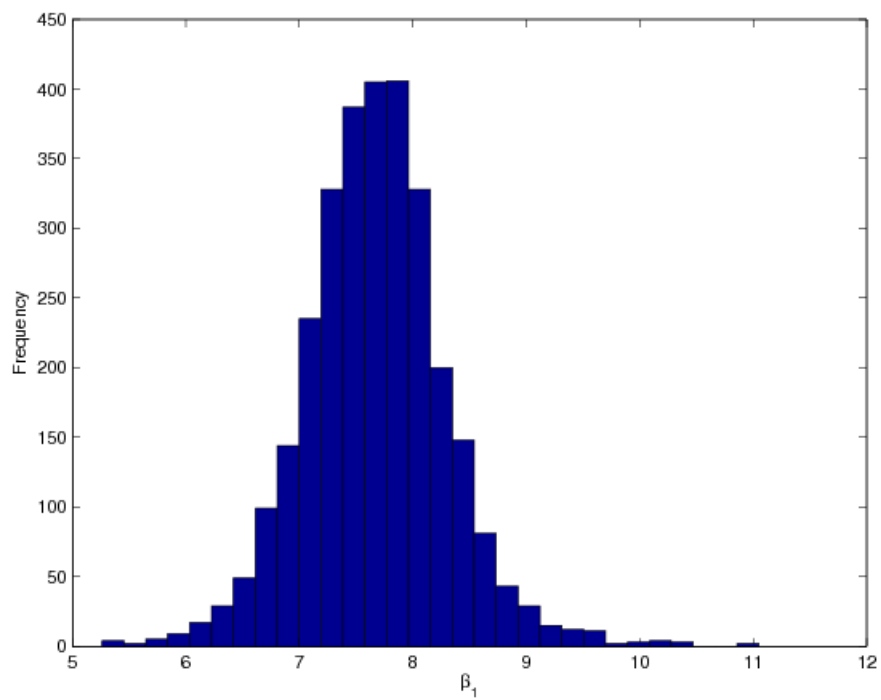


Figure 58: Random-x Bootstrap Histogram of $\hat{\beta}_1^*$ for the Demonstration Example

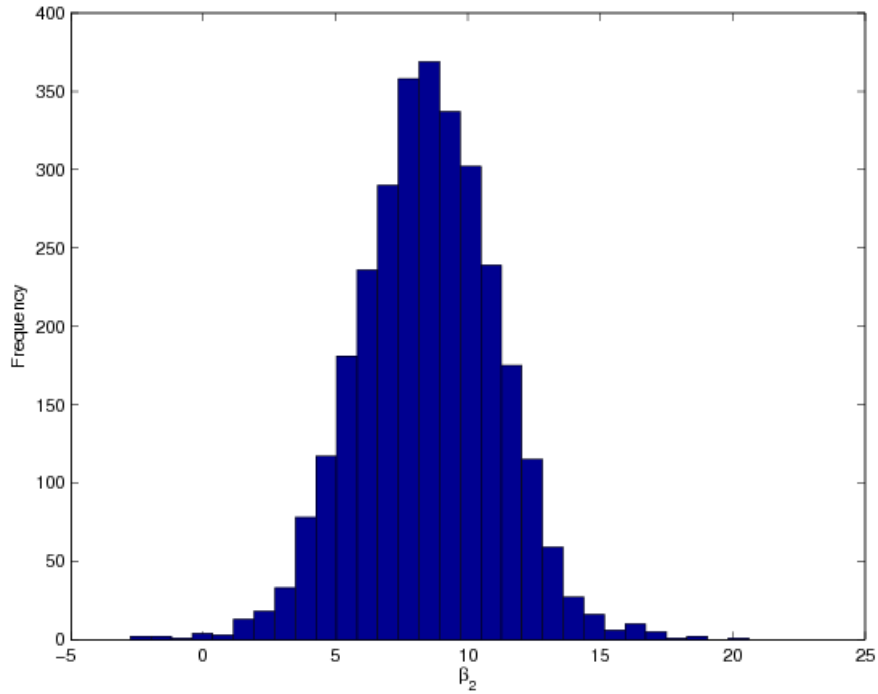


Figure 59: Random-x Bootstrap Histogram of $\hat{\beta}_2^*$ for the Demonstration Example

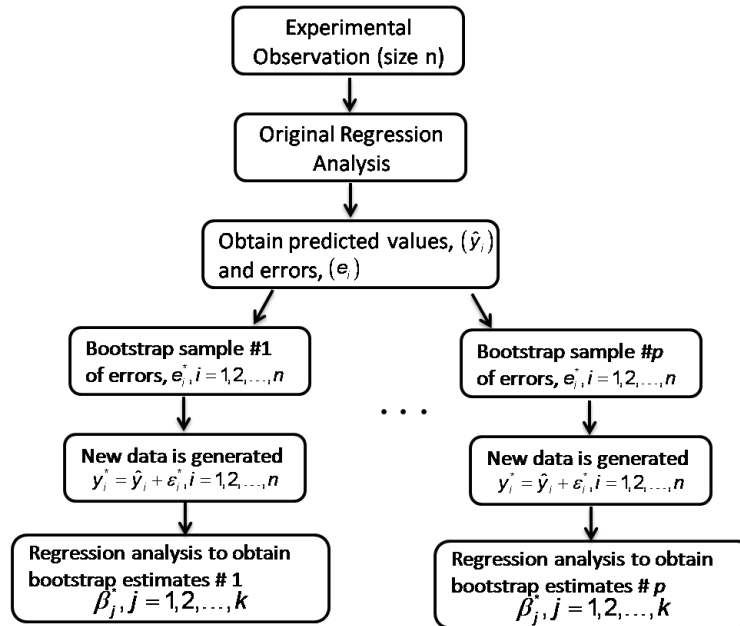


Figure 60: Fixed-x Bootstrap Procedure Flowchart

replacement. The size of the error vector is same as the number of observation, which is 16 in the demonstration example Table 23 shows an example of the bootstrap errors, fit from the original regression analysis, and the generated observation. The generated observation is obtained by adding the fit to the bootstrap errors. Comparing the bootstrap error column in Table 23 to the error column in Table 21, it can be seen that the errors 11.9, -2.1, 7.1, 0.1, and 10.2 from Table 21 did not appear in the bootstrap errors, while the errors, -1.0 and -21.5 appeared three times and the error 23.1 appeared twice.

Table 23: Bootstrap Error, Predicted Values, and Generated Observations for Fixed-x Bootstrap Method

| # | Bootstrap error (ϵ_i^*) | Predicted value (\hat{y}_i) | Generated observation ($y_i^* = \hat{y}_i + \epsilon_i^*$) |
|----|------------------------------------|---------------------------------|--|
| 1 | -12.1 | 2244.5 | 2232.4 |
| 2 | -1.0 | 2352.1 | 2351.1 |
| 3 | 11.5 | 2414.1 | 2425.6 |
| 4 | -20.5 | 2294.0 | 2273.5 |
| 5 | 25.4 | 2346.4 | 2371.8 |
| 6 | -4.1 | 2389.3 | 2385.2 |
| 7 | 23.1 | 2252.1 | 2275.2 |
| 8 | -21.3 | 2383.6 | 2362.3 |
| 9 | -1.0 | 2385.5 | 2384.5 |
| 10 | -16.4 | 2369.3 | 2352.9 |
| 11 | -21.5 | 2416.9 | 2395.4 |
| 12 | -1.0 | 2384.5 | 2383.5 |
| 13 | -21.5 | 2396.9 | 2375.4 |
| 14 | 23.1 | 2316.9 | 2340 |
| 15 | 9.7 | 2298.8 | 2308.5 |
| 16 | -21.5 | 2332.1 | 2310.6 |

The bootstrap estimates obtained from the newly generated data set using Equation 15 are $\hat{\beta}_0^* = 1633.34$, $\hat{\beta}_1^* = 7.0056$, and $\hat{\beta}_2^* = 7.19$. The procedure of generating bootstrap errors is repeated, and for every sample of the bootstrap estimate of the regression coefficients is obtained and saved. The procedure is repeated 3000 times to obtain the histograms of the bootstrap estimates. Figures 61, 62, and 63 show the bootstrap histograms of $\hat{\beta}_0^*$, $\hat{\beta}_1^*$, and $\hat{\beta}_2^*$ respectively.

The fixed-x resampling technique is used when the model-matrix $[X]$ is fixed. Efron [89] claims that the two approaches are asymptotically equivalent. The random-x method is less sensitive to assumptions concerning independence or error term. In this work, the fixed-x method is suitable because the model-matrix $[X]$ is fixed.

At the end of the input uncertainty quantification step, the covariance matrix $[\psi]$ between the regression estimates which represents the input uncertainty is obtained along with the estimates itself. The size of the covariance matrix is $k \times k$, where k is the number of regression estimates.

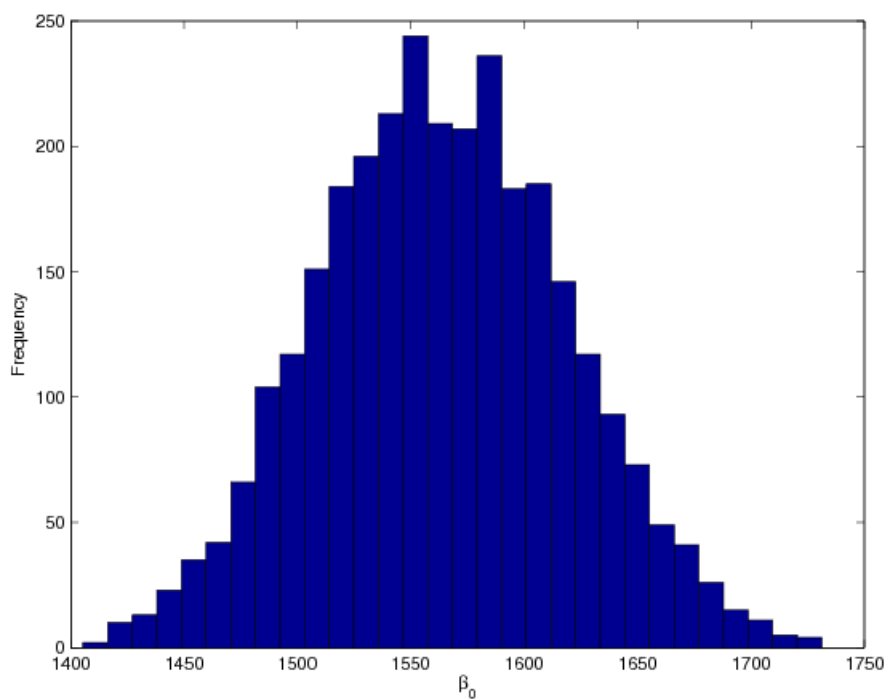


Figure 61: Fixed-x Bootstrap Histogram of $\hat{\beta}_0^*$ for the Demonstration Example

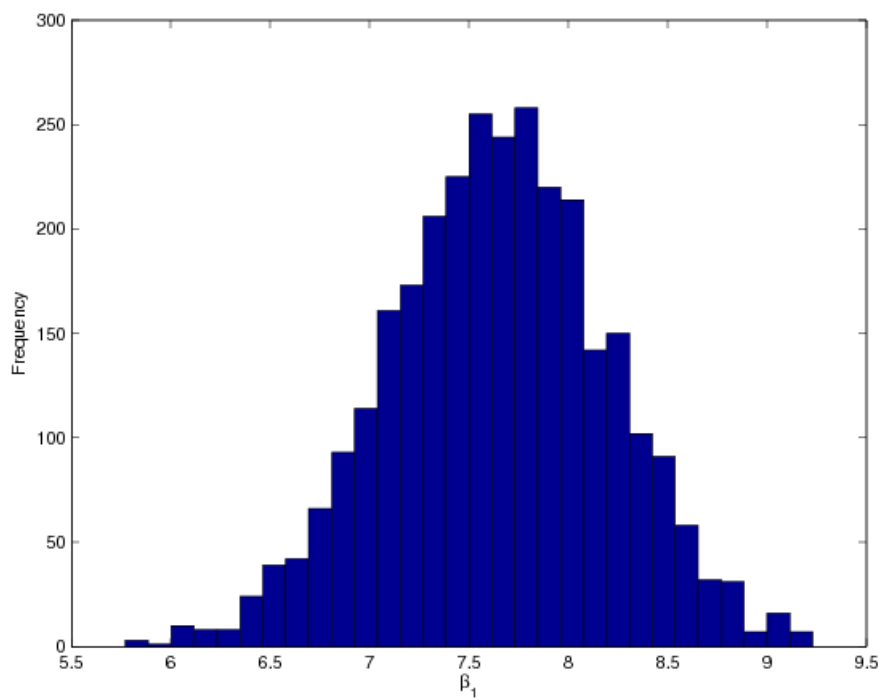


Figure 62: Fixed-x Bootstrap Histogram of $\hat{\beta}_1^*$ for the Demonstration Example

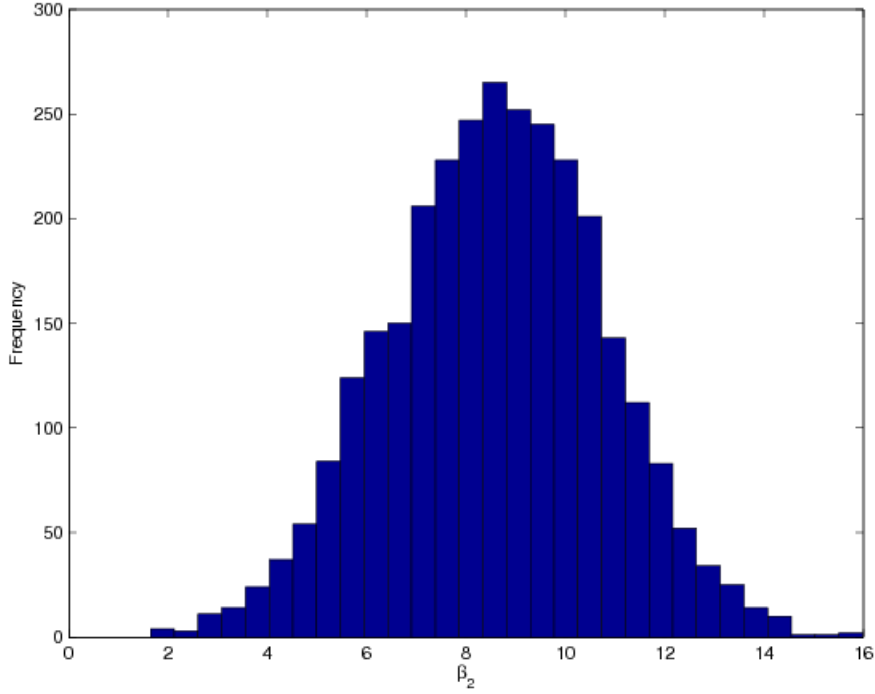


Figure 63: Fixed-x Bootstrap Histogram of $\hat{\beta}_2^*$ for the Demonstration Example

6.3.3 Uncertainty Propagation

Propagation of the uncertainty is needed to account its effect on the response. In a simulation-based environment such as FEA, polynomial chaos expansion or Taylor series expansion are used to approximate the response. This is performed to reduce the computational cost because there is no explicit relationship between the input and the response. A closed form equation is used to demonstrate the derivation procedure for the input uncertainty propagation before the black box (FEA) propagation is presented.

Closed Form Propagation

Consider a simple function f , that is a function of two parameters β_0 and β_1 . Assume $y = f(t; \hat{\beta}) = \hat{\beta}_0 + \hat{\beta}_1 t$, where t is the independent variable and $\hat{\beta}_0$ and $\hat{\beta}_1$ are unbiased estimates of true values. In analogy with the LP simulation, y can be considered as residual stress, $\hat{\beta}_0$ and $\hat{\beta}_1$ are model constant estimates and t is depth. The covariance function of response at two different depths t_1 and t_2 is derived:

$$\begin{aligned} Cov[y(t_1), y(t_2)] &= Cov\left[(\hat{\beta}_0 + \hat{\beta}_1 t_1), (\hat{\beta}_0 + \hat{\beta}_1 t_2)\right] \\ &= E\left\{\left[(\hat{\beta}_0 + \hat{\beta}_1 t_1) - (\beta_0 + \beta_1 t_1)\right]\left[(\hat{\beta}_0 + \hat{\beta}_1 t_2) - (\beta_0 + \beta_1 t_2)\right]\right\}, \text{ assuming } E\{\hat{\beta}_0\} = \beta_0 \text{ and } E\{\hat{\beta}_1\} = \beta_1 \end{aligned}$$

$$\begin{aligned}
&= E \left\{ \left[\left(\hat{\beta}_0 - \beta_0 \right) - \left(\hat{\beta}_1 - \beta_1 \right) t_1 \right] \left[\left(\hat{\beta}_0 - \beta_0 \right) - \left(\hat{\beta}_1 - \beta_1 \right) t_2 \right] \right\} \\
&= E \left[\left(\hat{\beta}_0 - \beta_0 \right)^2 \right] + E \left[\left(\hat{\beta}_0 - \beta_0 \right) \left(\hat{\beta}_1 - \beta_1 \right) \right] (t_1 + t_2) + E \left[\left(\hat{\beta}_1 - \beta_1 \right)^2 \right] (t_1 t_2) \\
&= \hat{\sigma}_{00} + \hat{\sigma}_{01} (t_1 + t_2) + \hat{\sigma}_{11} (t_1 t_2)
\end{aligned}$$

where $\hat{\sigma}_{00}$ is the estimate of variance of $\hat{\beta}_0$, $\hat{\sigma}_{11}$ is the estimate of variance of $\hat{\beta}_1$ and $\hat{\sigma}_{01}$ is the estimate of covariance between $\hat{\beta}_0$ and $\hat{\beta}_1$. $E(\bullet)$ stands for expected value. The above equation can be written in matrix form:

$$Cov \begin{bmatrix} y(t_1) \\ y(t_2) \end{bmatrix} = \begin{bmatrix} Var[y(t_1)] & Cov[y(t_1), y(t_2)] \\ Cov[y(t_2), y(t_1)] & Var[y(t_2)] \end{bmatrix}$$

where Var stands for variance of a variable and Cov stands for covariance of a variable. Substituting for the covariance as derived above and using the property of variance as self covariance:

$$Cov \begin{bmatrix} y(t_1) \\ y(t_2) \end{bmatrix} = \begin{bmatrix} \hat{\sigma}_{00} + 2t_1 \hat{\sigma}_{01} + t_1^2 \hat{\sigma}_{11} & \hat{\sigma}_{00} + \hat{\sigma}_{01} (t_1 + t_2) + \hat{\sigma}_{11} (t_1 t_2) \\ \hat{\sigma}_{00} + \hat{\sigma}_{01} (t_1 + t_2) + \hat{\sigma}_{11} (t_1 t_2) & \hat{\sigma}_{00} + 2t_2 \hat{\sigma}_{01} + t_2^2 \hat{\sigma}_{11} \end{bmatrix} \quad (26)$$

The matrix shown in Equation 26 is decomposed into three matrices as: gradient matrix, input covariance matrix, and transpose of gradient matrix as follows:

$$Cov \begin{bmatrix} y(t_1) \\ y(t_2) \end{bmatrix} = \begin{bmatrix} \hat{\sigma}_{00} + t_1 \hat{\sigma}_{01} & \hat{\sigma}_{01} + t_1 \hat{\sigma}_{11} \\ \hat{\sigma}_{01} + t_2 \hat{\sigma}_{11} & \hat{\sigma}_{01} + t_2 \hat{\sigma}_{11} \end{bmatrix} \begin{bmatrix} 1 & 1 \\ t_1 & t_2 \end{bmatrix} \quad (27)$$

$$Cov \begin{bmatrix} y(t_1) \\ y(t_2) \end{bmatrix} = \begin{bmatrix} 1 & t_1 \\ 1 & t_2 \end{bmatrix} \begin{bmatrix} \hat{\sigma}_{00} & \hat{\sigma}_{01} \\ \hat{\sigma}_{01} & \hat{\sigma}_{11} \end{bmatrix} \begin{bmatrix} 1 & 1 \\ t_1 & t_2 \end{bmatrix} \quad (28)$$

The matrix shown in Equation 28 can be written as a gradient matrix, input covariance matrix, and transpose of the gradient matrix as shown in Equation 29:

$$Cov \begin{bmatrix} y(t_1) \\ y(t_2) \end{bmatrix} = \begin{bmatrix} \frac{\partial f(t_1)}{\partial \hat{\beta}_0} & \frac{\partial f(t_1)}{\partial \hat{\beta}_1} \\ \frac{\partial f(t_2)}{\partial \hat{\beta}_0} & \frac{\partial f(t_2)}{\partial \hat{\beta}_1} \end{bmatrix} \begin{bmatrix} \hat{\sigma}_{00} & \hat{\sigma}_{01} \\ \hat{\sigma}_{01} & \hat{\sigma}_{11} \end{bmatrix} \begin{bmatrix} \frac{\partial f(t_1)}{\partial \hat{\beta}_0} & \frac{\partial f(t_2)}{\partial \hat{\beta}_0} \\ \frac{\partial f(t_1)}{\partial \hat{\beta}_1} & \frac{\partial f(t_2)}{\partial \hat{\beta}_1} \end{bmatrix} \quad (29)$$

$$Cov \begin{bmatrix} y(t_1) \\ y(t_2) \end{bmatrix} = [F] [\psi] [F^T] \quad (30)$$

where $[F]$ is a matrix of partial derivatives of parameter estimates at two different depths t_1 and t_2 , and $[\psi]$ is the covariance matrix of the estimates of regression coefficients obtained from the non-linear regression analysis. The term $\left[\frac{\partial f(t_1)}{\partial \hat{\beta}_0} \right]$ is the gradient of f with respect to $\hat{\beta}_0$ at a depth t_1 . The covariance matrix of the response is obtained by propagating the input uncertainty. The derivation shown in this section is valid for a linear relationship between input and output.

Black Box Propagation

In the above demonstration example, the relationship between random input parameters $\underline{\hat{\beta}}$ and the response y is known. In a simulation-based environment, such as FEA, the function f is a black box. First order Taylor series expansion is used to approximate the response. At any depth t , the residual stress can be approximated as shown in Equation 31:

$$f(t; \underline{\hat{\beta}}) \cong f(t; \underline{\beta}) + \left[\frac{\partial f(t)}{\partial \underline{\beta}} \right]_{\underline{\beta}=\underline{\hat{\beta}}}^T (\underline{\hat{\beta}} - \underline{\beta}) \quad (31)$$

where $\underline{\hat{\beta}}$ represents the estimates of material model constants $\underline{\beta}$. $\left[\frac{\partial f(t)}{\partial \underline{\beta}} \right]_{\underline{\beta}=\underline{\hat{\beta}}}^T$ is a vector representing the gradient of residual stress w. r. t. all the regression coefficients at any depth t evaluated at the regression estimates obtained. The definition of covariance of residual stresses between two different depths t_1 and t_2 is shown in Equation 32:

$$Cov \left[f(t_1, \underline{\hat{\beta}}), f(t_2, \underline{\hat{\beta}}) \right] = E \left\{ \left[f(t_1, \underline{\hat{\beta}}) - f(t_1, \underline{\beta}) \right] \left[f(t_2, \underline{\hat{\beta}}) - f(t_2, \underline{\beta}) \right] \right\} \quad (32)$$

Substituting the Taylor series approximation assumed in Equation 31 in the Equation 32, we obtain:

$$\cong E \left\{ \left[\left[\frac{\partial f(t_1)}{\partial \underline{\beta}} \right]_{\underline{\beta}=\underline{\hat{\beta}}}^T (\underline{\hat{\beta}} - \underline{\beta}) \right] \left[\left[\frac{\partial f(t_2)}{\partial \underline{\beta}} \right]_{\underline{\beta}=\underline{\hat{\beta}}}^T (\underline{\hat{\beta}} - \underline{\beta}) \right]^T \right\} \quad (33)$$

Rearranging the terms in Equation 33, we obtain:

$$\cong E \left\{ \left[\left[\frac{\partial f(t_1)}{\partial \underline{\beta}} \right]_{\underline{\beta}=\underline{\hat{\beta}}}^T (\underline{\hat{\beta}} - \underline{\beta}) (\underline{\hat{\beta}} - \underline{\beta})^T \left[\frac{\partial f(t_2)}{\partial \underline{\beta}} \right]_{\underline{\beta}=\underline{\hat{\beta}}} \right] \right\} \quad (34)$$

The gradient matrix and its transpose shown in Equation 34 are not random but fixed numbers. Therefore Equation 34 is simplified as shown in Equation 35:

$$\cong \left[\frac{\partial f(t_1)}{\partial \underline{\beta}} \right]_{\underline{\beta}=\underline{\hat{\beta}}}^T E \left\{ \left[(\underline{\hat{\beta}} - \underline{\hat{\beta}}) (\underline{\hat{\beta}} - \underline{\hat{\beta}})^T \right] \right\} \left[\frac{\partial f(t_2)}{\partial \underline{\beta}} \right]_{\underline{\beta}=\underline{\hat{\beta}}} \quad (35)$$

The expected value of the random term shown in Equation 35 is by definition the covariance matrix of the regression estimates that is obtained from the regression analysis. It is defined as shown in 30 as $[\psi]$. Substituting $[\psi]$ in Equation 35, we obtain:

$$\cong \left[\frac{\partial f(t_1)}{\partial \underline{\beta}} \right]_{\underline{\beta}=\underline{\hat{\beta}}}^T [\psi] \left[\frac{\partial f(t_1)}{\partial \underline{\beta}} \right]_{\underline{\beta}=\underline{\hat{\beta}}} \quad (36)$$

$\left[\frac{\partial f(t_1)}{\partial \underline{\beta}}\right]_{\underline{\beta}=\hat{\underline{\beta}}}^T$ is the partial derivative of residual stress at depth t_1 with respect to estimates of model constants. For the sake of simplicity the subscript $\underline{\beta} = \hat{\underline{\beta}}$ is not included in rest of the document. $[\psi]$ is a symmetric matrix with variance on diagonal terms and covariance on off diagonal terms. The number of discrete depths that are considered depends on the finite element (FE) model mesh. Let m be the number of nodes in the FE model. The covariance of residual stress field at each depth is obtained as follows:

$$Cov \begin{bmatrix} f(t_1; \hat{\underline{\beta}}) \\ f(t_2; \hat{\underline{\beta}}) \\ \vdots \\ f(t_m; \hat{\underline{\beta}}) \end{bmatrix} = \begin{bmatrix} V[f(t_1, \hat{\underline{\beta}})] & C[f(t_1, \hat{\underline{\beta}}), (t_2, \hat{\underline{\beta}})] & \cdots & C[f(t_1, \hat{\underline{\beta}}), (t_m, \hat{\underline{\beta}})] \\ C[f(t_2, \hat{\underline{\beta}}), (t_1, \hat{\underline{\beta}})] & V[f(t_2, \hat{\underline{\beta}})] & \cdots & C[f(t_2, \hat{\underline{\beta}}), (t_m, \hat{\underline{\beta}})] \\ \vdots & \vdots & \ddots & \vdots \\ C[f(t_m, \hat{\underline{\beta}}), (t_1, \hat{\underline{\beta}})] & C[f(t_m, \hat{\underline{\beta}}), (t_2, \hat{\underline{\beta}})] & \cdots & V[f(t_m, \hat{\underline{\beta}})] \end{bmatrix}$$

where $V[\bullet]$ and $C[\bullet]$ represent the variance and covariance of a variable respectively. The size of the matrix is $m \times m$, with variance of residual stress at each depth on diagonal terms and covariance between depths on the off diagonal terms. Substituting the covariance between two depths that has been derived before, we obtain:

$$\approx \begin{bmatrix} \left[\frac{\partial f(t_1)}{\partial \underline{\beta}}\right]^T \psi \left[\frac{\partial f(t_1)}{\partial \underline{\beta}}\right] & \left[\frac{\partial f(t_1)}{\partial \underline{\beta}}\right]^T \psi \left[\frac{\partial f(t_2)}{\partial \underline{\beta}}\right] & \cdots & \left[\frac{\partial f(t_1)}{\partial \underline{\beta}}\right]^T \psi \left[\frac{\partial f(t_m)}{\partial \underline{\beta}}\right] \\ \left[\frac{\partial f(t_2)}{\partial \underline{\beta}}\right]^T \psi \left[\frac{\partial f(t_1)}{\partial \underline{\beta}}\right] & \left[\frac{\partial f(t_2)}{\partial \underline{\beta}}\right]^T \psi \left[\frac{\partial f(t_2)}{\partial \underline{\beta}}\right] & \cdots & \left[\frac{\partial f(t_2)}{\partial \underline{\beta}}\right]^T \psi \left[\frac{\partial f(t_m)}{\partial \underline{\beta}}\right] \\ \vdots & \vdots & \ddots & \vdots \\ \left[\frac{\partial f(t_m)}{\partial \underline{\beta}}\right]^T \psi \left[\frac{\partial f(t_1)}{\partial \underline{\beta}}\right] & \left[\frac{\partial f(t_m)}{\partial \underline{\beta}}\right]^T \psi \left[\frac{\partial f(t_2)}{\partial \underline{\beta}}\right] & \cdots & \left[\frac{\partial f(t_m)}{\partial \underline{\beta}}\right]^T \psi \left[\frac{\partial f(t_m)}{\partial \underline{\beta}}\right] \end{bmatrix}_{m \times m} \quad (37)$$

The above matrix can be simplified by separating the common terms and the resultant matrices obtained are:

$$= \begin{bmatrix} \left[\frac{\partial f(t_1)}{\partial \underline{\beta}}\right]^T \\ \left[\frac{\partial f(t_2)}{\partial \underline{\beta}}\right]^T \\ \vdots \\ \left[\frac{\partial f(t_m)}{\partial \underline{\beta}}\right]^T \end{bmatrix}_{m \times k} [\psi]_{k \times k} \begin{bmatrix} \left[\frac{\partial f(t_1)}{\partial \underline{\beta}}\right]_{k \times 1} & \left[\frac{\partial f(t_2)}{\partial \underline{\beta}}\right]_{k \times 1} & \cdots & \left[\frac{\partial f(t_m)}{\partial \underline{\beta}}\right]_{k \times 1} \end{bmatrix}_{k \times m} = [F^T] [\psi] [F]$$

where $[F]$ is the sensitivity matrix of the residual stress with respect to estimates of material model constants. Each column of $[F]$ is the gradient of residual stress with respect to a material model constant estimate along the depth. The obtained covariance matrix of residual stress represents the uncertainty in the residual stress field due to uncertainty in the model constant estimator. Central difference scheme is used to determine the gradients of residual stress at each depth with respect to estimates of regression coefficients or model constants. The step size for each gradient is obtained after a convergence study. The number of additional FE simulations

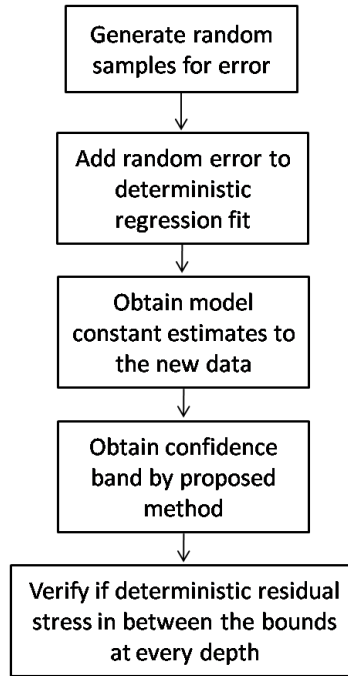


Figure 64: Confidence Band Validation Procedure

needed using the central difference scheme depends on the number of regression coefficient estimates. For k estimates, $2k$ additional FE simulations are required.

6.3.4 Residual Stress Field Confidence Band

The diagonal elements of the covariance matrix obtained in the previous section contain the variance of the residual stress at each depth. Approximate 95% lower and upper bound of residual stress at each depth can be obtained from Equation 38

$$\begin{aligned} \text{Upper Bound} &= RS_i + 1.96\sigma_i \\ \text{Lower Bound} &= RS_i - 1.96\sigma_i \end{aligned} \quad (38)$$

where RS_i is the residual stress obtained from the deterministic analysis at a depth i and σ_i is the standard deviation at a depth i . The index i ranges from 0 (surface) to a depth of interest. The number 1.96 represents the 95% bounds for normal distribution. The upper and lower confidence band for the entire depth is obtained by interpolating the upper and lower confidence bounds respectively. The confidence band implies that the true residual stress field will be between the confidence band 95% of the times.

Validation of Confidence Band

A Monte Carlo analysis is performed to demonstrate the validation of the confidence band developed. Figure 64 shows the flow chart of the validation procedure. Random samples of error are generated from a normal distribution with a zero mean and a variance of mean squared error obtained from the non-linear regression analysis. The deterministic fit is added to the random

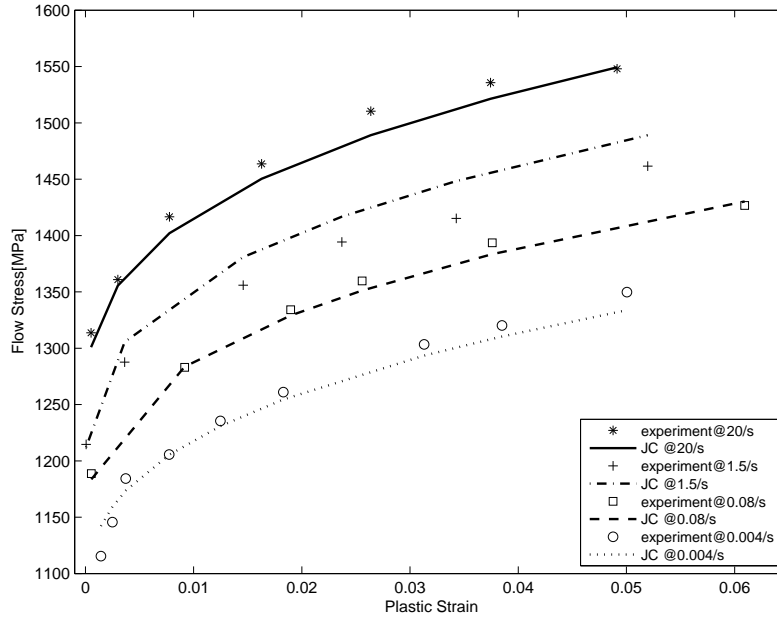


Figure 65: JC Model Fit to the Experimental Data

error. New estimates of model constants are obtained from non-linear regression analysis. The developed methodology is used to obtain the confidence band for the entire depth of interest for the new simulated experimental data. The deterministic residual stress is verified at each depth and if the stress lies in between the confidence bounds, a counter is prepared. This procedure is repeated several times and the counter is updated each time the deterministic residual stress is in between the confidence bounds. The counter at each depth can be used to approximate the true confidence level. A plot of obtained confidence level vs. depth is prepared to compare with the target level.

6.4 Regression (Input) Uncertainty Quantification Results

Experimental data [75] of material behavior for Ti-6Al-4V at four different strain rates are shown in Figure 65. This figure shows the plot of flow stress vs. plastic strain. The experiments have been performed using the Hopkinson bar test, details can be found in the cited reference. The JC model is used to curve fit the available experimental data and will later be used to predict the material behavior at higher strain rates. The JC model details are provided in Chapter 3 and is shown in Equation 39 for continuity. Figure 65 shows that the JC model was able to match the experimental data at three strain rates of $20s^{-1}$, $1.5s^{-1}$, and $0.04s^{-1}$ relatively well compared to strain rate of $1.5s^{-1}$. Model constants A , B , n , and C are estimated using non-linear regression analysis. $\dot{\epsilon}_0$ is assumed to be equal to $1s^{-1}$.

$$\sigma = [A + B\epsilon^n] \left[1 + C \ln \frac{\dot{\epsilon}}{\dot{\epsilon}_0} \right] \quad (39)$$

Figure 66 shows another representation of the fit to the experimental data. Comparison between actual values vs. predicted values are plotted at different actual values. A plot of straight line with

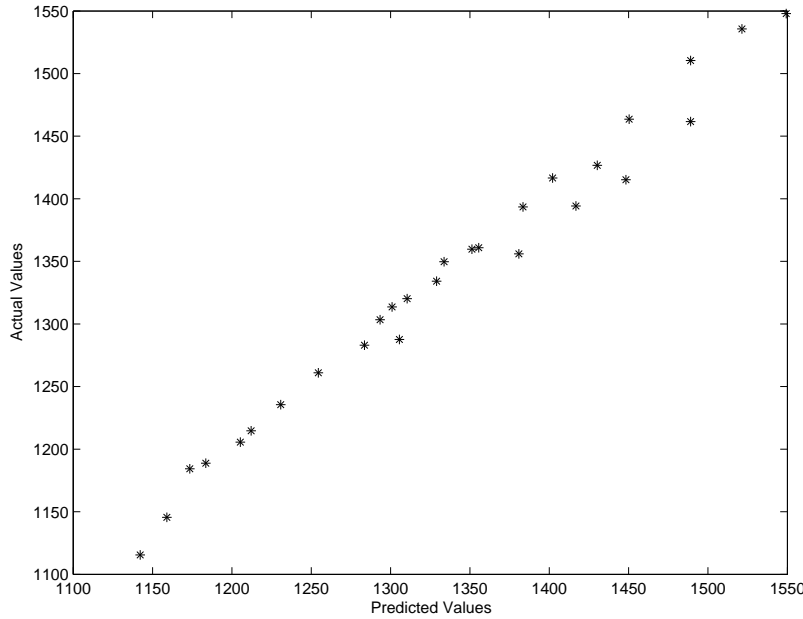


Figure 66: JC Model Fit vs Actual Experimental Data

45° angle represents a good fit with the experimental data at all predicted values. Figure 66 shows a straight line with better fit to the experimental data at lower predicted values compared to higher. Two assumptions of random errors: (i) constant variance and (ii) zero mean can be checked at the same time using the residual plot. A residual plot is a plot of residuals against the fitted values. If both the assumptions are satisfied the scatter is expected to vary randomly around zero for all predicted values. Figure 67 shows the residual plot for the JC model from the non-linear regression analysis. The figure shows that both the assumptions were satisfied for all predicted values.

The model constant estimates obtained are shown in Table 24.

Table 24: Material Model Constant Estimates

| Model Constant Estimates | Value |
|--------------------------|-------------|
| <i>A</i> | 1170.07 MPa |
| <i>B</i> | 837.34 MPa |
| <i>n</i> | 0.3409 |
| <i>C</i> | 0.017 |

An estimate of the covariance matrix for the model constant estimates is obtained from the

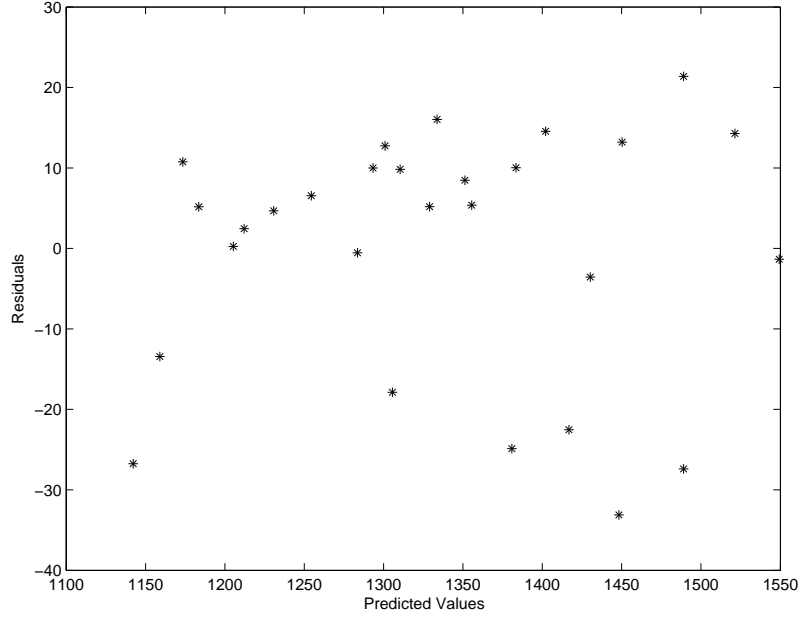


Figure 67: JC Model Fit vs Residuals

non-linear regression analysis using Equation 20 and is shown in Equation 40:

$$[\psi] = \begin{bmatrix} \hat{A} & \hat{B} & \hat{n} & \hat{C} \\ \hat{A} & 5.72 \times 10^2 & 1.51 \times 10^3 & 1.18 & -8.82 \times 10^{-4} \\ \hat{B} & & 7.10 \times 10^3 & 4.08 & -4.83 \times 10^{-3} \\ \hat{n} & & & 2.75 \times 10^{-3} & -3.58 \times 10^{-6} \\ \hat{C} & Sym & & & 4.29 \times 10^{-7} \end{bmatrix} \quad (40)$$

The variance of the model constant estimates are along the diagonals. The off-diagonal terms represent the covariance between model constant estimates. A correlation coefficient matrix is obtained to provide a better interpretation of the covariance matrix because the model constants are on different scales. Equation 41 shows the formula to obtain the correlation coefficient between two random variables, X and Y :

$$corr[X, Y] = \frac{cov[X, Y]}{\sqrt{Var[X]} \sqrt{Var[Y]}} \quad (41)$$

where $cov[X, Y]$ is the covariance between X and Y and $Var[\bullet]$ represents variance of a variable. Equation 42 shows the calculated correlation coefficient matrix:

$$[corr] = \begin{bmatrix} \hat{A} & \hat{B} & \hat{n} & \hat{C} \\ \hat{A} & 1 & 0.75 & 0.94 & -0.06 \\ \hat{B} & & 1 & 0.92 & -0.09 \\ \hat{n} & & & 1 & -0.1 \\ \hat{C} & Sym & & & 1 \end{bmatrix} \quad (42)$$

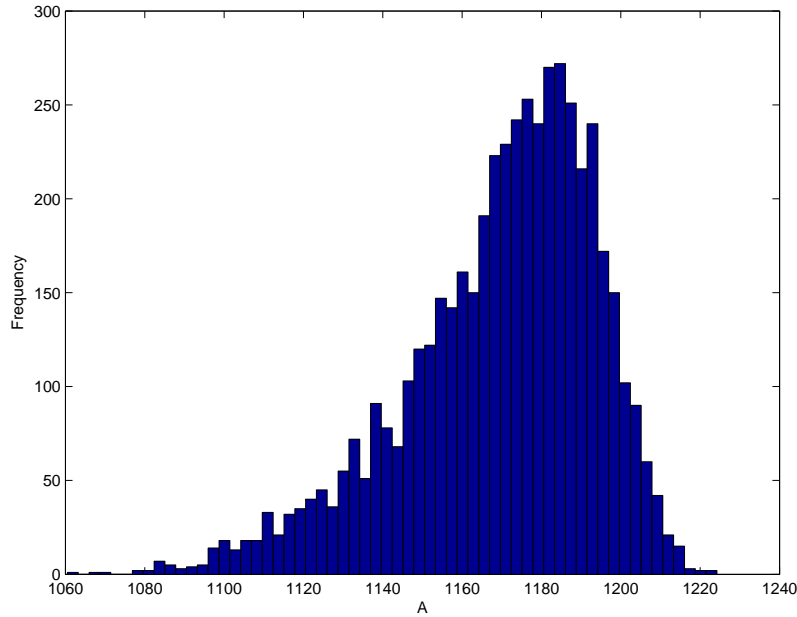


Figure 68: Bootstrap Histogram of \hat{A}

Equation 42 indicates that the estimate of model constant \hat{C} is negatively correlated with other estimates and also these correlations are low. Model constant estimate \hat{n} is highly correlated with estimates \hat{A} and \hat{B} .

Fixed-x bootstrap sampling technique is performed to evaluate the multivariate normality assumption of the model constant estimates. Figures 68, 69, 70, and 71 show the bootstrap histograms of the estimates \hat{A} , \hat{B} , \hat{C} , and \hat{n} . 5000 bootstrap estimates are obtained. It can be seen from these figures that the model constant estimates \hat{n} and \hat{C} are approximately normal while the estimates \hat{A} and \hat{B} are skewed. The bootstrap method provides a qualitative validation on the multi-variate normality assumption that the model constant estimates closely resemble the assumed distribution.

6.5 Demonstration Examples and LP Application

The input uncertainty quantified in the previous section is propagated through closed-form demonstration examples and the LP application to obtain the confidence band. Two demonstration examples are investigated. For these demonstration examples, an explicit relationship between the residual stress and the model constant estimate is assumed such that the residual stress field obtained is similar to the residual stress field generated by the LP application. Monte Carlo analysis is performed for the demonstration examples to validate the confidence band.

6.5.1 Demonstration Example 1

The relationship between the residual stress field and the model constant estimates is shown in Equation 43.

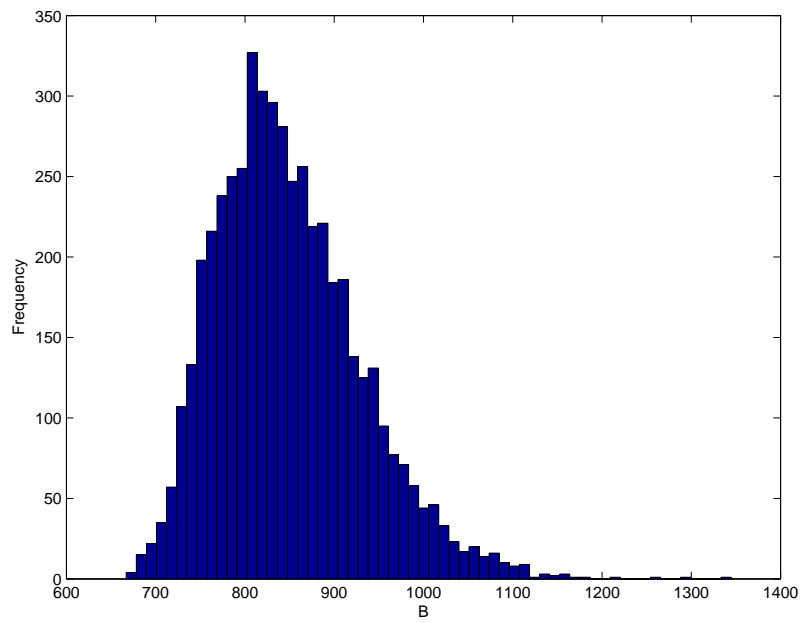


Figure 69: Bootstrap Histogram of \hat{B}

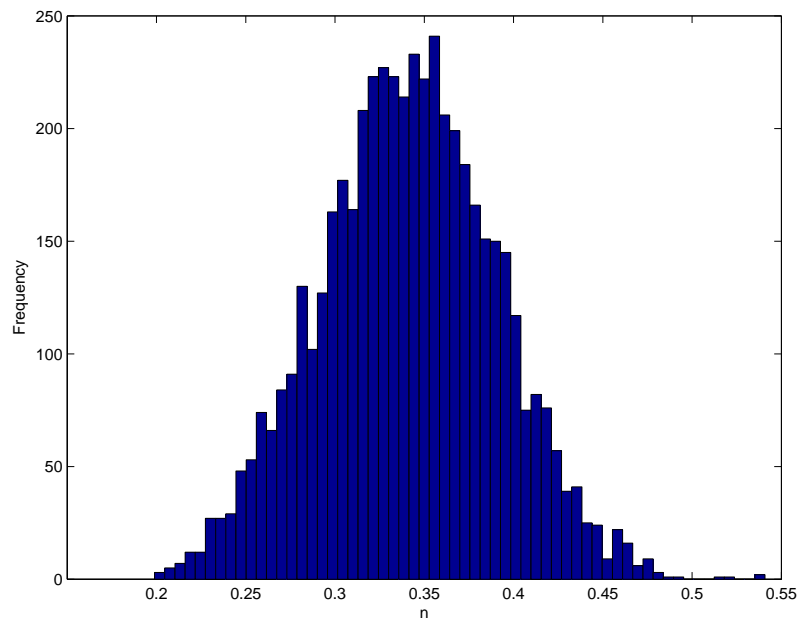


Figure 70: Bootstrap Histogram of \hat{n}

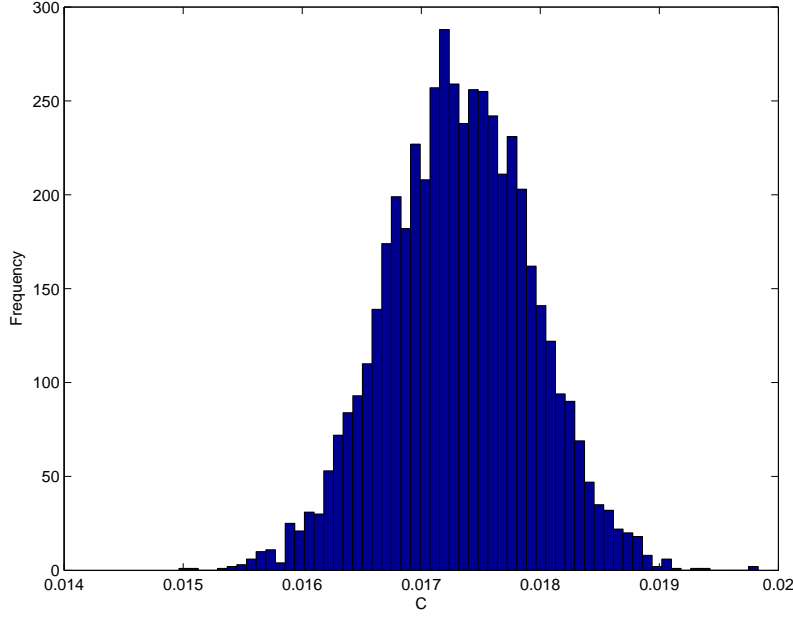


Figure 71: Bootstrap Histogram of \hat{C}

$$RS = -1000 + 1000 \log(A + 20Bd + nd^2 + Cd^3) \quad (43)$$

where RS is the residual stress value, d is the depth in mm , and A , B , n , and C are the model constants. Equation 43 indicates a logarithmic relationship between the residual stress field at any depth d and the model constants. The estimates obtained in Table 24 are used to obtain the deterministic residual stress field. A depth of 2 mm is considered and 80 equal divisions are assumed representing the discretization (FEA mesh) of the depth. Figure 72 shows the deterministic residual stress field. As we can see from the figure, the residual stress field is compressive at the surface and progressively leads to tensile at sub surface which is similar to the laser peened residual stress field. The closed form equation is a representative of the residual stress field obtained from the LP simulation.

A central difference scheme is used to obtain the numerical gradient of the residual stress field with respect to each model constant estimate. A comparison is made with the analytical gradients because the explicit relationship between the residual stress field and the model constants is known. Figures 73, 74, 75, and 76 show the comparison between analytical and numerical gradient of residual stress field for model constant estimates \hat{A} , \hat{B} , \hat{n} , and \hat{C} respectively.

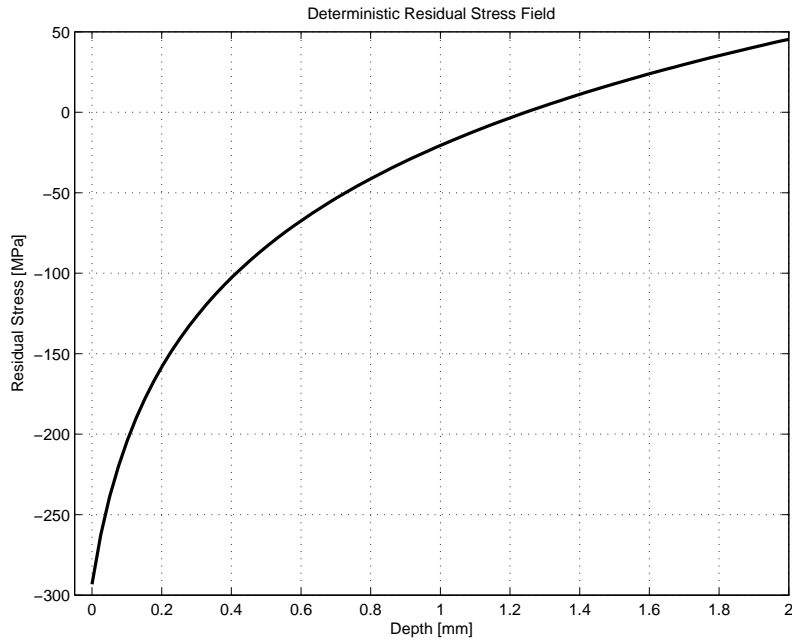


Figure 72: Deterministic Residual Stress Field for Demonstration Problem 1

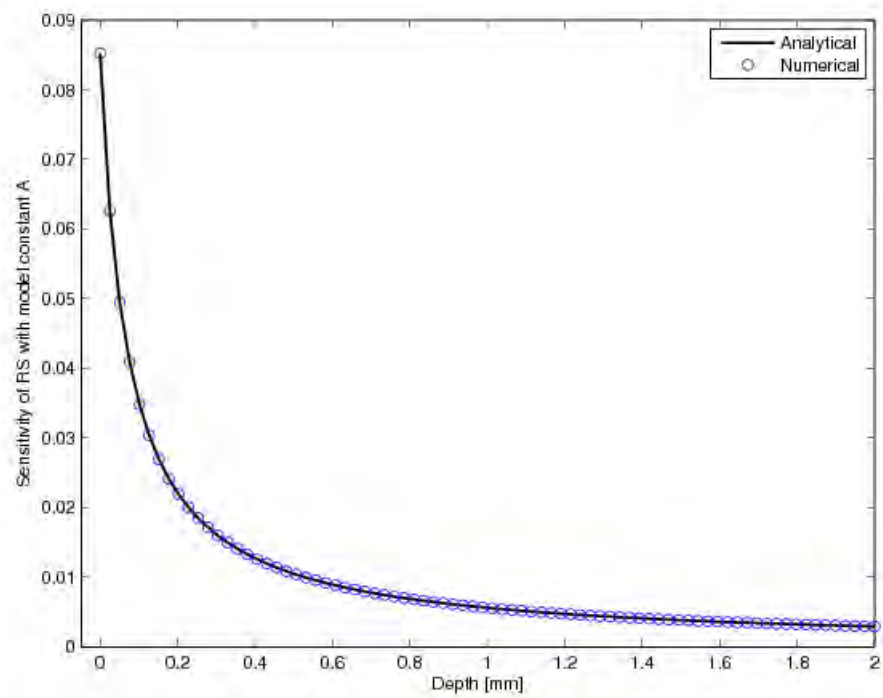


Figure 73: Gradient of Residual Stress Field with respect to Model Constant Estimate \hat{A} for Demonstration Problem 1

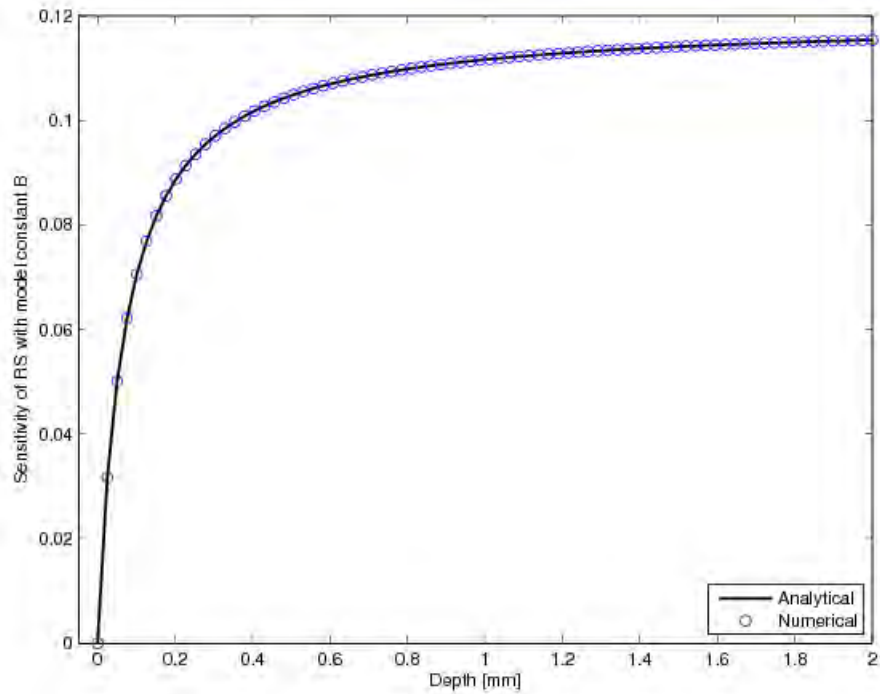


Figure 74: Gradient of Residual Stress Field with respect to Model Constant Estimate \hat{B} for Demonstration Problem 1

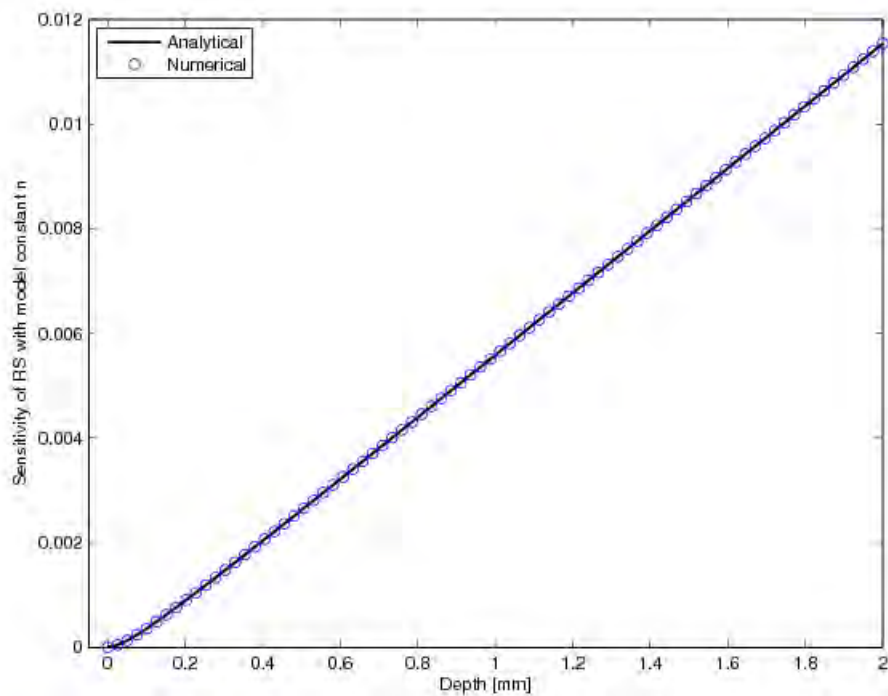


Figure 75: Gradient of Residual Stress Field with respect to Model Constant Estimate \hat{n} for Demonstration Problem 1

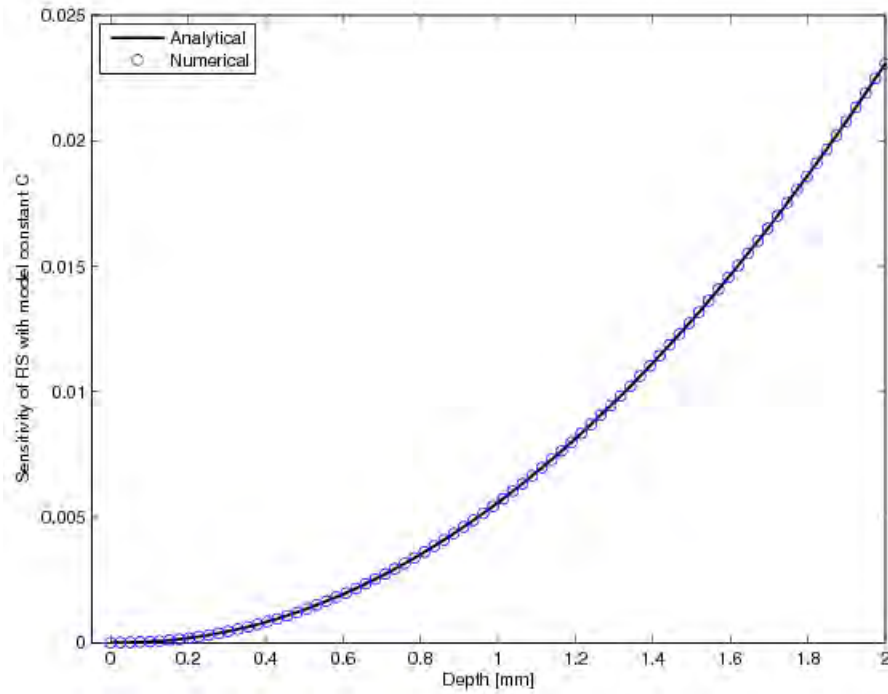


Figure 76: Gradient of Residual Stress Field with respect to Model Constant Estimate \hat{C} for Demonstration Problem 1

A good agreement between the numerical and analytical gradient is evident from the figures. Increasing trend can be seen for the model constant estimates \hat{B} , \hat{C} , and \hat{n} , while decreasing trend is evident for \hat{A} . The covariance matrix of the residual stress is obtained from the procedure described in Section . Figure 77 shows the 95% confidence band on the residual stress field along with the deterministic residual stress field.

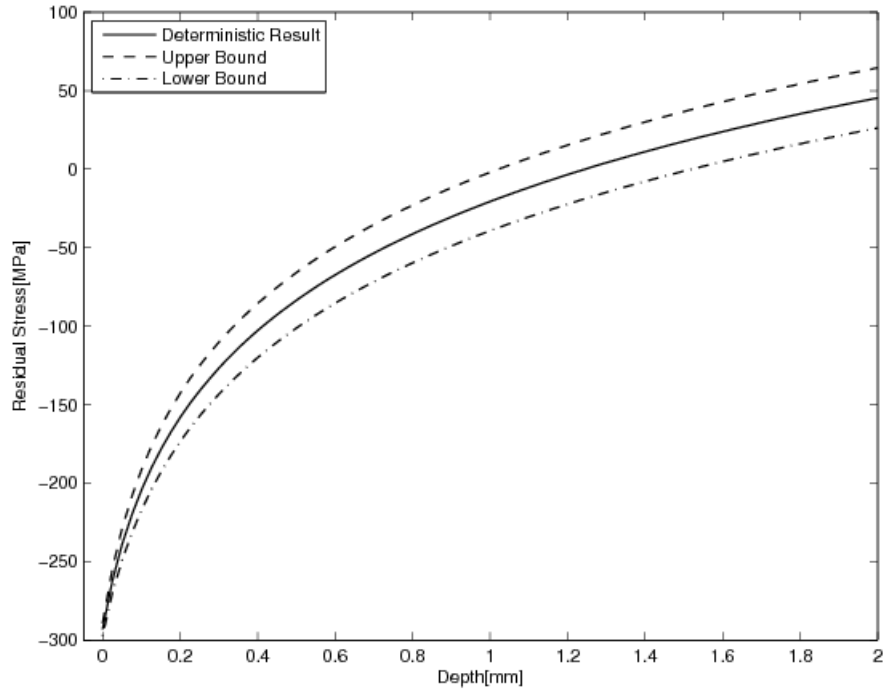


Figure 77: 95% Confidence Band on the Residual Stress Field for Demonstration Problem 1

The confidence band indicates that the true residual stress field is in between the band 95% of the times. A plot of standard deviation of the residual stress along the depth is shown in Figure 78.

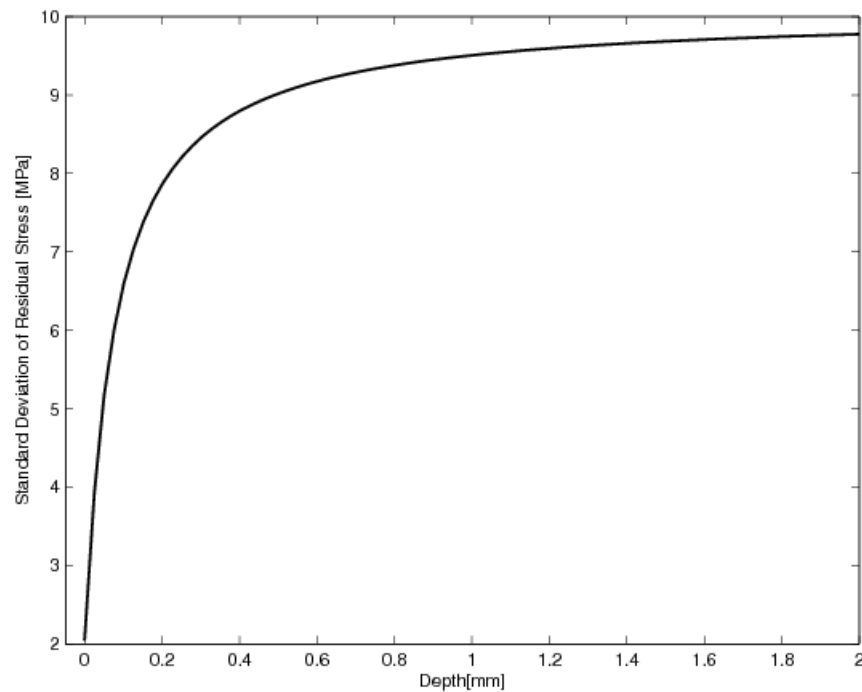


Figure 78: Standard Deviation of Residual Stress Field for Demonstration Problem 1

A lower value of standard deviation can be seen at the surface and progressively increases along the depth. The smallest variability of 2 MPa is observed at the surface while a maximum variability of 10 MPa can be seen at a depth of 2 mm.

A MCS on Equation 43 is performed to validate the developed residual stress band. Figure 79 shows the comparison between the target and achieved confidence level for the million Monte Carlo samples along the entire depth.

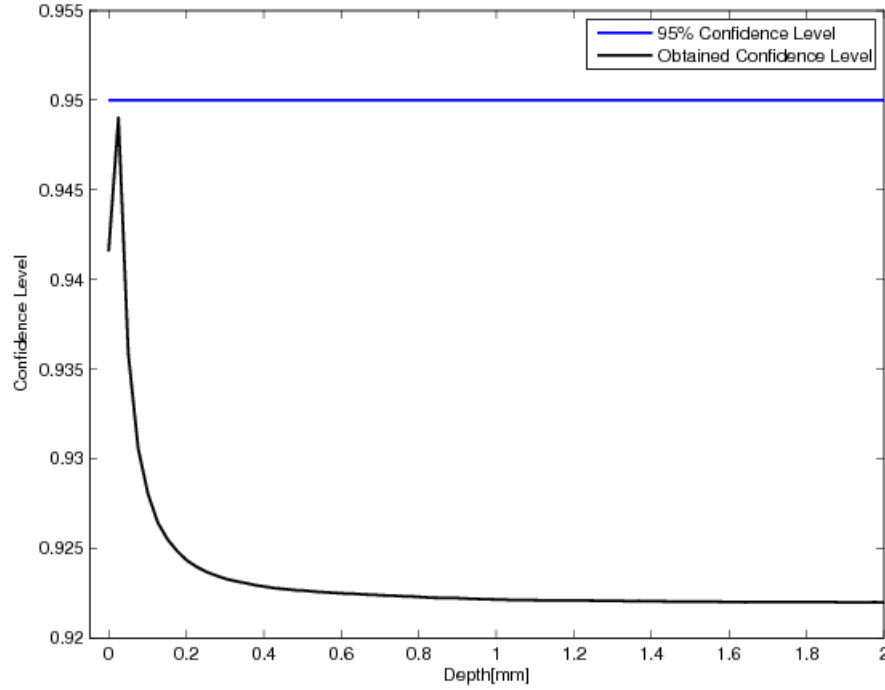


Figure 79: Confidence Level Comparison to Target Confidence Level for Demonstration Problem 1

A lowest confidence level of $\approx 92\%$ is achieved at the sub surface and a highest confidence of $\approx 95\%$ at near surface. Figure 79 indicates that the developed confidence bands are able to capture the target confidence levels with reasonable accuracy.

6.5.2 Demonstration Example 2

A response surface fit is chosen as the second demonstration example. The response surface is shown in Equation 44

$$RS = \alpha_1 + \alpha_2 A d^{\alpha_3} + \alpha_4 B d^{\alpha_5} + \alpha_6 n d^{\alpha_7} + \alpha_8 C d^{\alpha_9} \quad (44)$$

where α_i , $i = 1, 2, \dots, 9$ need to be determined. The second demonstration example represents a polynomial relationship between the residual stress field and the model constant estimates as opposed to logarithmic relationship in the demonstration example 1. Also, the response surface is a representative of the residual stress field induced by the LP process. 21 latin hypercube samples are generated using JUMP software and the design matrix is shown in Table 25. Upper and lower

bounds for each model constant estimate is provided. The design matrix is generated such that the samples are generated from the entire design space. FEA is performed at all the 21 design points and the residual stress values are obtained. The first 20 samples are used to obtain the coefficients and the 21st design point is used to compare the response surface fit and the FEA result.

Table 25: Latin Hypercube Samples Design Matrix

| # | <i>A</i> | <i>B</i> | <i>n</i> | <i>C</i> | <i>d</i> |
|----|----------|----------|----------|----------|----------|
| 1 | 1168.3 | 862.59 | 0.3881 | 0.0174 | 0.3 |
| 2 | 1180.2 | 921.58 | 0.3723 | 0.0178 | 1.4 |
| 3 | 1189.8 | 803.6 | 0.3776 | 0.0168 | 0.6 |
| 4 | 1173.1 | 837.31 | 0.3933 | 0.0173 | 1.7 |
| 5 | 1185.0 | 904.73 | 0.2989 | 0.0177 | 0.8 |
| 6 | 1177.8 | 786.74 | 0.3199 | 0.0178 | 1.1 |
| 7 | 1151.5 | 761.46 | 0.3304 | 0.0172 | 1.3 |
| 8 | 1175.4 | 795.17 | 0.2884 | 0.0171 | 1.6 |
| 9 | 1187.4 | 913.15 | 0.3566 | 0.0169 | 1.5 |
| 10 | 1161.1 | 769.89 | 0.3618 | 0.0169 | 0.2 |
| 11 | 1163.4 | 845.73 | 0.3356 | 0.0167 | 2.0 |
| 12 | 1170.7 | 753.03 | 0.3828 | 0.0177 | 0.5 |
| 13 | 1156.3 | 871.02 | 0.2936 | 0.0174 | 1.9 |
| 14 | 1192.2 | 879.44 | 0.3409 | 0.0171 | 0.0 |
| 15 | 1165.9 | 887.87 | 0.3146 | 0.017 | 0.7 |
| 16 | 1153.9 | 812.02 | 0.3461 | 0.0179 | 1.8 |
| 17 | 1158.7 | 820.45 | 0.3251 | 0.0176 | 0.1 |
| 18 | 1194.6 | 854.16 | 0.3041 | 0.0168 | 1.0 |
| 19 | 1182.6 | 778.31 | 0.3094 | 0.0172 | 0.4 |
| 20 | 1149.1 | 896.3 | 0.3513 | 0.0175 | 1.2 |
| 21 | 1197.0 | 828.88 | 0.3671 | 0.0175 | 0.9 |

Figure 80 shows the comparison between the FEA result and response surface at the 21st design point up to a depth of 2 mm.

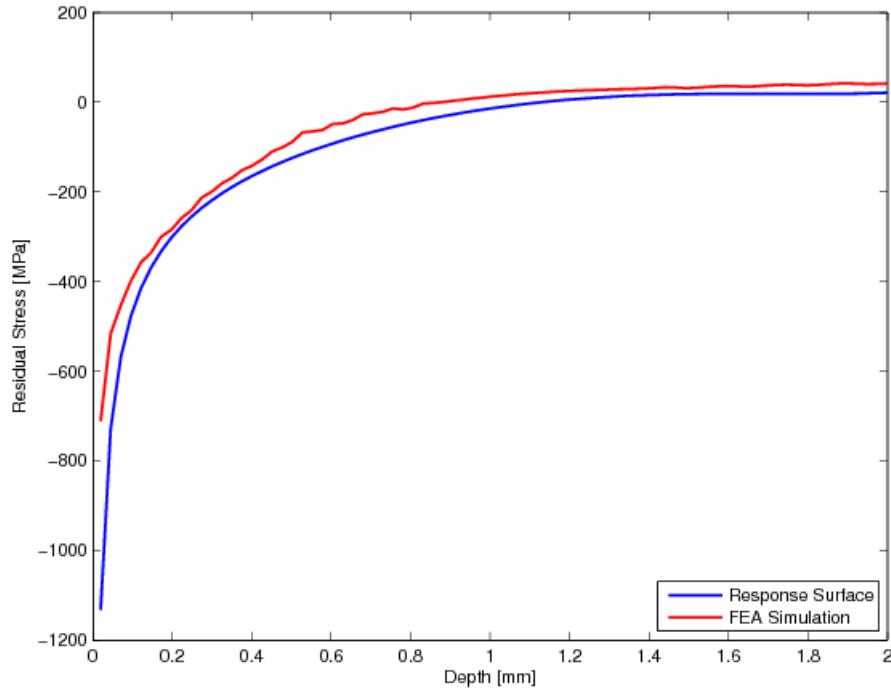


Figure 80: Response Surface Fit Comparison with FEA

It is evident from Figure 80 that the response surface is in good agreement with the FEA result along the entire depth except at the surface. The response surface over predicts at the surface, but for the purpose of validation of the framework the above obtained response surface is sufficient. The coefficients obtained from the response surface fit are shown in Table 26.

Table 26: Response Surface Coefficients

| Parameter | Value |
|------------|----------|
| α_1 | -54.70 |
| α_2 | -0.02 |
| α_3 | 3.45 |
| α_4 | 0.2304 |
| α_5 | 0.6984 |
| α_6 | -345.64 |
| α_7 | -0.5499 |
| α_8 | 155.3663 |
| α_9 | 5.6861 |

A depth of 2 mm is considered and 80 equal divisions are assumed representing the discretization (FEA mesh) of the depth. Figure 81 shows the deterministic residual stress field.

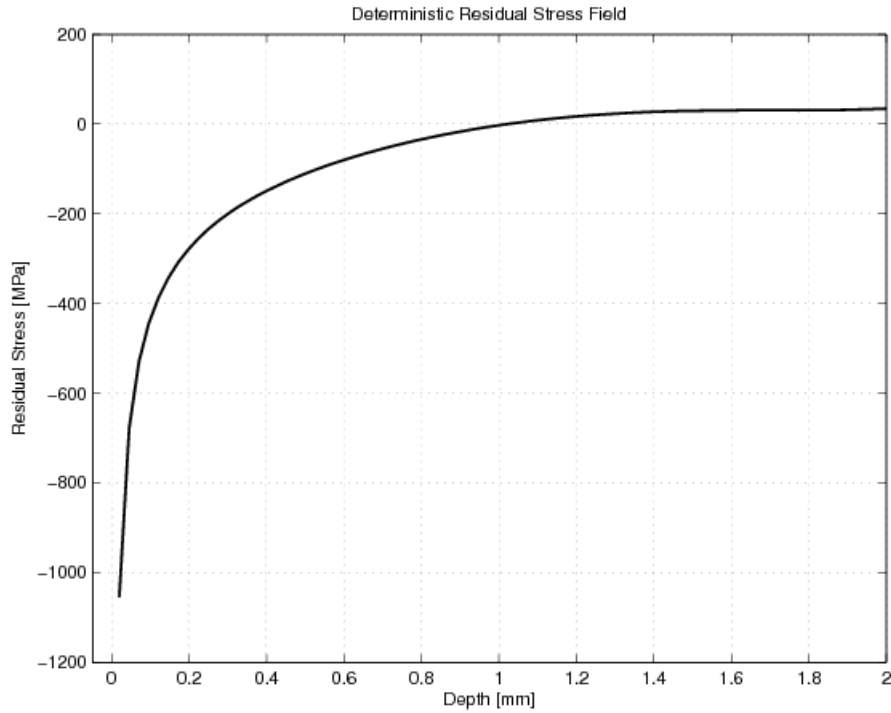


Figure 81: Deterministic Residual Stress Field for Demonstration Example 2

As we can see from the figure, the same trend observed in demonstration example 1 is also seen here. The residual stress field consists of compressive stresses at the surface and progressively leads to tensile stresses at subsurface which is similar to the LP residual stress field. A higher compressive residual stress of 1000 MPa is obtained at the surface compared to the previous example which had a compressive residual stress of 250 MPa at the surface. A central difference scheme is used again to obtain the numerical gradients of the residual stress field with respect to each model constant estimate. A comparison is made with the analytical gradients because the explicit relationship between the residual stress field and the model constants is known. Figures 82, 83, 84, and 85 show the comparison between analytical and numerical gradient of residual stress field for model constant estimates \hat{A} , \hat{B} , \hat{n} , and \hat{C} respectively.

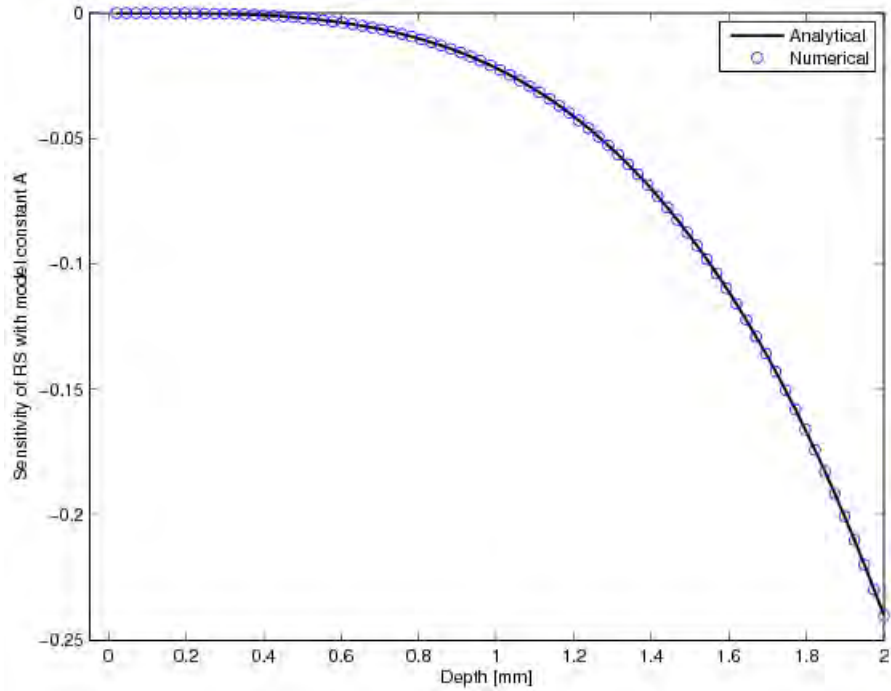


Figure 82: Gradient of Residual Stress Field with respect to Model Constant Estimate \hat{A} for Demonstration Problem 2

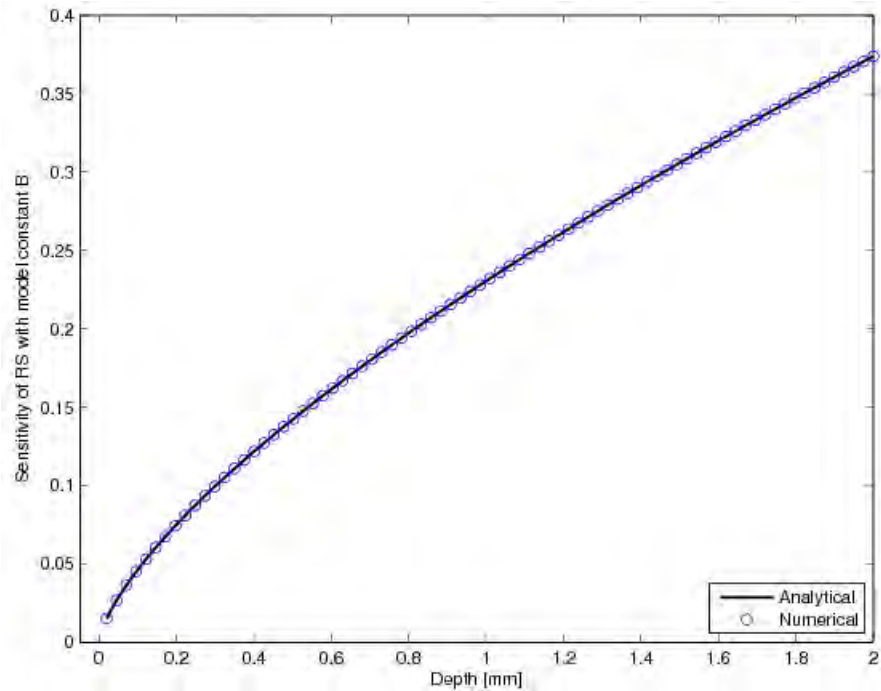


Figure 83: Gradient of Residual Stress Field with respect to Model Constant Estimate \hat{B} for Demonstration Problem 2

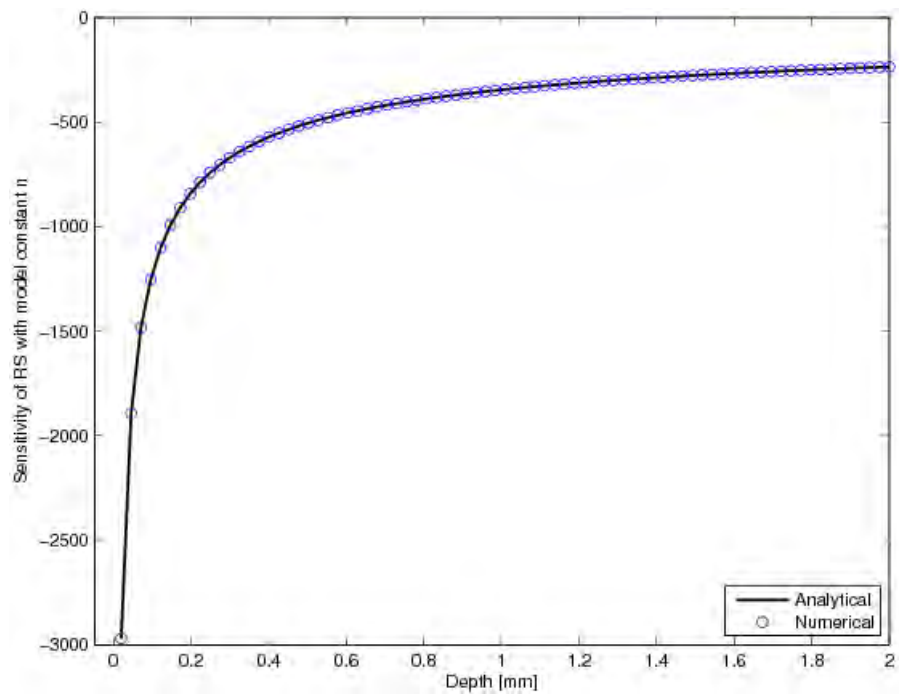


Figure 84: Gradient of Residual Stress Field with respect to Model Constant Estimate \hat{n} for Demonstration Problem 2

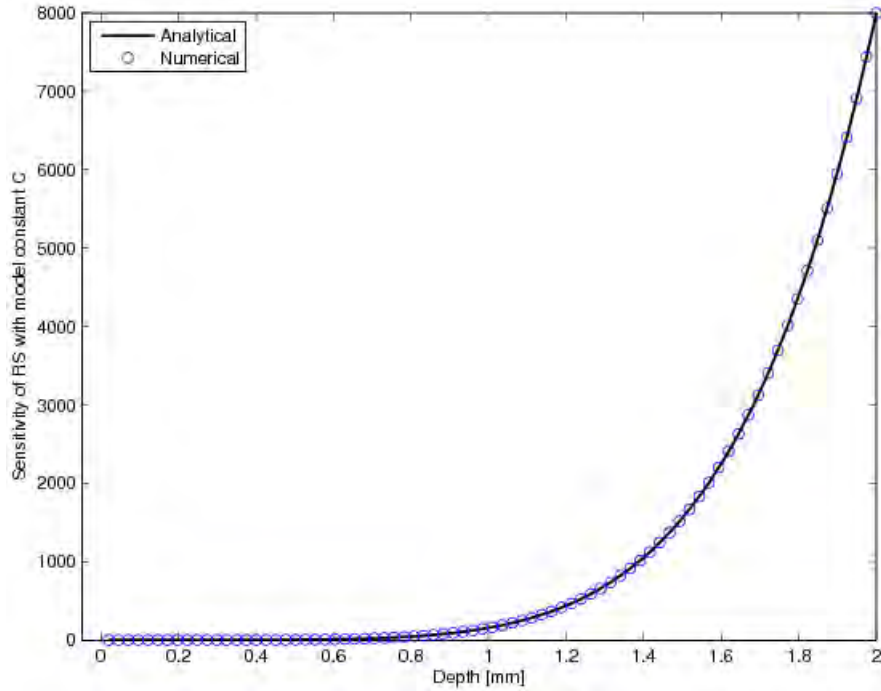


Figure 85: Gradient of Residual Stress Field with respect to Model Constant Estimate \hat{C} for Demonstration Problem 2

A good agreement between the numerical and analytical gradient is evident from these figures. Increasing trend can be seen for the model constant estimates \hat{B} , \hat{C} , and \hat{n} , while decreasing trend is evident for \hat{A} . The covariance matrix of the residual stress is obtained from the sensitivity matrix of the residual stress field with respect to each model constant estimate. Figure 86 shows the 95% confidence band on the residual stress field along with the deterministic residual stress field.

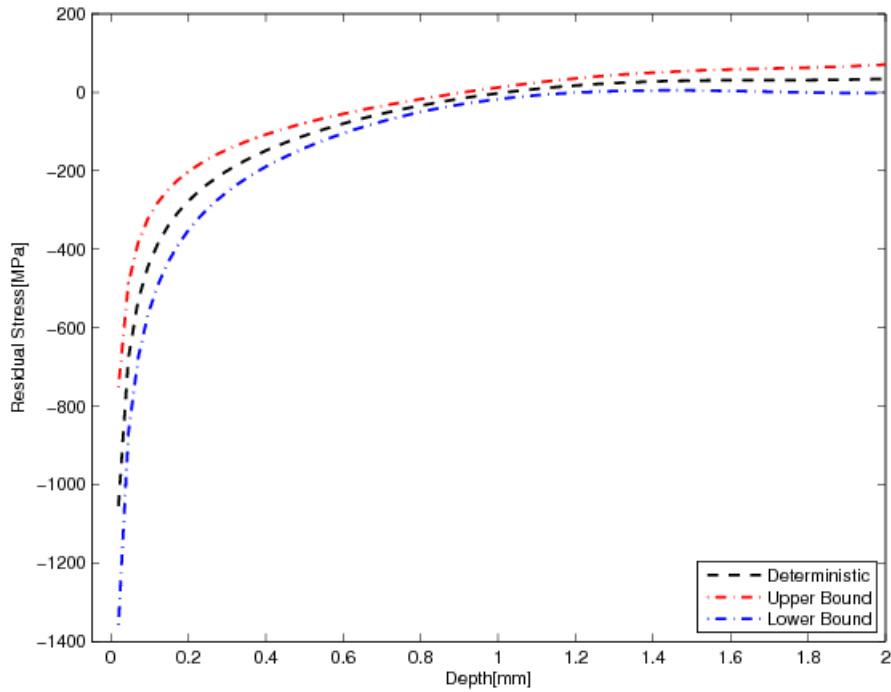


Figure 86: 95% Confidence Band on the Residual Stress Field for Demonstration Problem 2

The confidence band indicates that the true residual stress field is in between the band 95% of the times. A plot of the variability of the residual stress field along the depth can be seen in Figure 87 that shows standard deviation against depth.

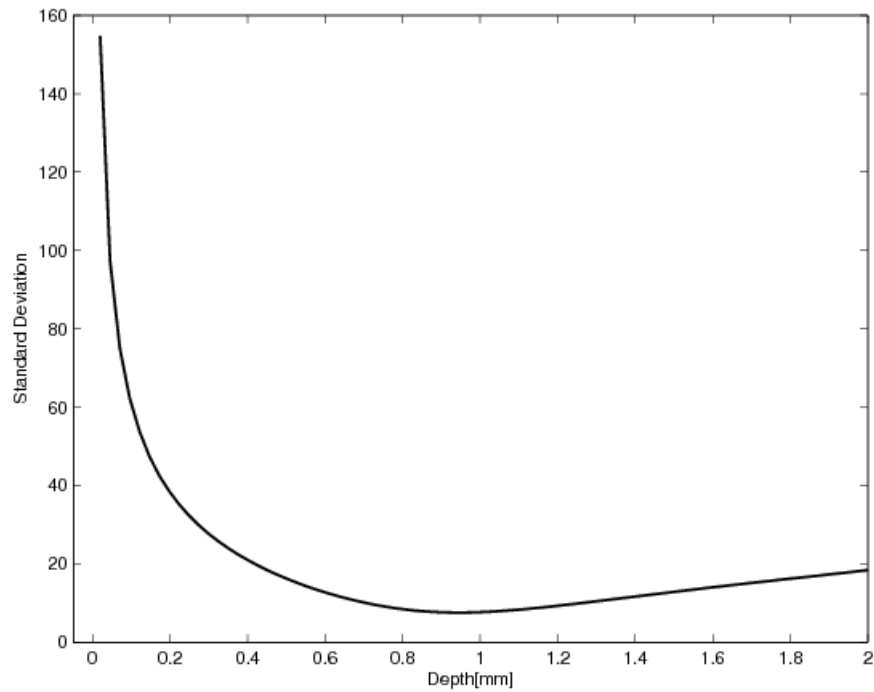


Figure 87: Standard Deviation Variation along the Depth for Demonstration Problem 2

A higher variability of residual stress can be seen at the surface and progressively decreases along the depth. A maximum variability of $\approx 160\text{MPa}$ is obtained at the surface while least variability of $\approx 15\text{MPa}$ can be seen at a depth of $\approx 1\text{mm}$.

A Monte Carlo analysis is performed to validate the developed residual stress band. Figure 88 shows the comparison between the target and achieved confidence level for the million Monte Carlo samples along the entire depth. It can be seen from Figure 88 that the achieved confidence level is lower than the target confidence level at the surface regions while a higher confidence level is achieved sub surface.

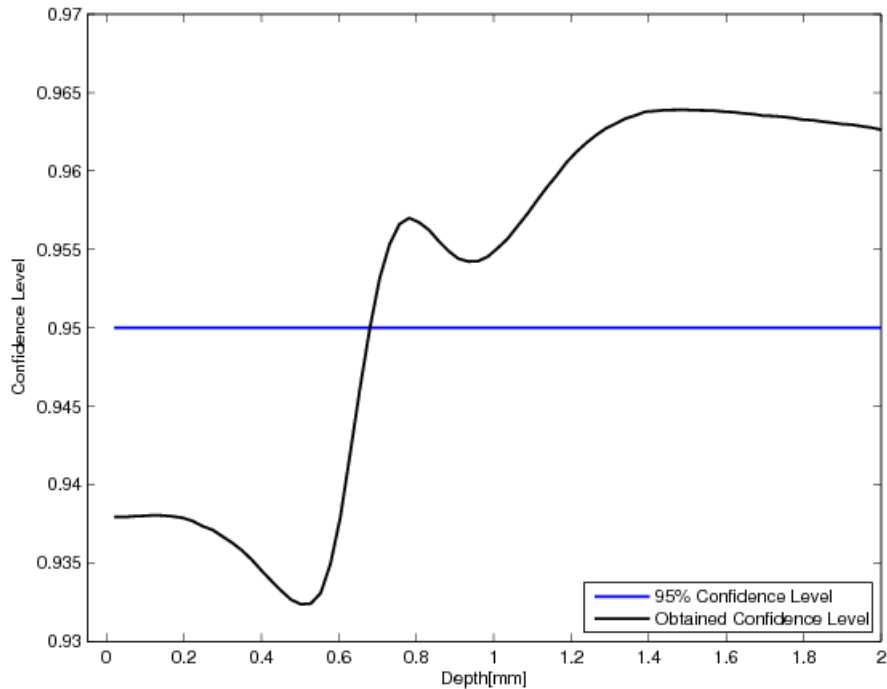


Figure 88: Confidence Level Comparison to Target Confidence Level for Demonstration Problem 2

A lowest confidence level of $\approx 93\%$ is achieved at a depth of $\approx 0.6\text{mm}$ and a highest confidence of $\approx 96.5\%$ at a depth of $\approx 1.4\text{mm}$. The obtained confidence level differs from the target value of 95% could be due to Taylor series approximation and/or lack of normality in regression estimates.

6.5.3 LP Application

For the LP application, no explicit relationship between residual stress and material model constants is available. FEA is used to simulate the residual stress fields generated by the LP process. The estimates obtained in Table 24 are used to obtain the deterministic residual stress field. Figure 89 shows the deterministic residual stress field with a peak pressure of 5.5 GPa.

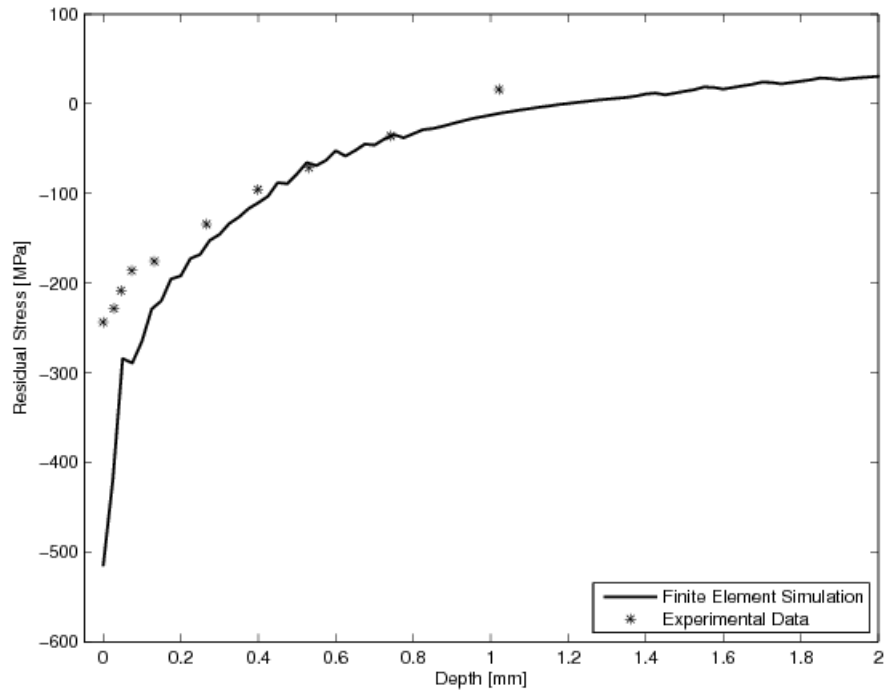


Figure 89: Deterministic Residual Stress Field for the LP Process Simulation

A comparison is also shown with the experimental data [38]. It is evident from the Figure 89 that compressive residual stresses are generated at the surface and compensated by tensile stresses in the sub-surface. Figures 90, 91, 92, and 93 show the gradients of residual stress field with respect to model constant estimates \hat{A} , \hat{B} , \hat{n} , and \hat{C} and respectively.

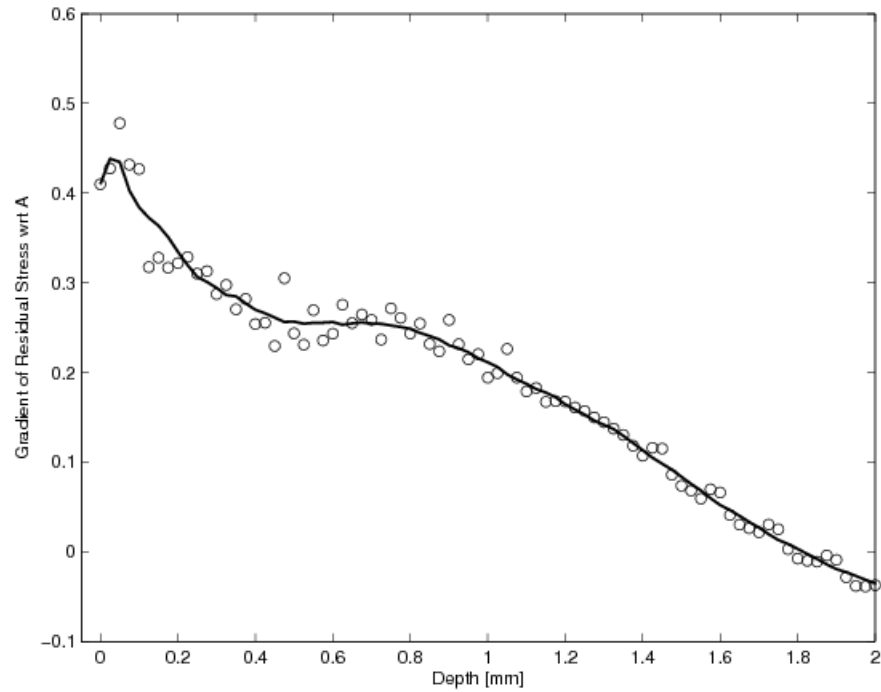


Figure 90: Gradient of Residual Stress Field with respect to Model Constant Estimate \hat{A} for the LP Simulation

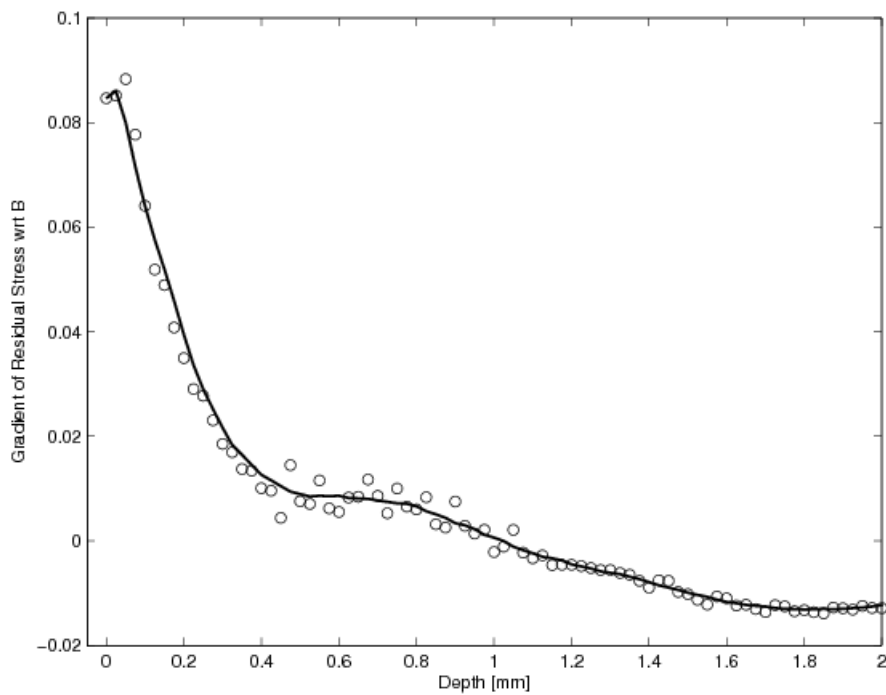


Figure 91: Gradient of Residual Stress Field with respect to Model Constant Estimate \hat{B} for the LP Simulation

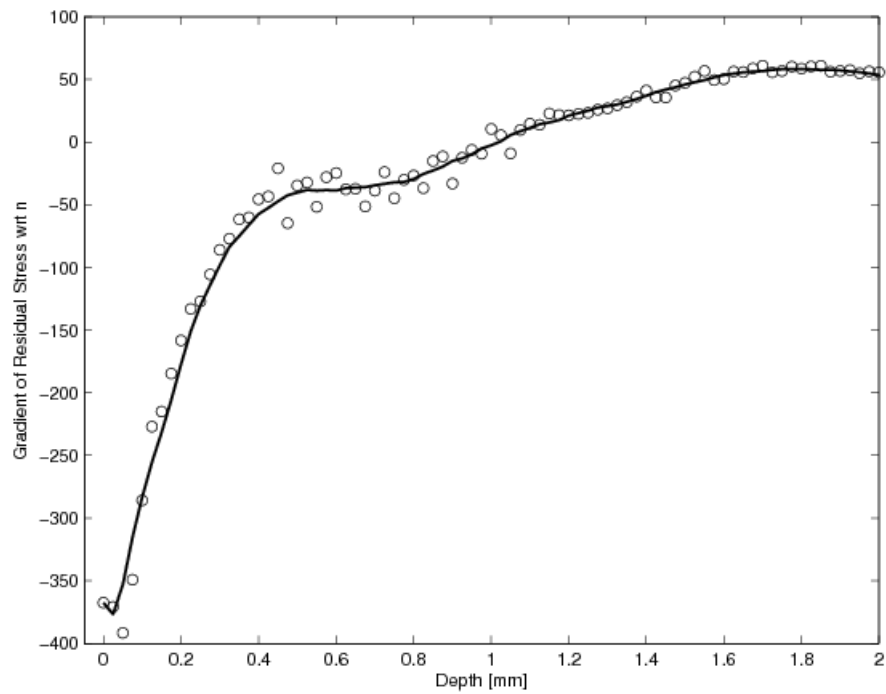


Figure 92: Gradient of Residual Stress Field with respect to Model Constant Estimate \hat{n} for the LP Simulation

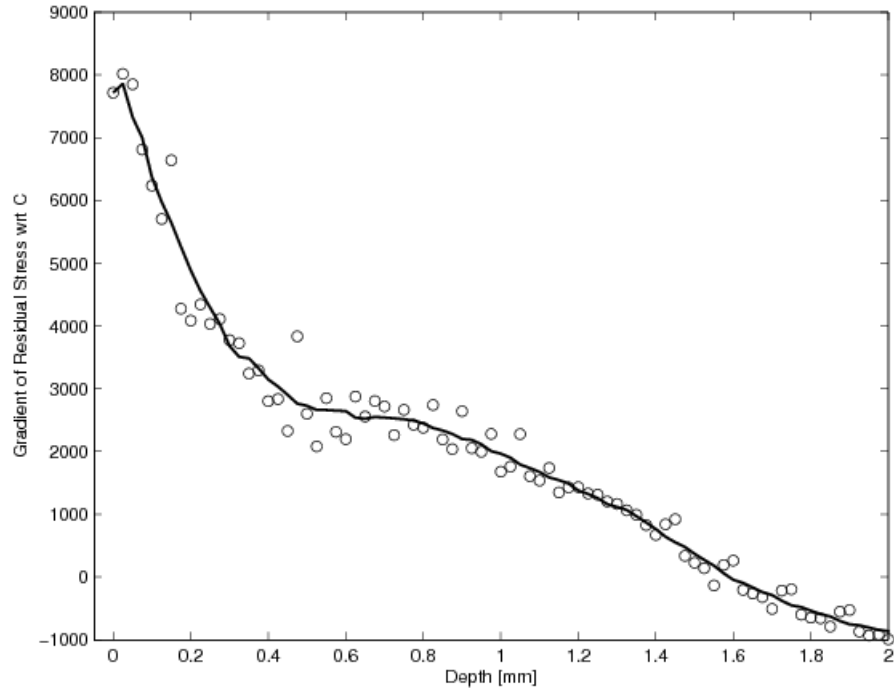


Figure 93: Gradient of Residual Stress Field with respect to Model Constant Estimate \hat{C} for the LP Simulation

Central difference scheme is used to obtain the gradients. Assuming the true gradients are smooth function, the numerical gradients generated by central difference scheme are smoothed. It can be seen from these figures that the gradients are on different scales. Decreasing trend can be seen for the model constant estimates \hat{A} , \hat{B} , and \hat{C} , while an increasing trend is evident for estimate \hat{n} . 95% confidence band for the residual stress field at each depth is shown in Figure 94.

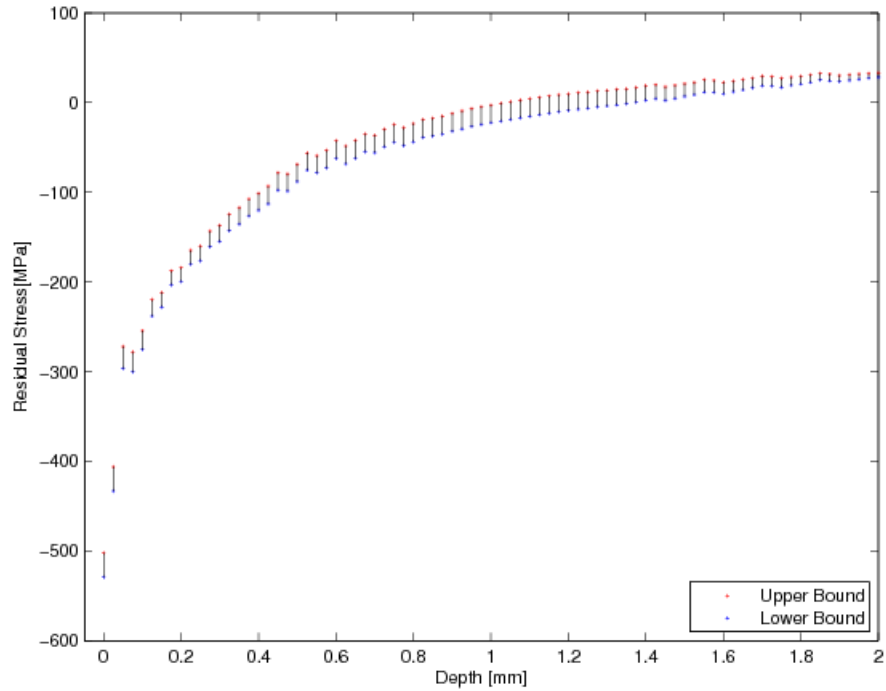


Figure 94: 95% Confidence Band on the Residual Stress Field for the LP Simulation

A higher variance of residual stress is obtained at the surface and decreases along the depth. A plot of the variability along the depth can be seen in Figure 95 that shows the standard deviation against depth.

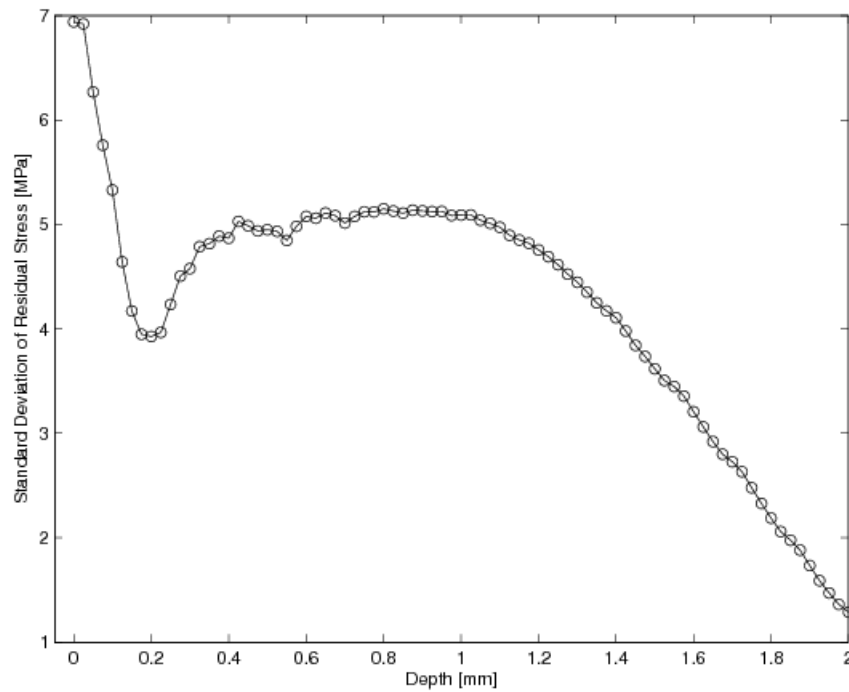


Figure 95: Standard Deviation of Residual Stress Field for the LP Simulation

A maximum deviation of 7MPa is obtained at the surface. This indicates that the JC model is robust in prediction of residual stress field for the LP process. The variation of residual stress depends on the material model, experimental data, and relationship between residual stress field and model constants.

6.6 Section Summary

In this chapter, a framework is developed to quantify the uncertainty in residual stress field induced by the LP simulation. Input uncertainty is quantified from a non-linear regression analysis that is used to fit the constitutive material model to the experimental data of stress-strain at different strain rates. A bootstrapping technique is used to evaluate the multivariate normality assumption of the material model constant estimates. Taylor series expansion in combination with sensitivity analysis is used to propagate the input uncertainty. Two demonstration examples are shown to validate the methodology by comparing the obtained confidence level with target confidence level using Monte Carlo analysis. The JC material model is shown to be a robust model to simulate the LP process with a maximum residual stress standard deviation of 7 MPa is obtained at the surface.

7.0 SUMMARY AND FUTURE DIRECTIONS

This chapter provides a brief summary of the research work performed and possible future directions for the research that can be extended. In this work, the simulation of the LP process is performed and the residual stress field generated by the LP simulation is quantified by the propagation of regression uncertainty.

Material model validation for the simulation of the LP process is presented. FEA is shown to be a useful method to simulate the LP process. Three different material models, the EPP, the JC model, and the ZA model, are used for the validation purposes. Efficient modeling of the LP process is performed by incorporating infinite elements to represent the non-reflecting boundary conditions. An integration framework is implemented for efficient data management between ABAQUS/Explicit and ABAQUS/Standard. The EPP model, which is most often used in the literature, is shown to produce inconsistent results. The simulation results are compared with the experimental data for three different peak pressures including multiple shots. The ZA model, which is based on dislocation mechanics, produces consistent trends but overestimates the results compared to experimental data. The JC model is shown to produce consistent results matching the trends and better agreement with experimental results.

Inverse optimization-based approach is designed to obtain the material behavior when very little or no experimental data of stress-strain curves is available. The optimization-based approach is shown to predict residual stresses that are consistent with experimental results. The consistency of the approach is shown by validating for two materials including Inconel®718 and Ti-6Al-4V. LP experiments were performed in collaboration with LSP Technologies Inc, Dublin, OH with a Nd-glass laser for Inconel®718 at four different energy densities and the residual stress measurements were made using an x-ray diffraction method. For the Inconel®718, the JC and the KHL models predicted the trends and the simulation results are in agreement with the experimental results for the lower two peak pressures. The JC and the KHL models are shown to perform better than the ZA model in prediction of residual stresses compared to experimental data for Ti-6Al-4V.

A framework is developed to quantify the uncertainty in residual stress field induced by the LP simulation. The input uncertainty is quantified from a non-linear regression analysis that is used to fit the constitutive material model to the experimental data of stress-strain at different strain rates. A technique from statistics known as 'bootstrap for regression' is used to evaluate the multivariate normality assumption of the material model constant estimates. Taylor series expansion in combination with sensitivity analysis is used to propagate the input uncertainty. Two demonstration examples are shown to validate the methodology by comparing the obtained confidence level with target confidence level using Monte Carlo analysis. The first example is a logarithmic relationship between the residual stress field and the model constant estimates while the second example is a response surface fit of the FEA. The LP application results show that the JC material model is a robust model to simulate the residual stresses induced by the LP process.

7.1 Future Directions

The presented research work of finite element simulations of the residual stresses induced by the LP process can be extended to modeling of thin specimens, two side LP simulation, geometric effects of LP, and integrated framework for LP design.

7.1.1 Modeling of Thin Specimens

In the current work, LP simulations are performed on thick specimens. Future work can be extending the research work to thin specimens. In this aspect, accurate tracking of shock waves reflecting from the surface and appropriate material behavior changes can be investigated.

7.1.2 Two Sided LP Simulation

Very little work has been performed in the literature on two sided LP simulation. Simulating the two sided LP process can be a challenge not only in understanding the physics of the material but also in computational cost. Efficient techniques need to be developed to address the computing cost.

7.1.3 Geometric Effects of the LP Process

In the current work and most of the literature focuses the work on simulating flat surfaces. Geometric effects of component that need to be laser peened can be investigated. Efforts must be made to model the real scale component instead of coupon level scale, that will allow curvature effects to be investigated.

7.1.4 Bootstrapping Method for Parametric Uncertainty

In this work, the bootstrapping method was used to validate normality assumption of the model constant estimates for the non-linear regression analysis. For the future work, the bootstrapping method can be adapted to define the distribution of a parametric uncertainty including peak pressure, spot radius, material properties, and geometric dimensions . Figure 96 shows the schematic representation of application of bootstrapping technique for regression uncertainty.

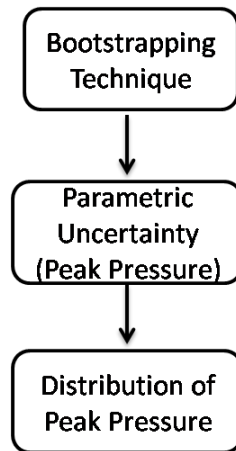


Figure 96: Bootstrapping for Parametric Uncertainty

The peak pressure of the shock wave can be considered as an example for demonstration. The bootstrapping method can be used to obtain a histogram of the peak pressure with limited experimental data. The mean of the experimental data is considered as the sample statistic to obtain the histogram. The obtained histogram is matched with the known distributions to obtain not only the nature of the distribution but also the parameters of the distribution. Other sample statistics such as variance could also be used to obtain further analysis of the parameters of the distribution.

Other types of uncertainties including model uncertainty and shape uncertainty can be integrated with the bootstrapping method based on the availability of the experimental data. For the model uncertainty, bootstrapping method can be used to obtain the confidence interval of the LP residual stresses and then integrated with the model uncertainty quantification method. Bootstrapping method can be used with multiple statistics including mean and standard deviation to define the shape uncertainty.

7.1.5 Integration Framework for LP Design

An integrated framework can be investigated for the implementation of LP design as shown in the Figure 97. Different tools can be integrated to obtain maximum benefit from the LP process. Given a structural component, this framework would consider both its geometric configuration and constituent material(s) to determine an optimal LP configuration. The existing database of experimental work based on geometry, LP parameters, and materials would be used to obtain LP process parameters. High fidelity simulations combined with semi-empirical relations have to be developed and validated for new structures to update this database. The fatigue life estimation methodology including stress relaxation mechanisms have to be implemented simultaneously to obtain a realistic life estimate of the structural component. Vibration characteristics can also be investigated to avoid resonant frequencies. Risk-based analysis and optimization of the LP process would be performed based on experimental and simulated data to obtain risk quantified optimum design. This procedure would then be iterated for a specific design until a user input criterion was met. Examples include a percentage increase in fatigue life or failure at a given

location. Eight disciplines are represented in the figure, while other disciplines can be added to the framework.

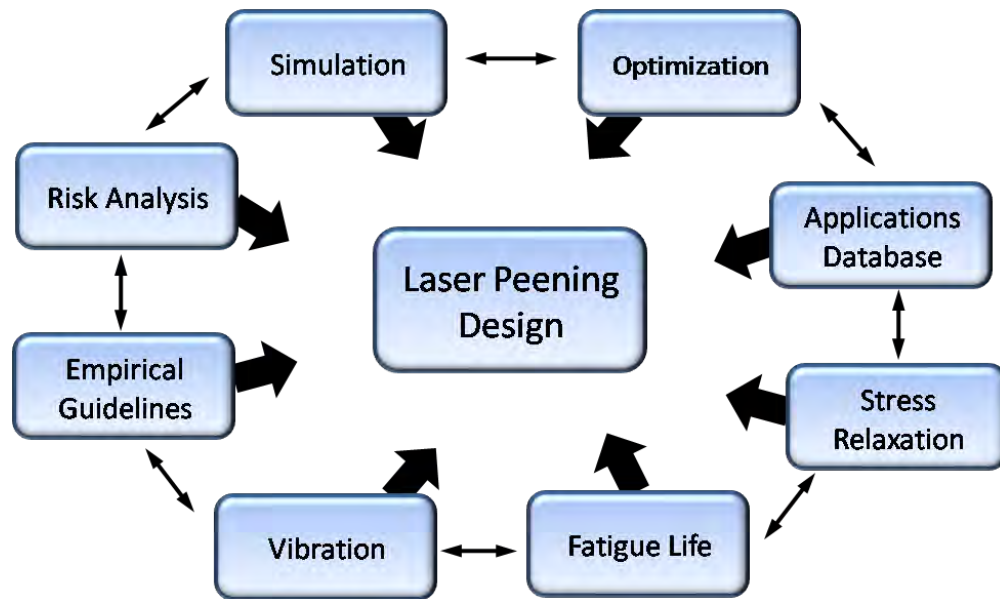


Figure 97: Integration Framework for LP Design

8.0 REFERENCES

- [1] "F-22 Raptor Fact Sheet," USAF, retrieved on may 25, 2010, november 11, 2009.
- [2] "In wikipedia, the free encyclopedia," retrieved may 25, 2010.
- [3] Cayton., M., Bunch., J., Walker., P., Brown., J., Brussat., T., Ransom., J., Poast., T., Garcia., W., and Bair., R., "Test demonstrated damage tolerance of F-22 wing attach lugs with force-mate bushings," USAF Aircraft Structural Integrity Program, Palm Springs, CA, December 2007.
- [4] Weiss., R., Bunch., J., Blair, R., and Garcia, W., "Application of surface residual stresses for durability and damage tolerance Improvements in wing attachment lugs," *The 2nd International Conference on Laser Peening*, San Fransisco, CA, April 2010.
- [5] Eckersley., J. S. and Champaigne, J., editors, *Shot peening - theory and application*, IITT-International, Gournay-Sur-Marne, France, 1991.
- [6] Chang., H., *A non-destructive method to measure the residual stresses induced by shot peening for non-magnetic materials*, Ph.D. dissertation, Cleveland State University, Cleveland, OH, 1996.
- [7] Metal Improvement Company, Inc., Manual, New Jersey, *Shot peening applications*, seventh ed.
- [8] Carek., G. A., "Shot peening of Ti-6Al-4V alloy compressor blades," Technical paper 2711, NASA, 1987.
- [9] Meguid., S. A., Shagal., G., Stanart., J. C., and Daly., J., "Three-dimensional dynamic finite element analysis of shot-peening induced residual stresses," *Finite elements in analysis and design*, Vol. 31, No. 3, 1999, pp. 179–191.
- [10] Shepard., M. J., Smith., P. R., and Amer., M. S., "Introduction of compressive residual stresses in Ti-6Al-4V simulated airfoils via laser shock processing," *Journal of Materials Engineering and Performance*, Vol. 10, No. 6, 2001, pp. 670–678.
- [11] Prevey., P. S., "Burnishing method and apparatus for providing a layer of compressive residual stress in the surface of a workpiece," U. S. Patent - 5,826,453, 1998.

- [12] Prevey., P. S., "The effect of cold work on the thermal stability of residual compression in surface enhanced IN718," *20th ASM Materials solutions conference and exposition*, St. Louis, MO, 2000, pp. 426–434.
- [13] Hornbach., D. J., Prevey., P. S., and Loftus., E. F., "Application of low plasticity burnishing to improve the fatigue performance of Ti-6Al-4V femoral hip stems," *Journal of ASTM international*, Vol. 5, No. 5, 2006, pp. Paper ID: JAI13580.
- [14] Daniewicz., S. R. and Cummings, S. D., "Characterization of a water peening process," *ASME Journal of Engineering Materials and Technology*, Vol. 121, No. 3, 1999, pp. 336–340.
- [15] Tonshoff., H. K., Mohfield., A., Gey., C., and Winkler, J., "Mechanical pretreatment for improved adhesion of diamond coatings," *Surface and Coatings Technology*, Vol. 116-119, September 1999, pp. 440–446.
- [16] Kunaporn., S., Ramulu., M., and Hashish., M., "Mathematical modeling of ultra-high-pressure waterjet peening," *Journal of Engineering Materials and Technology*, Vol. 127, No. 2, 2005, pp. 186–191.
- [17] Rajesh., N., Veeraraghavan., S., and Babu., N. R., "A novel approach for modelling of water jet peening," *International Journal of Machine Tools and Manufacture*, Vol. 44, No. 7-8, 2004, pp. 855–863.
- [18] Peyre., P. and Fabbro., R., "Laser shock processing: a review of the physics and applications," *Optical and Quantum Electronics*, Vol. 27, No. 12, 1995, pp. 1213–1229.
- [19] Montross., C. S., Tao., W., Ye., L., Clark., G., and Mai, Y.-W., "Laser shock processing and its effects on microstructure and properties of metal alloys: a review," *International journal of fatigue*, Vol. 24, No. 10, 2002, pp. 1021–1036.
- [20] Clauer., A. H., "How did we get here? A historical perspective of laser peening," First International Conference on Laser Peening, Houston, TX, Dec 15 - 17 2008.
- [21] White, R. M., "Elastic wave generation by electron bombardment or electromagnetic wave absorption," *Journal of Applied Physics*, Vol. 34, No. 7, 1963, pp. 2123–2124.
- [22] Gregg., D. W. and Thomas, S. J., "Momentum transfer produced by focused laser giant pulses," *Journal of Applied Physics*, Vol. 37, No. 7, 1966, pp. 2787–2789.
- [23] Skeen., C. H. and York, C. M., "Laser-induced "Blow-Off" phenomena," *Applied Physics Letters*, Vol. 12, No. 11, 1968, pp. 369–371.
- [24] Anderholm, N. C., "Laser-generated stress waves," *Applied Physics Letters*, Vol. 16, No. 3, 1970, pp. 113–115.
- [25] Malozzi., P. and Fairand., B. P., "Altering material properties," U. S. Patent 3,850,698, November 26 1974.
- [26] Clauer., A. H. and Fairand., B. P., "Interaction of laser-induced stress waves with metals," *Applications of Lasers in Materials Processing*, AMS, Materials Park, OH, 1979.

- [27] Shepard., M. J., *Laser shock processing induced residual compression for improved damage tolerance design*, Ph.D. dissertation, University of Dayton, Dayton, OH, December 2004.
- [28] Fairand., B. P. and Clauer, A. H., "Applications of laser-induced stress waves," Presented at Lasers in Modern Industry Seminar, Cambridge, MA, Society of Manufacturing Engineers, May 23-25 1978.
- [29] Fairand., B. P. and Clauer, A. H., "Laser generation of high-amplitude stress waves in materials," *Journal of Applied Physics*, Vol. 50, No. 3, 1979, pp. 1497–1502.
- [30] Peyre., P., Fabbro., R., Merrien., P., and Lieurade, H. P., "Laser shock processing of aluminum alloys. Application to high cycle fatigue behavior," *Materials Science and Engineering A*, Vol. 210, No. 1-2, June 1996, pp. 102–113.
- [31] Montross., C. S., Florea., V., and Swain, M. V., "The influence of coatings on subsurface mechanical properties of laser peened 2011-T3 aluminum," *Journal of Materials Science*, Vol. 36, No. 7, 2001, pp. 1801–1807.
- [32] Anderholm, N. C., "Laser generated pressure waves," *American Physical Society Bulletin*, Vol. 11, No. 13-BK9, 1968, pp. 388.
- [33] Fairand., B. P., Wilcox., B. A., Gallagher., W. J., and Williams., D. N., "Laser shock-induced microstructural and mechanical property changes in 7075 aluminum," *Journal of applied physics*, Vol. 43, No. 9, 1972, pp. 3893–3895.
- [34] Fabbro., R., Fournier., J., Ballard., P., Devaux., D., and Virmont, J., "Physical study of laser-produced plasma in confined geometry," *Journal of Applied Physics*, Vol. 68, No. 2, 1990, pp. 775–784.
- [35] Fairand., B. P., Clauer., A. H., Jung., R. G., and Wilcox, B. A., "Quantitative assessment of laser-induced stress waves generated at confined surfaces," *Applied Physics Letters*, Vol. 25, No. 8, 1974, pp. 431–433.
- [36] Peyre., P., Berthe., L., Fabbro., R., and Sollier, A., "Experimental determination by PVDF and EMV techniques of shock amplitudes induced by 0.6-3 ns laser pulses in a confined regime with water," *Journal of Physics D: Applied Physics*, Vol. 33, No. 5, 2000, pp. 498–503.
- [37] Braisted., W. and Brockman., R., "Finite element simulation of laser shock peening," *International Journal of Fatigue*, Vol. 21, No. 7, 1999, pp. 719–724.
- [38] Nam., T., *Finite element analysis of residual stress field induced by laser shock peening*, Ph.D. dissertation, The Ohio State University, 2002.
- [39] Yilbas., B. S., Shuja., S. Z., Arif., A., and Gondal, M. A., "Laser-shock processing of steel," *Journal of Materials Processing Technology*, Vol. 135, No. 1, 2003, pp. 6–17.
- [40] Arif., A. F., "Numerical prediction of plastic deformation and residual stresses induced by laser shock processing," *Journal of Materials Processing Technology*, Vol. 136, No. 1-3, 2003, pp. 120–138.

- [41] Ding., K. and Ye., L., “Three-dimensional dynamic finite element Analysis of multiple laser shock peening processes,” *Surface Engineering*, Vol. 19, No. 5, 2003, pp. 351–358.
- [42] Ding., K. and Ye, L., “FEM simulation of two sided laser shock peening of thin sections of Ti - 6Al - 4V alloy,” *Surface engineering*, Vol. 19, No. 2, 2003, pp. 127–133.
- [43] Ocana., J. L., Morales., M., Molpeceres., C., and Torres., J., “Numerical simulation of surface deformation and residual stresses fields in laser shock processing experiments,” *Applied Surface Science*, Vol. 238, No. 15, 2004, pp. 242–248.
- [44] Wu., B. and Shin, Y. C., “A self-closed thermal model for laser shock peening under the water confinement regime configuration and comparisons to experiments,” *Journal of Applied Physics*, Vol. 97, No. 11, 2005, pp. 113517–1 –11.
- [45] Wu., B. and Shin, Y. C., “From incident laser pulse to residual stress: A complete and self-closed model for laser shock peening,” *ASME Journal of Manufacturing Science and Engineering*, Vol. 129, No. 1, 2007, pp. 117–125.
- [46] Peyre., P., Chaieb., I., and Braham., C., “FEM calculation of residual stresses induced by laser shock processing in stainless steels,” *Modelling and Simulation in Materials Science and Engineering*, Vol. 15, No. 3, 2007, pp. 205–221.
- [47] Warren., A. W., Guo., Y. B., and Chen., S. C., “Massive parallel laser shock peening: Simulation, analysis, and validation,” *International Journal of Fatigue*, Vol. 30, No. 1, 2008, pp. 188–197.
- [48] Srinivasan, M., *Finite element simulation of laser shock peening process*, Master’s thesis, University of Cincinnati, Cincinnati, OH, March 2008.
- [49] Yang., C., Hodgson., P. D., Liu., Q., and Ye, L., “Geometrical effects on residual stresses in 7050-T7451 aluminum alloy rods subject to laser shock peening,” *Journal of Materials Processing Technology*, Vol. 201, No. 1-3, 2008, pp. 303–309.
- [50] Hadipriono, F. C., *"Fuzzy sets in probabilistic structural mechanics" in Probabilistic Structural Mechanics Handbook*, Chapman & Hall, New York, 1995.
- [51] Zadeh, L., “Fuzzy sets,” *Information and Control*, Vol. 8, No. 3, 1965, pp. 338–353.
- [52] Bae., H. R., Grandhi., R. V., and Canfield, R. A., “Uncertainty quantification of structural response using evidence theory,” *AIAA Journal*, Vol. 41, No. 10, 2003, pp. 2062–2068.
- [53] Yakov, B.-H., *Info-gap decision theory: Decisions under severe uncertainty*, Academic Press, London, UK, 2nd ed., 2006.
- [54] Helton., J. C. and Davis, F. J., “Latin hypercube sampling and the propagation of uncertainty in analyses of complex systems,” *Reliability Engineering and System Safety*, Vol. 81, No. 1, 2003, pp. 23–69.

- [55] Sallabery., C. J., Helton., C. J., and Hora, S. C., “Extension of latin hypercube samples with correlated variables,” *Reliability Engineering and System Safety*, Vol. 93, No. 7, 2008, pp. 1047–1059.
- [56] Choi., S.-K., Grandhi., R. V., and Canfield, R. A., *Reliability-based structural design*, Springer-Verlag, London, UK, 2007.
- [57] Youn., B. D., Choi., K. K., and Du, L., “Adaptive probability analysis using an enhanced hybrid mean value method,” *Structural and Multidisciplinary Optimization*, Vol. 29, No. 2, 2005, pp. 134–148.
- [58] Rahman., S. and Xu, H., “A univariate dimension-reduction method for multi-dimensional integration in stochastic mechanics,” *Probabilistic engineering mechanics*, Vol. 19, No. 4, 2004, pp. 393–408.
- [59] Youn., B. D., Zhimin., X., and Pingfeng, W., “Eigenvector dimension reduction (EDR) method for sensitivity-free probability analysis,” *Structural and Multidisciplinary Optimization*, Vol. 37, No. 1, 2008, pp. 13–28.
- [60] Penmetsa., R. C. and Grandhi, R. V., “Adaptation of fast fourier transformations to estimate structural failure probability,” *Finite Elements in Analysis and Design*, Vol. 39, No. 5-6, 2003, pp. 473–485.
- [61] Choi., S.-K., Canfield., R. A., and Grandhi, R. V., “Estimation of structural reliability for gaussian random fields,” *Structure and Infrastructure Engineering*, Vol. 2, No. 3-4, 2006, pp. 161–173.
- [62] Millwater., H., Larsen., J., and John, R., “Effects of residual stresses on probabilistic lifing of engine disk materials,” *Materials Science and Engineering: A*, Vol. 468-470, No. 15, 2007, pp. 129–136.
- [63] Millwater., H., John., R., Larsen., J., and Buchanan, D., “Probabilistic modeling of residual stress data in IN100,” No. AIAA 2008-1983, 49th AIAA/ASME/ASCE/AHS/ASC Structures, Structural Dynamics, and Materials Conference, Schaumburg, IL, April 2008.
- [64] Khaled., A.-T. and Noor, A. K., “Uncertainty analysis of welding residual stress fields,” *Computer Methods in Applied Mechanics and Engineering*, Vol. 179, No. 3-4, 1999, pp. 327–344.
- [65] Grujicic., M., Delong., J. R., and DeRosset, W., “Probabilistic finite element analysis of residual stresses in shrink-fit hybrid ceramic/steel gun barrels,” *Journal of Materials: Design & Applications*, Vol. 216, No. 4, 2002, pp. 219–231.
- [66] Sobczyk., K. and Trebicki, J., “Fatigue crack growth in random residual stresses,” *International Journal of Fatigue*, Vol. 26, No. 11, 2004, pp. 1179–1187.
- [67] Park., I., Amarchinta., H. K., and Grandhi, R. V., “A bayesian approach for quantification of model uncertainty,” *Reliability Engineering and System Safety*, Vol. 95, No. 7, 2010, pp. 777–785.

- [68] Meyers., M. A., *Dynamic behavior of materials*, John Wiley & Sons, NY, 1994.
- [69] Bodner, S. R., *Unified plasticity for engineering applications*, Kluwer/Plenum, New York, NY, 2002.
- [70] Miller, A., “An inelastic constitutive model for monotonic, cyclic, and creep deformation, part 1,” *ASME Journal of Engineering Materials and Technology*, Vol. 98, 1976, pp. 97–105.
- [71] Bammann., D. J., Chiesa., M. L., and Johnson., G. C., “Modeling large deformation and failure in manufacturing process,” *Proceedings of 19th international congress of theoretical and applied mechanics*, Kyoto, Japan, August 1996, pp. 359–376.
- [72] Johnson., G. R. and Cook., W. H., “A constitutive model and data for metals subjected to large strains, high strain rates and high temperatures,” *Proceedings of the Seventh International Symposium on Ballistics*, The Hague, Netherlands, April 1983, pp. 541–547.
- [73] Zerilli., F. J. and Armstrong., R. W., “Dislocation-mechanics-based constitutive relations for materials dynamic calculations,” *Journal of Applied Physics*, Vol. 61, No. 5, 1987, pp. 1816–1825.
- [74] Zerilli., F. J., “Dislocation mechanics-based constitutive equations,” *Metallurgical and Materials Transactions A*, Vol. 35, No. 9, 2004, pp. 2547–2555.
- [75] Maiden., C. J. and Green., S. J., “Compressive strain rate tests on six selected materials at strain rates from 0.0001 to 10000 inchperinchpersecond,” *Journal of Applied Mechanics*, Vol. 33, September 1966, pp. 496–504.
- [76] Meyer., H. W., “A modified zerilli-armstrong constitutive model describing the strength and localizing behavior of Ti-6Al-4V,” Tech. Rep. ARL-CR-0578, Army Research Laboratory, 2006.
- [77] Khan., A. S., Suh., Y. S., and Kazmi, R., “Quasi static and dynamic loading responses and constitutive modeling of titanium alloys,” *International Journal of Plasticity*, Vol. 20, No. 12, 2004, pp. 2233–2248.
- [78] Ding., K. and Ye, L., *Laser shock peening: Performance and process simulation*, Woodhead Publishing Limited, Cambridge, UK, 2006.
- [79] Mathworks, Natick, MA, *MATLAB Optimization tool box 3, user’s guide*, 2007.
- [80] Dassault Systemes, Providence, RI, *ABAQUS users manual*.
- [81] Cook., R. D., Malkus., D. S., and Plesha, M. E., *Concepts and applications of finite element analysis*, John Wiley & Sons, New York, 3rd ed., 1989.
- [82] *Special Metals Corporation*, publication number smc-045 ed., September 2007.
- [83] Amarchinta., H. K., Grandhi., R. V., Langer., K., and Stargel, D. S., “Material model validation for laser shock peening process simulation,” *Modelling and Simulation in Materials Science and Engineering*, Vol. 17, No. 1, 2009, pp. id:015010.

- [84] Montgomery., D. C. and Peck, E. A., *Introduction to linear regression analysis*, John Wiley & Sons, New York, 2nd ed., 1992.
- [85] Bates., D. M. and Watts, D. G., *Nonlinear regression analsis and its applications*, John Wiley & Sons, 1988.
- [86] Montgomery, D. C., *Design and analysis of experiments*, John Wiley & Sons, New York, sixth ed., 2005.
- [87] Ratkowsky, D. A., *Nonlinear regression modeling: A unified practical approach*, Marcel Dekker Inc., New York, 1983.
- [88] Chernick, M. R., *Bootstrap methods: A guide for practitioners and researchers*, John Wiley & Sons, New York, 2nd ed., 2008.
- [89] Efron., B. and Tibshirani, R. J., *An introduction to the bootstrap*, Chapman & Hall, New York, 1993.
- [90] Mathworks, Natick, MA, *MATLAB Statistics tool box 7, user's guide*, 2010.
- [91] Picheny., V., Kim., N. H., and Haftka, R. T., "Application of bootstrap method in conservative estimation of reliability with limited samples," *Journal of Structural and Multidisciplinary Optimization*, Vol. 41, No. 2, 2010, pp. 205–217.
- [92] Fox, J., *Bootstrapping regression models, An R and S-plus companion to applied regression: A web appendix to the book*, Sage Publications, Thousand Oaks, CA, 2002.

LIST OF ACRONYMS, ABBREVIATIONS AND SYMBOLS

| | |
|-----------------------|---|
| ε | Strain |
| $\dot{\varepsilon}$ | Strain Rate |
| $\dot{\varepsilon}_0$ | Initial Strain Rate |
| σ | Flow Stress |
| σ_y | Yield Strength |
| ν | Poissons Ratio |
| A | Material Constant for the Johnson-Cook Material Model |
| AFRL | Air Force Research Laboratory |
| B | Material Constant for the Johnson-Cook Material Model |
| BCC | Body Centered Cubic |
| C | Material Constant for the Johnson-Cook Material Model |
| C_i | Material Constants for Zerilli Armstrong Model, $i=1,2,3,4,5$. |
| EOS | Equation of State |
| EPP | Elastic Perfectly Plastic |
| FCC | Face Centered Cubic |
| FEA | Finite Element Analysis |
| FFT | Fast Fourier Transformation |
| FORM | First Order Reliability Method |
| FWHM | Full Width at Half Maximum |
| HCP | Hexagonal Closely Packed |
| HEL | Hugoniot Elastic Limit |
| JC | Johnson-Cook |
| KHL | Khan-Huang-Liang |
| LHS | Latin Hypercube Sampling |
| LP | Laser Peening |
| LPB | Low Plasticity Burnishing |
| m | Material Constant for the Johnson-Cook Material Model |

| | |
|----------------|--|
| MCS | Monte Carlo Simulation |
| MPP | Most Probable Point |
| n | Material Constant for the Johnson-Cook, Zerilli-Armstrong Material Model |
| Nd | Neodymium |
| ns | nano seconds |
| RS | Residual Stress |
| SORM | Second Order Reliability Method |
| SRT | Short Rise Time |
| T | Test Temperature |
| T' | Non-Dimensionalized Temperature |
| T _m | Melting Temperature |
| T _γ | Room Temperature |
| ZA | Zerilli Armstrong |